Faculté des Sciences

Origin and properties of the two-dimensional electron gas at the $LaAlO_3/SrTiO_3$ interface: a first-principles hybrid functional study.

Dissertation présentée en vue de l'obtention du grade de

Docteur en Sciences Physiques

par

FONTAINE Denis

Promoteurs:

Prof. Philippe GHOSEZ

Membres du jury:

Prof. Matthieu VERSTRAETE (président)

Prof. Jean-Marc TRISCONE

Prof. Alessio FILIPPETTI

Dr. Daniel BILC

Dr. Eric BOUSQUET

Le 11 septembre 2014

Abstract

Complex oxides exhibit a wide range of physical properties making them very attractive for future electronic and device applications. Although more and more studied, additional scientific investigations are required, especially in oxide interfaces, where new and amazing phenomena can arise. A prototypical example is the $LaAlO_3$-$SrTiO_3$ interface that appear to be conducting, magnetic or even supra-conducting while these properties are not present in the $LaAlO_3$ and $SrTiO_3$ bulk insulator compounds. The conductivity arises from the formation of a highly localized electron gas at the interface which exhibits a different behavior than the one at semiconductor interfaces. Even nowadays, its exact origin, intrinsic versus extrinsic, is still intensively debated. The existence of an electric field in $LaAlO_3$ used as a key feature of models based on an intrinsic origin is highly controversial. In these models, the closing of the band gap with increasing $LaAlO_3$ film thicknesses finally results to a Zener breakdown and to the metal/insulator transition.

In this Ph.D. thesis we aim to investigate the various consequences of the presence of an electric field in $LaAlO_3$ through first-principles calculations in pristine $LaAlO_3$-$SrTiO_3$ interfaces. First, using both experimental and theoretical structural distortions in $LaAlO_3$, we predicted a lattice expansion via an electrostrictive effect, supporting the existence of an electric field in $LaAlO_3$. Second, the metal/insulator transition was tuned with regards to the intensity of the electric field in the film, which was controlled by the composition of a solid solution between $LaAlO_3$ and $SrTiO_3$. The theoretical results match the experimental one where, nevertheless, extrinsic origin mechanisms are allowed and defects are present. These two works are in favors of an intrinsic origin of the electronic gas observed in $LaAlO_3$-$SrTiO_3$ heterostructures. In addition, a relationship between the sheet carrier density and spatial extension of the gas was established and thus setting an intrinsic threshold to the sheet carrier concentration. At lower density the electrons are strictly localized close to the interface while above this value the carriers start to spill into the $SrTiO_3$ substrate.

Acknowledgements

Ce manuscrit est l'aboutissement d'un travail long d'une demi douzaine d'années. Tout au long de ce parcours, j'ai eu l'opportunité de rencontrer de nombreuses personnes qui ont contribué à la réalisation de cette thèse directement ou indirectement.

En premier lieu, je remercie Philippe Ghosez qui m'a offert l'opportunité de réaliser une thèse de doctorat dans un domaine de recherche alors encore peu connu pour moi, mais finalement ô combien épanouissant et excitant. Plus que ses conseils et son expérience, c'est aussi sa rigueur et son engouement qu'il aura su me transmettre. Je réalise également la patience dont il a dû faire preuve mais aussi la persévérance qu'il communique à ses étudiants en étant toujours bon et encourageant.

C'est aussi en ce début de thèse qu'Eric et Daniel m'ont accueilli dans le groupe. Mes connaissances liées aux programmes de simulations, et bien plus encore, sont entièrement dues à leur aide, toujours fournie avec bonne humeur. Par la suite, la relève sera assurée par Julien et Nick. En plus de leur aide dans mon travail, ils ont rapidement égayé les heures passées au labo et celles passées autour "d'une" bière (juste une). En particulier, cette dernière année fut le fruit d'une excellente collaboration. Je remercie aussi les autres membres du groupe ainsi que nos groupes voisins, ceux de Matthieu et de Jean-Yves.

Ce travail est riche de plusieurs collaborations qui ont directement contribué aux résultats présentés et à mon développement personnel. Je remercie donc particulièrement le groupe DPMC de Jean-Marc Triscone, celui de Phil Willmott au PSI et enfin le groupe d'Alessio Filippetti, ainsi qu'eux-mêmes. En particulier, je remercie Claudia, Alexandre et Stéphano pour nos discussions.

Durant ces années, de nombreux fous rires auront lieu grâce au "groupe du quatrième", Jérémie, Alexandre, Sophie, Alice, Cédric et Davide, qui ont malheureusement quasiment tous fuit la Belgique. Toujours présent durant ces années, le groupe des "chimistes" et associés a toujours réussi à bien me faire savoir qu'ils ne comprenaient rien à ce que je

faisais mais merci à eux. Merci aussi aux assistants, Bruno, Dorian, Antoine, etc, qui étaient présents pour la partie enseignement de mon travail et un tout grand merci à Christophe pour son aide et ses conseils.

Finalement, tout simplement merci à ma famille et à celle de Nathalie pour leur soutien et particulièrement à ma môman qui m'a offert la chance d'arriver jusqu'ici. Et même si tu ne comprends pas ce que je fais, un grand merci au nâne.

Contents

List of Figures

List of Tables

Chapter 1

Introduction

Over the last 2 decades, ABO_3 complex oxide interfaces have attracted a large community of scientists. Complex oxides represent a large variety of compounds that display a huge range of properties such as high dielectric permitivities, ferroelectricity, piezoelectricity, magnetism, multiferroism and metal-insulator transitions. Moreover the creation of an interface between 2 of these compounds enlarge even more the field of applications of these systems such as possible high temperature superconductivity or enhanced magneto-electric coupling for instance.

A typical example of new phenomena emerging at oxide interfaces is found in the $LaAlO_3$-$SrTiO_3$ heterostructure. In this system, composed of 2 large bandgap insulators, a mobile electronic gas is formed at the interface with completely new properties compared to the formal compounds. Moreover, thanks to the specific behavior of oxides (i.e. due to the interactions among the electrons), the properties of the gas are far from the usual behavior in the semiconductor heterostructures. Indeed, two-dimensionally localized electrons, high mobilities, large carrier densities, superconductivity or even magnetism are only a few examples of the rich physics found at the $LaAlO_3$-$SrTiO_3$ interface. Since this system was discovered in 2004, it is the center of interest of many research groups as can be attested by the continuously increasing number of annual citations of the seminal publication of Othomo and Hwang [1], totalizing 1300 citations[1] since that time (see figure 1.1). A possible explanation of the craze for the $LaAlO_3$-$SrTiO_3$ interface, besides from the interesting properties of the system, is that the exact mechanism at the origin of the gas formation is still unknown and is a constant source of debate.

The $LaAlO_3$-$SrTiO_3$ system is now a complex and huge field which is still growing. For

[1]Number obtained via Scopus however google scholar gives more than 1600 citations.

this reason, we focus here on a relevant and more general description corresponding to the further discussions of this work. Some parts of this field are thus not tackled. Additional information is however in the following reviews [2–12].

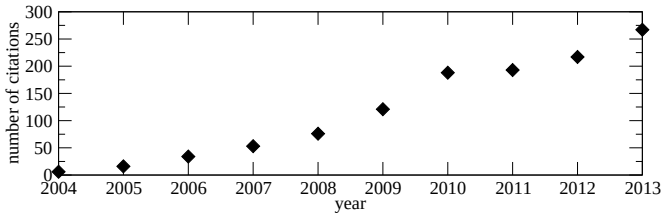

Figure 1.1: *The number of citation per year for the seminal paper of Othomo and Hwang [1]. Source from Scopus.*

In this chapter we introduce the main generic concepts underlying this work as part of materials science, complex oxides and perovskite compounds. In addition, a particular attention is devoted to the description of the interface since it is a central point of this work, as the concept of polar discontinuity. The interest of such interfaces is that it completely changes the couplings between some degrees of freedom as we will show through different examples. The specific case of the $LaAlO_3$-$SrTiO_3$ heterostructure is finally introduced with a general description of the main properties of the system. The different possible mechanisms at the origin of the electron gas formation are tackled just like the reason of the intensive debate on these ones. To close this chapter we will give the motivation and goals of the present work.

1.1 Material science

1.1.1 History

Historically, the first concerns of what is now called "materials science" was to describe the macroscopic properties of different compounds such as the electrical conductivity or the heat transport for example. The first approaches were in general phenomenological and focused on the description of properties of the materials and their evolution. An example is the work of Georg Simon Ohm (1789-1854), who has shown that there is a direct proportionality between the applied voltage V and the current I in a material, known now as Ohm's law $V = RI$, where the coefficient R is the electrical resistance of the material. It is clear that at that time, $\sim$ 1825, Ohm did not know about the existence of the electron (identified in 1897) which is the underlying particle of the electrical conductivity. It was

then impossible for him to explain qualitatively this law. However this is what material science is: the understanding of why materials behave the way they do. To achieve such a thing it was first needed to have a better understanding of the atomistic world. Nowadays, even without a scientific background, the general public know that a material is composed of nuclei which are bound together and that the electrical conductivity is due to the flow of conduction electrons. The approach is not phenomenological and qualitative anymore but is the start to quantitatively describe the electrical conductivity within a microscopic understanding. This was realized in 1900 by Paul Drude (1863-1906). He demonstrated that, considering electrons as ball-like particles that can flow into the material. However the electrons are deviated and scattered by the ions which create some resistance to the flow of electrons. This classical[2] and microscopic formalism can finally leads to Ohm's law where the resistance is now explicitly given by the parameters introduced by Drude. This is one simple example of how material science can explain the macroscopic properties of a material through a microscopic description.

The only thing that scientists are doing is to create a model that attempts to describe the physical phenomena of a system[3]. The Drude model for instance works well for simple metals at room temperature but is not always so accurate. The reason is that the Drude model simplified the problem within a classical approach. However to model a system at the atomistic level, one need to use quantum mechanics. The reason is simply that classical mechanics cannot describe properly behavior at the nano-scale where new effects[4] appear. It is in fact not true to imagine the electrons as small balls that can bounce on other heavy and large balls i.e. the atoms. For that reason a new model had to be created and this one had to include these new effects appearing at very small scales. This has led to the introduction of quantum mechanics. This is finally what material science is: the understanding of why the materials behave the way they do by the use of quantum mechanics and atomistic properties as electron orbitals, electron spins, atomic positions, electron densities, *etc.*

Material science now reaches a level that allows us to better understand the atomistic world of matter and the macroscopic properties that follow. The road was long and not always simple. However the challenge is not only the theoretical understanding of the behavior or the performance of compounds but also the experimental ability to create some new complex systems with fascinating properties. In 1981 a large breakthrough arose with

[2] In contrast to quantum physics.

[3] until it is shown that the model is wrong and needs to be revised or completely changed.

[4] i.e. non-classical.

the creation of the first scanning probe microscope (STM) that immensely increases the access we have to the nano-world. This technology made it possible to have an "image" at the nanoscale but also to control the system at the atomic level by displacing atoms one by one. These developments gave the opportunity to raise the level of our technology as we know today and to create always more powerful and smaller electronic devices for instance. However the creation and the characterization of these different systems is not an easy task and needs large and costly machines. Thankfully, an alternative exists: computer simulations. Softwares implementing atomistic models can nowadays simulate a compound and give the resulting macroscopic and microscopic properties. The power of prediction of these tools is now such as it is possible for instance to tell which material versus another is more promising to achieve a desired properties (such as ferroelectricity or multiferoism). This kind of prediction can sometimes come before it is even possible to experimentally grow the material. Obviously these simulations are based on models that have their own limitations and sometimes fail. Therefore they always need to be confirmed experimentally. However these simulations are taking a distinct approach to experiments and can provide access to complementary microscopic informations on the same system. For that reason the combination of experiments and simulations often leads to a better understanding of phenomena thanks both to the different information they can access.

A large number of different promising materials exist and some are already part of our technologies. For example semiconductor lasers and light-emitting diodes (LEDs) are now the basis of many applications such as DVD or Bluray players, at the core of our telecommunications and they largely reduced our energy consumption. Another kind of material is the carbon fiber reinforced plastics that are found in planes, cars, *etc.* since they are very strong and light materials. Such materials represent 53 % of the Airbus A350 XWB for example. Finally, nanotubes are very promising since they are the strongest and stiffest materials discovered yet and offer promising electronic properties. This work focused on another kind of promising material: the complex oxides. These are part of an emerging branch of material science with new phenomena and new physics that has already lead to many applications.

1.1.2 Peroskite oxides

Among the wide range of oxides, perovskite ABO_3 compounds have been very popular systems of research. Over the last several decades, they were intensely studied due to a large range of properties among them, related to many possible applications. The perovskite structure was first discovered in 1839 in the Oural mountains by Gustav Rose, who gave the name of Russian mineralogist L. Perovski to the compound $CaTiO_3$. Nowadays the perovskite structure refers to the generic cubic ABX_3 structure where A and B are cations and X accounts for oxygens in the case of oxides. The B cation can be viewed as at the center of the cube inside an octahedron formed by the oxygens at the face centers while the A cation is at the corners of the cube, see figure1.2a. This ideal cubic structure can also be viewed as AO and BO_2 (100) planes alternating. The B cation is usually a transition metal that forms bonding with the 6 neighboring oxygens (octahedron) thanks to d electrons. The A cation is in a 12-fold cuboctahedral[5] coordination and gives the right number of electrons needed by the B-O bondings. The formal valence of oxygen is usually O^{2-} which leads to three common different possibilities[6] for A and B: $A^{1+}B^{5+}$, $A^{2+}B^{4+}$ and $A^{3+}B^{3+}$. These 3 configurations are then giving, in (100) direction, neutral planes (AO^0, AB_2^0) or charged planes (AO^+, BO_2^-) or (AO^-, BO_2^+) respectively.

The ideal cubic perovskite is stable if the usually small B cation, the oxygens forming the octahedron and the large A cation exactly fill the space available in the cube. This can be described by the Goldschmidt tolerance factor,

$$t = \frac{r_A + r_O}{\sqrt{2}(r_B + r_O)} \tag{1.1.1}$$

where r_A, r_B and r_O are the ionic radii of A, B and O respectively.

$\rightsquigarrow t = 1$: If this stringent requirement is fulfilled (like in $BaZrO_3$) the structure is the ideal cubic structure as represented in figure1.2a. Otherwise some structural distortions appear in the cubic structure and the symmetry is reduced. Nevertheless, this criteria is only phenomenological and some distortions might appear anyway, as in $SrTiO_3$ ($t = 1.001$).

$\rightsquigarrow t < 1$: If the A atom is too small and does not fill the available space in the cube, the Goldschmidt tolerance is lower than 1 and the octahedron formed by the 6 oxygens tends to rotate to occupy as much space as possible. This instability is labeled as an antiferrodistortive motions (AFD). The oxygens are no longer at the face centers as

[5] A cuboctahedron is composed of 8 triangles and 6 squares.

[6] even 5 possibilities considering B^{6+} in the defect perovskite WO_3 and Pb^{4+} $Ni^{2+}O_3$ for instance.

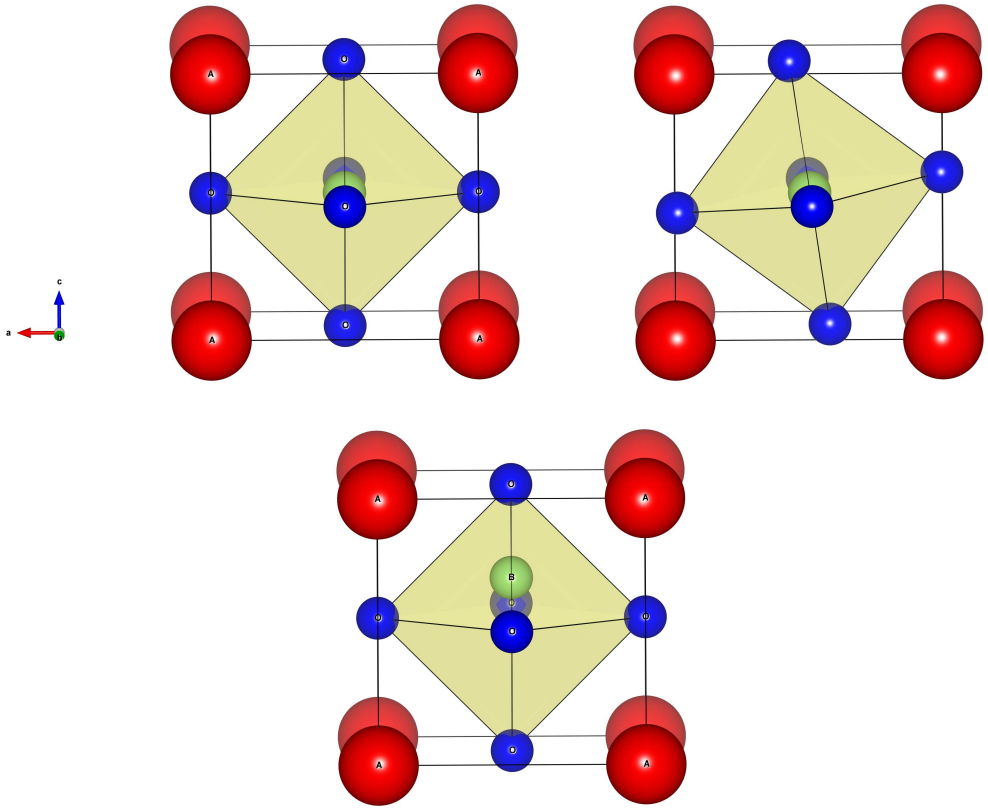

Figure 1.2: *a) The ideal perovskite structure, ABO_3. b) Example of AFD motions where the oxygens leave the face center leading to the rotation of the octahedron. c) An example of polar distortion that can condensed in the structure where B leaves the center of the cube.*

represented in figure 1.2b. Additionally the A cation can also move off-center through anti-polar distortions. This motion appears in the to the $Pnma$[7] phase [13], known to be stable for many complex oxides with $0.8 < t < 1.0$.

$\rightsquigarrow t > 1$: On the other hand if the radii of B is too small compare to A, the tolerance is larger than 1 and another instability takes place. This is the B-type ferroelectricity where B moves off-center of the cube as in figure 1.2c. Such distortions are affecting the physical properties of the materials and can for instance lead to the appearance of a microscopic dipole when the B cation moves in the same direction in neighboring unit cells. Other types of structural distortions can appear in the cubic perovskite structure however this will not be further discussed here.

Already at the structural level, ABO_3 compounds can display a wide variety of distortions (ferroelectric, anti-ferroelectric, antiferrodistortive, ...). Going further they can also ex-

[7] thanks to coupling with oxygen rotation modes.

hibit additional orders like spin ordering (ferro- or antiferro magnetism), charge ordering, orbital ordering or Cooper pair order, as represented in figure 1.3.

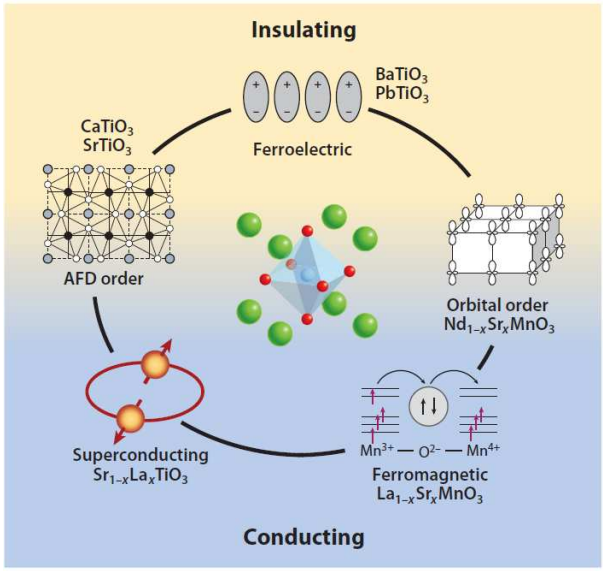

Figure 1.3: *The different kinds of ordering that appear in ABO_3 complex oxides (green, blue and red balls respectively). A huge range of functional properties arise in these materials thanks to the complex couplings between orders, as the metal-insulator transitions for instance.*

1.2 Tuning the degrees of freedom

With the huge wealth of different orders in complex oxides one could expect to combine them in a new compound. For instance, one can expect to obtain a system that combines ferroelectricity and ferromagnetism. That would be the opening for a possible magnetic control on the electric field and *vice versa*, potentially leading to new spintronic devices. Still, only a few oxides combine these 2 orders and unfortunately they are not necessarily coupled. In fact, in bulk, the different orders are often exclusive and they compete with each others. A well known example is in $SrTiO_3$ where both FE and AFD distortions are expected to appear. However the more stable phase only contains AFD motions and the FE ones are canceled through couplings with AFD motions and quantum fluctuation [14]. The same is true between ferroelectricity and magnetism [15], explaining the small amount of oxide compounds with both orders.

An alternative pathway is to combine different orders by acting with an external parameter like an electric field or a mechanical constraint. In this way, it is possible to tune

some orders and to stabilize them while they would not appear in the formal compounds. A nice example is the previous $SrTiO_3$ system that displays a paraelectric ground state with AFD motions at low temperature. However, if the lattice is under mechanical constraints, a paraelectric to ferroelectric transition can be observed [16]. The strain more strongly couple with FE motions making them dominant beyond a critical threshold.

Creating an interface offers a nice alternative playground to couple order parameters through various phenomena such as pressure (strain), frustration, *etc.*, see figure 1.4. But then, when such an interface is created between 2 distinct compounds with properties A and B respectively, what are the resulting properties? This new material can behave as the combination of the 2 others i.e. $A + B \rightarrow (A + B)$, or presents completely new properties such that $A + B \rightarrow C$.

Amount the large different constraints, this work will focus mainly on how a symmetry breaking and an electrostatic coupling created by an interface between 2 different materials can lead to completely new physical effect at this interface. For that reason we describe in the next section what exactly an interface is. Further informations on complex oxide heterostructure interfaces are available in recent reviews by Zubko *et al.* [17] and Yu *et al.* [18].

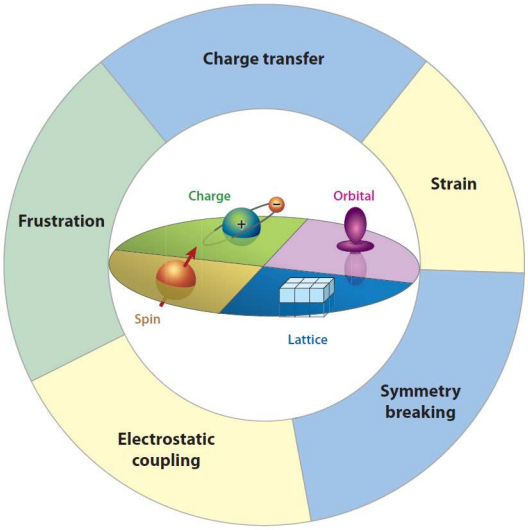

Figure 1.4: *The degrees of freedom in oxides and the constraints that appear at interface that can influence them.*

1.3 Interfaces

1.3.1 Generalities

In a perfect and infinite crystal the atoms interact with the neighboring environment which is the same everywhere. However a real sample has a finite dimension and an interface between the material and the vacuum (or the air) is then formed. Close to that interface, called a surface in this case, the atoms are not in the same environment than in the bulk and their behavior can be altered. The heterostructure, which consists of a series of layers of two or more compounds, is another way to build an interface, represented in figure 1.5. As for the surface the atoms at the boundary are not in the same environment than in the bulk infinite compounds and completely new effects can arise from this lowering of symmetry and various consecutie effects as illustrated in figure 1.4. The more common and usual interface, since it covers ~ 70 % of the surface of our planet, is the water-air one. This interface behaves as an elastic membrane and has a property that is completely missing in the two formal compounds, the surface tension. Closer to our working field, lasers, transistors or solar cells all involve interfacial phenomena which are in fact a key feature of many applications and technologies. The best example is probably the metal-oxide-semiconductor field-effect transistor (MOSFET) that is present in almost every electronic system. This transistor allows to tune the carrier density (and therefore the resistance) through an electric field thanks to interfacial effects between SiO_2 and Si.

The creation of a heterostructure can be achieved through the deposition of a film on the surface of a substrate via different processes (see later). When there is some degree of registry between the atomic positions of the substrate and the film, the result is called an epitaxy (the mismatch has to be small enough). The atomic structure of the film has to fit with the one of the substrate at the interface, although the two materials do not need to have the same crystal class. In the case of a thin film deposited on the surface of a thick substrate, it is the film that fully resizes to fit to the geometry of the substrate. In the two spatial directions of the surface, the film is expanded or contracted compared to its natural size. The relative difference of the lattice parameters of the distorted and undistorted film defines the epitaxial strain. Additionally, perpendicularly to the surface, a strain arises due to the Poisson effect[8]. If the film expands in plane compared to the

[8] As it is for a rubber which is thiner when expanded.

undistorted case, the perpendicular direction is contracted and vise versa. In the case of such epitaxial strain the atoms are not at their usual distances and some properties, like the ferroelectric, magnetic or orbital orderings, can be affected due to the change in the orbital overlaps for instance. The epitaxy is then one of the possibilities offered to affect the different degrees of freedom of a system.

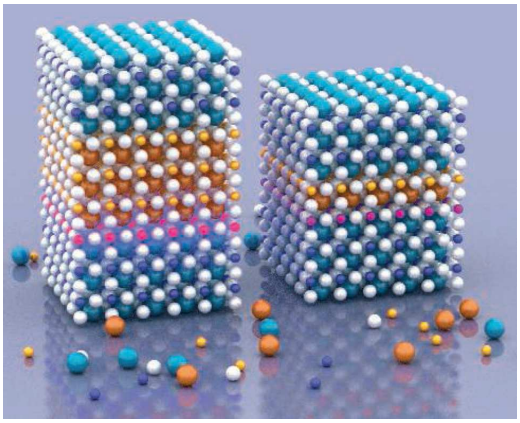

Figure 1.5: *Schematic representation of an oxide heterostructure. Figure adapted from [19].*

The growth of heterostructures highly depends on the quality of the substrate. For semiconductors the techniques are well developed giving rise to a very accurate control on the defects leading to almost defect free surface systems. However in the case of oxides, these techniques were lacking until recently. The lack of direct applications and the experimental limitations made these systems less studied despite the wealth of physical properties of oxides. Nowadays the techniques have been developed and it is possible to reach sufficient control of the substrate to have practical studies. Although these processes are still at their infancy, it is possible to obtain good $SrTiO_3$ substrates via chemical treatments [20–22] which is now the most communally used substrate. A good quality for a $SrTiO_3$ substrate means perfectly terminated by either single SrO or TiO_2 layers for a (001) surface. The growth of the substrate is not an easy task and will not be discussed further here.

The case of the film deposition is just as important since the growth conditions have an effect on the studied phenomena. We thus need to describe the different methods and parameters of the growth in order to have a naive understanding of these parameters. Nowadays the most popular growth methods of oxides are the pulse laser deposition (PLD) and the molecular beam epitaxy (MBE). PLD uses high power laser pulses that ablates the targeted material creating a highly luminous plasma. The ions have a high velocity and are redirected toward a heated substrate where they condense and form

the film. The whole is enclosed in a deposition chamber that allows the control of the oxygen atmosphere. This film is affected by many variables such as the oxygen partial pressure, the laser fluence or the substrate temperature, giving opportunity to control the film properties. However to control the growth and to reach a film with specific properties, a lot of time and effort are needed. MBE uses ultra high vacuum chamber where the material is heated and then migrated toward the sample where it is adsorbed at the surface and creates the film. With MBE the species have much lower kinetic energy when they approach the substrate. These two methods are physical deposition methods. During the deposition it is possible to use the reflection high-energy electron diffraction (RHEED) process to control and analyze the growth. The pattern of the electrons that diffract on the surface informs on the roughness of this surface. These methods are precise enough to adjust some parameters in order to obtain a specific system with for example 5 additional per cent of A atoms or a system as close as possible to the ideal case. It also allow controlling precisely the number of layers that have been deposited. Unfortunately, they are also rather slow and complicated compared to the case of semiconductors.

1.3.2 New physics at the interface

Many practical applications using semiconductors are based on interfacial effects. However apart from this interface, the electrons are almost free and there is no specific interaction leading to particularly new attractive property. On the other hand, the oxides display many different properties such as magnetism or ferroelectricity thanks to a complex interplay between the latice, magnetic, orbital and charge degrees of freedom. We can thus expect to obtain very interesting systems and new physical effects and mechanisms at the interface of these compounds. The strain is a way to act on the degrees of freedom but charge transfer, symmetry breaking, frustration and electrostatic coupling can also affect these degrees of freedom (in different ways), as schematically represented in figure 1.3.

When the interface is formed, between two compounds or with the vacuum, it is important to know if that one is polar or not. Indeed, for a polar interface the electrostatic coupling is important. The simplest method to determine whether or not an interface is polar, as first introduced by Tasker [23], is to use the formal charge of each ions as a point charge without any relaxation[9] (neither electronic or ionic). The interface is then polar

[9] Also referred to as bulk frozen surface.

if the bulk unit cell contains a dipole moment. Some examples of polar and non-polar systems are given in figure 1.6. This naive point of view appears to be, by chance, correct for centrosymmetric structures as discussed by Bristowe *et al.* [24] and nicely shown by Stengel [25] who succeeded to apply the concepts of the new theory of polarization in a polar surface case. To summarize, an interface is polar if the bulk polarization perpendicular to the interface of material A and B are not equal as describe by the interface theorem in reference [26]. If the system appears to be polar, it is equivalent to consider the surface net charge ($\mathbf{P}.\hat{\mathbf{n}}$) at each side of the interface. However, such charges at the interface between two semi-infinite systems produce a diverging potential and by this fact a highly unstable system. This problem is referred to as the polar catastrophe. Such systems with a diverging potential are not supposed to appear in nature and to be canceled, some charge screening should appear. However in the case of a thin film the change of potential is finite and the film is capable of handling that. In that case a dipole appears across the film due to the coupling of the two interfaces.

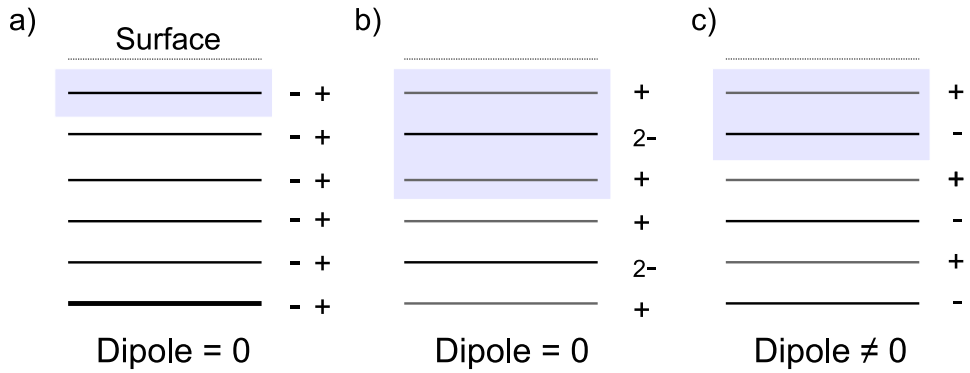

Figure 1.6: *Example of the ionic surface classification by Tasker. a) Same charges for cations and anions of a plane leading to neutrally charged planes (type 1). b) Zero net dipole moment despite the charged planes (type 2). c) Charged planes and net dipole moment (type 3). Figure adapted from reference [23].*

By creating such a polar interface between two compounds one might expect to create a stable structure if the thickness of the film is small enough. However for larger thicknesses, at some point, the system becomes unstable and should undergo some mechanisms to cancel the net charge density at the interface/surface. These can be of various types.
The first kind are extrinsic mechanisms that involve external sources. For example the molecular adsorption or the change of surface/interface stoichiometry are both doping the surface which screens the system. The interface between the semiconductors Ge and GaAs is a well known case were atomic reconstruction cancels out the diverging

potential [27].
The second kind rely on intrinsic mechanisms that only involve internal sources such as the electronic reconstruction or the dielectric screening.

The most popular example of polar interfaces, which is becoming a textbook case, is the $LaAlO_3$-$SrTiO_3$ (001) system [1]. The reason is that unlike semiconductors, oxides can acquire a mixed-valence ionic character by the Ti atoms. The polar discontinuity can thus be balanced by the fact that, at the interface, Ti^{4+} can become $Ti^{3.5+}$. In oxides, the electronic reconstruction is then a possible mechanism to avoid the polar catastrophe. Nevertheless, since the discovery of this system in 2004, a long and tenacious debate is wide open concerning the real origin, intrinsic or extrinsic, of the reconstruction in $LaAlO_3$-$SrTiO_3$ system. The next section is dedicated to the $LaAlO_3$-$SrTiO_3$ heterostructure, the properties that arise at the interface and the possible mechanisms at the origin of the reconstruction.

1.4 The $LaAlO_3$-$SrTiO_3$ interface

1.4.1 General overview

A landmark experiment realized in 2004 by Ohtomo and Hwang [1] showed that a highly conductive layer appears at the interface of the two insulators, $LaAlO_3$ (LAO) and $SrTiO_3$ (STO). This phenomenon is characterized by a two-dimensional electron gas (2DEG) confined in a few $SrTiO_3$ layers close to the interface [28]. In addition to that metallic interface, other exciting phenomena have been discovered since that time, such as superconductivity [29], magnetic transport [30], a quantum phase transition [31], huge field effects and magnetotransport [31, 32] or thickness and dimensional effects [32, 33]. Most of these effects are not present in the compositional materials, which are insulating and non magnetic. The $LaAlO_3$-$SrTiO_3$ system is a perfect example of new physical phenomena that appear when an interface is created modifying the different internal degrees of freedom. The $LaAlO_3$-$SrTiO_3$ interface is now a prototypical example of a polar/ non-polar interface and is one of the most important and investigated discovery of the last 10 years within the field of oxides with more than 1600 citations of the original paper at this time[10]. A brief overview of the major developments of the $LaAlO_3$-$SrTiO_3$ field is given in the next sections. Both theoretical and experimental key results are given concerning

[10]Source by google scholar.

the origin, the properties and the parameters that can affect the formation of the 2DEG.

1.4.2 Original explanation: The polar catastrophe scenario

Imagine two compounds with the property Black and the other White. If now these two compounds form a new system by mixing them, or creating an interface between them, you can expect to have: the properties Black or White, if one dominates, or the property Grey if they are almost equivalent. If you are lucky, maybe the new property will be something like Blue or Yellow, which is already quite interesting and unexpected. However, if it is really your lucky day, by mixing properties Black and White, you can end with the properties of a colored rainbow. This is the $LaAlO_3$-$SrTiO_3$ system.

In the seminal paper of Ohtomo and Hwang [1] the heterostructure is created by growing a $LaAlO_3$ thin film on a thick (001) oriented $SrTiO_3$ substrate. In this specific orientation (001), two different interfaces can form, SrO-AlO_2 and TiO_2-LaO, respectively called p-type and n-type interfaces, as represented in figure 1.7. Through Hall transport measurements, the authors have shown that the p-type interface remains insulating whilst the n-type interface displays a high electron mobility at the conducting interface. Afterwards, Nakagawa and Hwang [34] showed that the conductivity is due to the presence of electrons in the $SrTiO_3$ substrate close to the interface with a density of 0.7 electron per unit cell area (e^-/S). The origin of this two dimensional electron gas (2DEG) is introduced in reference [1] as what we call the polar catastrophe scenario. The compositional materials in the specific orientation, (001), are formed of $(LaO)^+$ and $(AlO_2)^-$ layers for $LaAlO_3$ and $(SrO)^0$ and $(TiO_2)^0$ for $SrTiO_3$. The alternatively charged layers in LAO is the key element of the polar catastrophe in addition to the symmetry breaking that appears when the interface is created with the non-polar STO substrate. With Gauss's law, or simply a capacitor in series approach (see chapter 3), one can show that an electric field is present in LAO. For each additional LAO unit cell i.e. for increasing LAO thicknesses, the electric potential increases without any physical limit, hence referred to the polar catastrophe. The system is then highly unstable and any mechanism that can reduce the diverging electrostatic energy by canceling the electric field in LAO should occur. Nakagawa and Hwang showed that the diverging potential can be prevented by transferring 0.5 e^-/S at the n-type interface. For the p-type interface the screening is realized through the transfer of 0.5 h^+/S but is also achieved by the appearance of 0.25 oxygen vacancies per unit cell area. This is in agreement with the 0.3 oxygen vacancies

that the authors found and the remaining insulating interface. This electronic transfer to prevent the diverging potential is referred to as the electronic reconstruction mechanism (discussed in more details in chapter 3) but oxygen vacancies or atomic interdiffusion are other mechanisms that can also prevent the "polar catastrophe" and will be discussed later in this chapter.

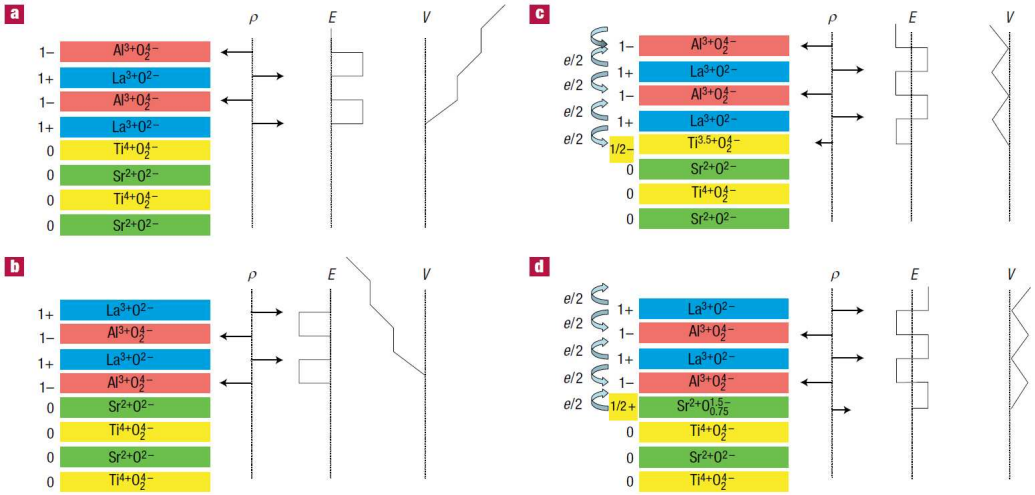

Figure 1.7: *The polar discontinuity at the LaAlO3/SrTiO3 heterostructure. The planar formal charge ρ, the electric field E and the potential V is represented for the n-type (a and c) and p-type (b and d) interfaces. Top and bottom correspond respectively to unreconstructed and reconstructed cases. Figure is adapted from reference [34].*

1.4.3 Role of oxygen vacancies

It is well known that $SrTiO_3$ is very sensitive to doping and that $SrTiO_{3-\delta}$ undergoes a metal/insulator transition even for a small defect density [35]. Even if the STO substrate is insulating before the growth, oxygen vacancies can affect, or even lead to, the metal/insulator transition in LAO-STO. Already in the original paper [1], the growth conditions are identified to greatly affect the gas properties (mobility, sheet conductance and electron densities). Several papers studied the oxygen partial pressure, p_{O_2}, and the annealing process of samples [1, 28, 36–38] showing 3 different regimes: low p_{O_2} ($\sim 10^{-6}$ mbar), high p_{O_2} ($\sim 10^{-4}$ mbar) and very high p_{O_2} ($\sim 10^{-2}$ mbar).

In the case of low oxygen partial pressure and no annealing process before transport measurements, Ohtomo *et al.* [1] found a large electron density (3×10^{14}-10^{17} cm^{-2}), a high Hall mobility (10^4 cm^2.V^{-1}.s^{-1}) and a sheet resistance around 10^{-2} Ω/S. These measurements correspond to the low p_{O_2} without annealing process since they are obtained by

several other studies. For high p_{O_2} the density reduced significantly to 10^{13}-10^{14} cm^{-2} in better agreement with the 0.5 e/u.c.^{2} (or 3.3 10^{14} cm^{-2}) expected by the polar catastrophe model. In addition the sheet resistance can increase by 2 orders of magnitude. On the other hand, some samples remain insulating if grown [37] or annealed [36] under very high partial pressure despite the polar catastrophe prediction. Finally for samples grown at low partial pressure, where typically the carrier densities are $\approx 10^{16}$-10^{17}, but annealed after, the densities reduce to $\approx 10^{13}$-10^{14} cm^{-2}.

All these results, summarized in reference [6], seem to imply that the electronic reconstruction mechanism is dominant for systems with a small quantity of vacancies and that, a very high electron density is obtained due to the doping properties of oxygen vacancies in non annealed or low partial pressure samples. Unfortunately, this simple point of view is unsatisfying and the electronic reconstruction mechanism suffers some problems (discussed later). For instance the insulating interface found for very high partial pressure samples (but also the p-type interface), questioned the real role of oxygen vacancies in the $LaAlO_3$-$SrTiO_3$ system.

In conclusion, the oxygen partial pressure, i.e. the oxygen vacancies, and the annealing process play a huge effect on the 2DEG and its properties. However, these results are not enough to rule out other mechanisms and the mechanism at the origin of the 2DEG is still a highly debated question.

1.4.4 Critical thickness

Another interesting feature of the $LaAlO_3$-$SrTiO_3$ interface is the thickness dependence. Even if samples grown at low p_{O_2} are always conducting due to oxygen doping, samples grown at higher partial pressure ($\sim 10^{-4}$ mbar) remain insulating unless the $LaAlO_3$ film thickness is large enough. The specific thickness at which the insulator-metallic transition occurs is called the critical thickness and was shown to be 4 unit cells in references [32, 38] and by many other works. These works show that the sheet carrier density is null or undetectable below the critical thickness but suddenly jumps after, see figure 1.8. Nevertheless the majority of these works were generally based on transport measurements. X-ray measurements have been realized on the same kind of samples by Sing *et al.* [39] where they show that the sheet carrier density is non zero even before the critical thickness and that this density increases with the $LaAlO_3$ film thickness, see figure 1.8. To explain the non zero carrier densities obtained by X-ray below the critical

thickness, the authors proposed the existence of immobile carriers.

Additionally, the critical thickness can be reduced compared to the usual 4 u.c. by adding a STO capping layer on top of the $LaAlO_3$ thin film. Huijben *et al.* [40] have shown a non zero sheet density for only 2 u.c. LAO films and Pentcheva *et al.* [41] have shown the same effect with *ab initio* calculations.

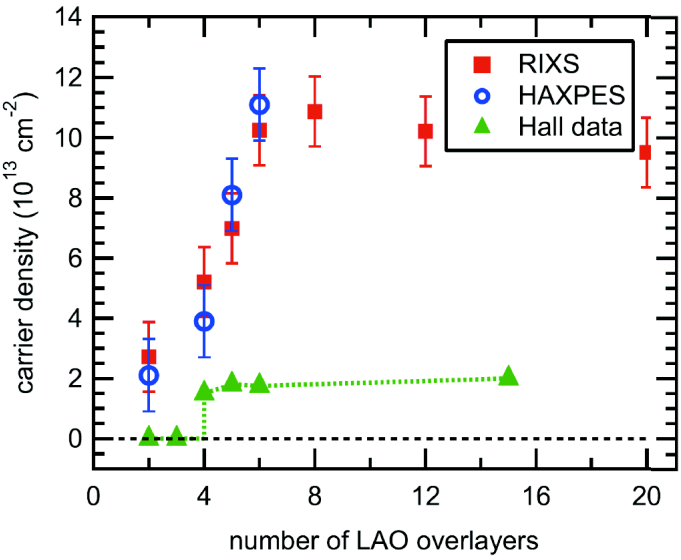

Figure 1.8: *The interface electron density measured via Hall transport [32], hard x-ray photoelectron spectroscopy (HAXPES) [39] and resonant inelastic x-ray scattering (RIXS) [42]. Figure adapted from reference [42]*

1.4.5 Electron confinement

The oxygen partial pressure and the annealing process influence the gas properties (charge density and mobility) but also its spacial extension. In low partial pressure samples (10^{-6} mbar and not annealed), the gas spreads over 10-100 μm in STO. The gas is then not confined at the interface and has a 3D character, as observed by [36, 43]. The electrons probably originate in that case from defects as oxygen vacancies that spreads into STO. On the other hand, Bastelic *et al.* [28] showed, via cross-section conductive tip atomic force microscopy measurements, that annealing the samples changes the spacial extent to a few nanometers from the interface. In that case, as for samples grown at high-partial pressure (10^{-4} mbar), the gas is confined at the interface and has a 2D character, see figure 1.9. It was then suggested that two types of carriers exist, a first spreads in STO coming from defects and a second localized at the interface with possible intrinsic origin. Depending on the method used for the measurements, but probably also on the different

samples, some works showed that the 2D gas lies between 4 nm and 10 nm [39, 44] with the majority of the electrons confined in the first unit cell of STO [45]. Furthermore, it was shown that the gas is composed of two types of (intrinsic) carrier, one that rapidly decays, confined close to interface (2 nm), and a second that extends into $SrTiO_3$ (11 nm) [46].

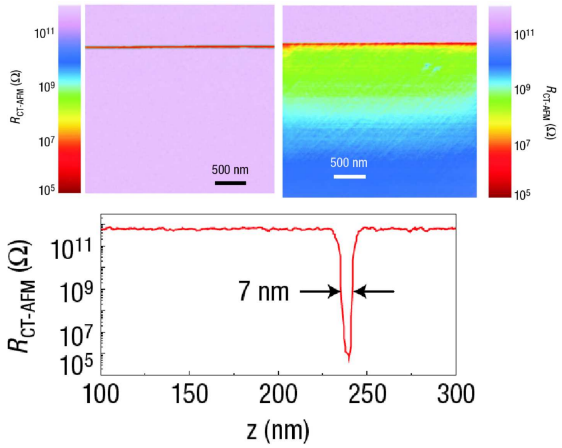

Figure 1.9: *Top: Comparison of conducting tip atomic force microscopy mapping for oxygen-rich (left) and oxygen-poor (right) samples. Bottom: The resistance profile across the interface for the oxygen-rich case showing the electron localization within a few nm. The figure is adapted from [28].*

In $SrTiO_3$, the first empty energy states (right above the Fermi level) are the $3d$ t_{2g} orbitals of Ti^{4+}. When the $LaAlO_3$-$SrTiO_3$ system is doped, the electrons partially fill the $3d$ states and Ti^{4+} changes to $Ti^{3.5+}$ as shown by atomic resolution electron energy loss spectroscopy (EELS) [34]. In this system, the orbital ordering of the ${t_{2g}}^{11}$ states is important since it affects the properties of the gas (see chapter 6). The t_{2g} states, degenerate in cubic STO, are split into the lower d_{xy} and the degenerate d_{yz} and d_{xz} states due to the interface symmetry breaking, as observed in reference [47]. In addition, some other works showed that 2 states, at least, are occupied by the interfacial electrons [48, 49], corresponding to localized and delocalized carriers.

DFT calculations [50–52] also showed the splitting of the t_{2g} orbitals with the lowest energy being mainly of d_{xy} character. Popovic *et al.* [53] also showed that this orbital has a strong 2D character whilst the d_{xz} and d_{yz} are more 3D-like and expands into STO. Calculations realized by Popovic [53] and by Son [51] are realized for different charge densities showing a large evolution of the band structure with carrier density. Popovic

[11] $3d$ is split into lower t_{2g} and higher e_g states in cubic perovskites due to the crystal field splitting of the oxygen octahedral environment, see chapter 6.

et al. [53] also stressed that due to the 2D-like states the electron should be localized by Anderson mechanism. This possibly gives an explanation on the low charge density obtained through Hall measurements [32] compared to the 0.5 e/S of the polar catastrophe model.

In fact the exact reason why the electrons are confined close to the interface is not easy. Usually band bending is the concept that lead to confinement in metal-oxide-semiconductor interfaces. However Janicka *et al.* [54] suggested that the latest effect is not enough and that formation of metal-induced gap states may play an important role spreading more deeply the electrons into STO. On their side, Chen *et al.* [50] proposed a large Ti-La coupling that lowers the Ti 3*d* levels at the interface that becomes energetically favorable for the electrons and possibly explain why the holes formed at the p-type (AlO_2-SrO) interface are delocalized. However, Stengel, in the supplementary material of reference [55], showed that it costs some energy to move the electrons away from the interface. Additionally, the cost of energy is inversely proportional to the static dielectric constant of STO. Stengel concludes by saying that the dielectric properties of $SrTiO_3$ is very important to determining the 2DEG confinement contrary to the Ti-La orbital couplings proposed by reference [50].

Finally, we need to mention the correlation effects that appears in oxides and create new properties that were not present in the formal materials. Evidence of a magnetic behavior was provided by Brinkman *et al.* [30] who showed a magnetic hystereris loop and transport properties associated to a large negative magnetoresistance. Additionally this system presents superconducting behavior [29] which was shown to be controlled by an electric field effect [31]. Even if they are usually highly exclusive, superconducting and ferromagnetic phases have been found in $LaAlO_3/SrTiO_3$, as phase separated [56] or coexisting [57, 58].

1.4.6 Structure and lattice distortion

Due to a slightly shorter lattice parameter of the film compare to the substrate, the epitaxy creates an in-plane tensile strain that should reduce the out-of-plane lattice parameter of $LaAlO_3$ (see chapter 3). However Maurice *et al.* [59] have shown that it is in fact an expansion that is observed, especially at the interfacial octahedra. The explanation of a Jahn-Teller like distortion was given however Willmott *et al.* [60] only attributed these deviations to intermixed cations at the interface. Using X-ray diffraction methods,

Pauli *et al.* [61] have shown that atomic displacements in $LaAlO_3$ are in agreement with the presence of an electric field since they measured an off-centering of the cations with respect to the perovskite LAO structure.

1.4.7 Intermixing and disorder

The $LaAlO_3$-$SrTiO_3$ system is far from being perfect and some intermixing occurs at the interface as shown by Nakagawa *et al.* [34]. In addition, Willmott *et al.* [60] have shown that La-Sr mixing occurs in a larger range than the Al-Ti mixing beside the fact that La and Sr are twice larger suggesting a natural tendency of the system. Furthermore, Qiao *et al.* [62] have shown, on the basis of density functional theory calculations, that intermixed interfaces are thermodynamically more stable. Such defects have been suggested by reference [7] to be a possible origin of the doping of the interface and then the origin of the 2DEG. This will be discussed in section 1.5. Such a mixing can affect the transport properties by creating trapping states for instance or by changing the dipole at the interface. However they cannot explain why the interface is conducting (the solid solution is insulating). Recently the effect of such intermixing but also of (non)stoichiometric exchange as been studied by Breckenfeld *et al.* [63] showing the effect on sheet carrier densities and mobility. For instance only a small deviation from unity of the La:Al ratio leads to a decrease of charge density by one or two orders of magnitude.

1.4.8 Toward applications

Another amazing discovery is the possibility to reversibly switch the metal/insulator transition by a gate voltage. This property is obtained when the $LaAlO_3$ film is grown with a thickness just below the critical [32]. Later, another experiment [64] reproduced this field effect using a biased atomic force microscopy (AFM) tip, again in 3 unit cells thick films. The authors were able to write and also erase conducting nano-regions in the LAO insulating film. Additionally, a transition from insulator to a superconducting state was obtained by the same field effect, at low temperature [31]. These experiments opened the way to use oxides for potential electronic device applications and storage devices with high capacity. Moreover they offer a new approach to understand the formation of the 2DEG and its conductivity. For instance, in reference [64] the authors proposed that oxygen vacancies, but this time at the LAO surface[12], could activate the metal/insulator

[12]The previous kind of doping by the oxygen vacancies was due to defects in the $SrTiO_3$ substrate.

transition, a theory supported by density functional theory calculations. Later, another mechanism was suggested when it was realized that the switching process was linked to water in the environment [65]. Finally, few systems, as field-effect transistors [66] and nano-devices [67, 68] have been recently realized proving the potential applications of the heterostructure.

1.5 Controversial origin of the 2DEG

Introduction

It has now been 10 years since the creation of a 2DEG at the interface of the $LaAlO_3$-$SrTiO_3$ system has been discovered. However it has now been also 10 years that a strong debate is open on the mechanism at the origin of this gas. People have in fact their own ideas on this origin depending on the studies they rely on and how they interpret them. An example of how this origin is controversial is given in figure 1.10 where the authors of references [7] and [69] are giving their point of view concerning these mechanisms. For someone that is not working in the field, it is difficult to understand why the electronic transfer mechanism seems to perfectly explain all the experiments in one case while it is not for the other case. This naive comparison[13] perfectly reflects the confusion concerning the mechanism at the origin of the 2DEG. Moreover, this comparison also shows the rapid evolution of the topic with the additional mechanisms that have appeared between these two works.

These two mechanisms, electronic reconstruction and surface oxygen vacancies, are electric field driven. However, in references [70–74] the authors found an unexpected conductivity at the interface between a $SrTiO_3$ substrate and an amorphous $LaAlO_3$ film, which is clearly non-polar. In addition, no signature of an electric field, a very important feature for the 2 previous mechanisms, is found in a few works [75, 76], raising doubt that the polar catastrophe is a real problem and is at the origin of any mechanism. In fact, it was shown recently that the conductivity is no longer observed in the amorphous systems [74] if they are post-growth annealed. Moreover, some experiments do find signatures of a built-in electric field [61, 77–79]. However, the values which are found are smaller than expected by the field driven mechanisms and can be attributed to the presence of metal

[13] A complete explanation of the complex reasons why a observation is not in agreement with a mechanism and why it can still be valid for some other effect should be done.

Table 1 | Suggested origins of observed conductivity.

Origin of conductivity	Oxygen vacancies	Interdiffusion	Electronic reconstruction
$LaAlO_3$ on TiO_2-terminated $SrTiO_3$ conducting (refs 1,3,4,10)	✓	✓	✓
$LaAlO_3$ on SrO-terminated $SrTiO_3$ insulating (refs 1,3)	✗	✗	✓
Amorphous $LaAlO_3$ on $SrTiO_3$ insulating (ref. 4)	✗	✗	✓
≤3 UC $LaAlO_3$ on $SrTiO_3$ insulating (refs 1,4,10)	✗	✗	✓
>3 UC $LaAlO_3$ on $SrTiO_3$ conducting (refs 1,4,10)	✓	✓	✓
Thickness-dependent potential in $LaAlO_3$ (ref. 12)	✗	✗	✓
Density of states consistent with conductivity model (ref. 13)	✗	✗	✓
Thickness-dependent buckling of $LaAlO_3$ planes (ref. 14)	✗	✗	✓
Reversible conductivity of 3 UC $LaAlO_3$ on $SrTiO_3$ induced by electric fields (refs 1,2,10)	✓	✗	✓

A summary of how the mechanisms suggested to be the origin of the observed conductivity agree (ticks) or disagree (crosses) with experiments performed on $LaAlO_3/SrTiO_3$ interfaces. This list is not comprehensive. References to the experiments described by each column are given. UC, unit cells.

Interface structure	Experimental Observations	Polar Catastrophe	Cation Mixing	V_O at interface	V_O at surface	Unifying mechanism
n-type	1. Critical thickness (L_c) = 4 uc	✔	✖	✖	?	✔
	2. 2DEG density < 0.5 *e*/*S*	✖	?	✖	✖	✔
	3. Weak *E* in $LaAlO_3$ for $n_{LAO} < L_c$	✖	?	✖	✖	✔
	4. Weak *E* in $LaAlO_3$ for $n_{LAO} \geq L_c$	✖	✖	✖	✔	✔
	5. $LaAlO_3$ surface: insulating	✖	?	?	✔	✔
	6. Interface: cation intermixed	✖	✔	✖	✖	✔
	7. Interface **magnetism**	✖	?	✖	✖	✔
p-type	1. Interface: insulating	✖	?	✖	?	✔
	2. $LaAlO_3$ surface: insulating	✖	✖	?	?	✔
	3. Interface: cation mixed	✖	✔	✖	✖	✔
	4. Interface **magnetism**	✖	?	?	✖	✔

The symbol of '✔' and '✖' mean that the mechanism agrees or disagrees, respectively with the experimental observation. The '?' symbol denotes uncertainty.

Figure 1.10: *A list of the possibility, or not, for some mechanisms to explain important experimental observations. This show the complete disagreement of the 2 authors, [7] and [69], and the confusion and debate around the origin. In addition, it shows the confusion between the electronic reconstruction and the polar catastrophe (see next section).*

electrodes.

This discussion tries to show, using 12 studies, the huge confusion about the origin of the conductivity in the $LaAlO_3$-$SrTiO_3$ system. However this topic gathers 100 times more studies. It is for those reasons that, another part of the community believes that only external defects (see figure 1.11), such as intermixing, adsorbate at surface or oxygen vacancies in $SrTiO_3$, are doping the system and creates the gas.

This section gives a description of the different mechanisms that can lead to the 2DEG with their agreements and disagreements with experiment. None of these are highlighted compare to another and only a brief description is given. The idea is to give a basic and simplified description of the mechanisms, not a new and isolated point of view. The reader can find a more complete description and comparison of these mechanisms in a recent review by Bristowe [12].

The question of how the electronic gas is created can be avoided in the sense that what may be important is the fact that it is possible to create this gas that has amazing properties. However depending on the mechanism at the origin of the gas, different

properties can arise since for example oxygen vacancies at LAO surface creates defects that have a direct influence on the carriers mobility [1]. The real mechanism can thus have a direct impact on the properties of the $LaAlO_3$-$SrTiO_3$ system. Additionally, without knowing the real mechanism at play, it is impossible to predict new systems which show similar phenomena. We present in this section the 4 main mechanisms that are possibly at the origin of the 2DEG. First and second are the Zener breakdown and the surface redox reactions respectively that both need the build-in electric field in $LaAlO_3$ to occur as a result of the polar discontinuity at the interface. The two other mechanisms are the oxygen vacancies that forms in $SrTiO_3$ and any type of cation intermixing. Both do not need any electric field to occur.

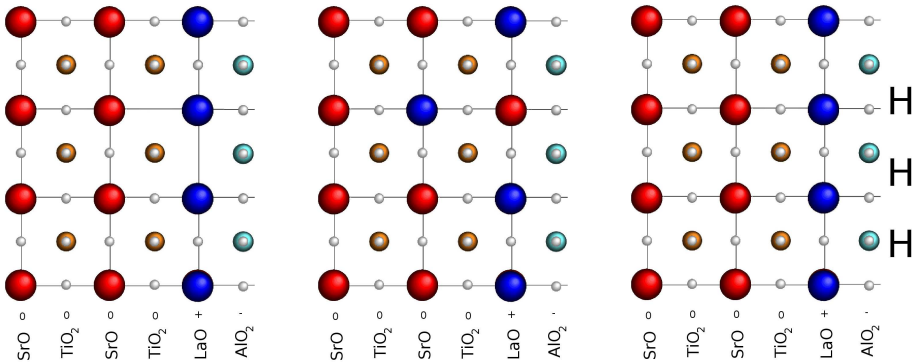

Figure 1.11: *Schematic picture of $LaAlO_3$-$SrTiO_3$ with extrinsic defects. The oxygen vacancies, intermixing and hydrogen adsorbate at respectively left, middle and right.*

Technical vocabulary

Before the description of the different mechanisms, a small technical detail has to be fixed. Indeed, the usual intrinsic and extrinsic concepts are not really well defined and sometimes hard to distinguish. For instance are the oxygen vacancies coming from a natural way for the system to decrease the electrostatic potential or is it due to defects creation during growth? For this reason, in this work, we split the mechanisms in two different types. First one relies on an electric field arising from the polarization mismatch between LAO and STO and the second kind is not based on the need of this built-in electric field. In addition we need to clarify the usual confusion between the polar catastrophe and the electronic reconstruction. The polar catastrophe was attributed to systems in which the electric potential diverges due to the creation of an interface between a polar and a non-polar material (polar discontinuity). The electronic reconstruction is the transfer of 0.5 electrons per two-dimensional unit cell from the $LaAlO_3$ surface to the $SrTiO_3$ interface

as a result of Zener breakdown. It is then one of the possible mechanisms that can explain the creation of the 2DEG by fixing the polar catastrophe problem.

The electronic reconstruction (Zener breakdown)

The electronic reconstruction is a direct consequence of the polar/non-polar interface that is formed in the $LaAlO_3$-$SrTiO_3$ system. Already in 2000, Noguera showed[80] that a screening charge on the surface and the interface is needed to avoid the polar catastrophe of such systems, usually realized through an exchange of cations in semiconductors. However for Ti based compounds, the mixed valence state of the titanium (Ti^{3+} and Ti^{4+}) allows for the electronic reconstruction. Indeed, the screening charge can be obtained by an electronic transfer of 0.5 electrons per 2 dimensional unit cell, from the LAO surface to the STO interface and "If the electrons can move, the atoms do not have to " [34]. This model is rather simple since it is directly based on electrostatics, Gauss's law and the use of formal charges disregarding any covalency of the bonds[14]. However it captures the main physics of the pristine polar non-polar interface and it is reinforced by the fact that a metallic interface is found for instance between $SrTiO_3$ and $LaTiO_3$ [81], $LaGaO_3$ [82] and $LaVO_3$ [83] which are also II-IV/III-III perovskite interface.

A feature that comes naturally from the electronic reconstruction is the thickness dependent metal-insulator transition, first observed in references [32, 38]. For very small thin films, $LaAlO_3$ is able to handle the built-in electric field and the system is insulating. This can be visualized by a simple band model where the valence and conduction bands of LAO are bent by the electric field, the intensity of which is linked to the dielectric constant and the net charge. As the thickness increases, the electric band gap of the system closes leading to the usual concept of Zener breakdown in a capacitor. The energy of the system is then reduced if electrons at the surface of LAO, which have a high energy due to the potential and have oxygen $2p$ character, are transfered to the Ti $3d$ states at the interface. The transfer then creates holes that remain in the O $2p$ states at the surface of LAO. The electronic reconstruction is schematically represented in figure 1.12.
The transferred charge density is less than the 0.5 electron per 2 dimensional unit cell, a value that is only recovered for an infinitely large thickness. As further discussed in chapter 3, this model predicts a critical thickness between 4 and 6 unit cells of $LaAlO_3$ which is in good agreement with the theoretical [64] and experimental [32] results.

[14]The reason why will be discussed in chapter 3

The main features of this mechanism are the pristine interface and surface, the built-in electric field, a natural explanation for the critical thickness and a progressive charge transfer. A complete description of this mechanism is done in chapter 3.

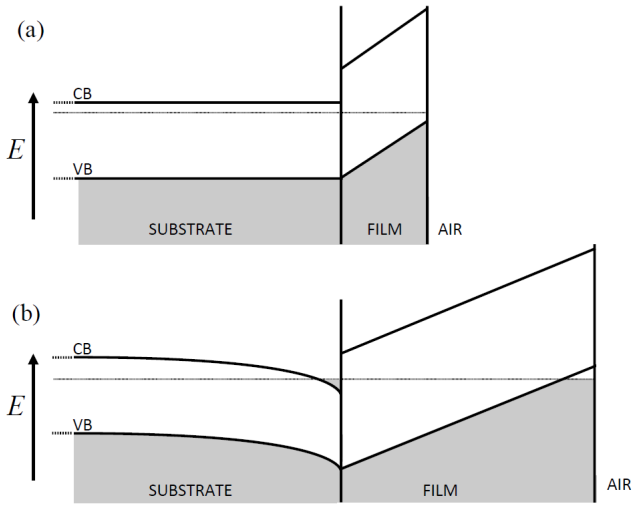

Figure 1.12: *Schematic representation of the band diagram of a polar thin film on a thick non-polar substrate (n-type interface case). a) The pristine system before the Zener breakdown. b) The electrons transfer from the surface of the film to the interface. The Fermi energy is represented by the dotted line. Figure adapted from reference [84].*

The surface redox reactions

Surface redox reactions are another possible mechanism based on the built-in electric field. The prototypical reaction

$$O^{2-} \rightarrow \frac{1}{2}O_2 + V_O + 2e^-$$

is a convenient way to create charges ($2\ e^-$) and a vacancy (V_O). Due to the electric field, the 2 electrons will be transfered to the Ti $3d$ orbitals at the interface leaving an immobile and $+2e$ charged vacancy at the LAO surface. This mechanism was originally proposed by Cen *et al.* [64] and found to be thermodynamically stable at a critical LAO thickness by Bristowe *et al.* [84]. The oxygen vacancies are not created by the growth of the film but are activated by a threshold energy coming from the electric field. This mechanism gives by this fact an explanation for the metal-insulator transition. This model takes into account the electrostatic energy associated to the electric field, a surface-interface chemistry term and a defect-defect interaction within a mean-field approximation. The parameters of the

model are fitted using density functional calculations [84, 85]. This mechanism and the electron reconstruction are in a sense in competition since they both need a large electric field to occur but both decrease the field when the electrons are transferred. An important question is then: which mechanism occurs first (see reference [12] for a discussion)?

This model allows the transfer of electrons to the interface before the usual critical thickness of 4 unit cell, thanks to several parameters. These charges are observed experimentally before 4 u.c. (see reference [39]) even if they are not mobile. Moreover it also gives a possible explanation for the trapped charges. Indeed, these vacancies at the surface are $+2e$ charged defects that create a trapping potential for the electrons at the interface. The trapping is reduced when the vacancies move away from the electrons i.e. for larger thicknesses where in addition these trapping regions are spatially larger. Moreover, the vacancies at the surface are immobile which is a possible explanation of why transport measurements are not observing holes at the $LaAlO_3$ surface [32] (except for capped system [41]).

The main features of this mechanism is in fact close to the electronic reconstruction with a pristine interface, a built-in electric field and a natural appearance of a critical thickness. However some of the features are able to explain results where the electronic reconstruction seems to fail.

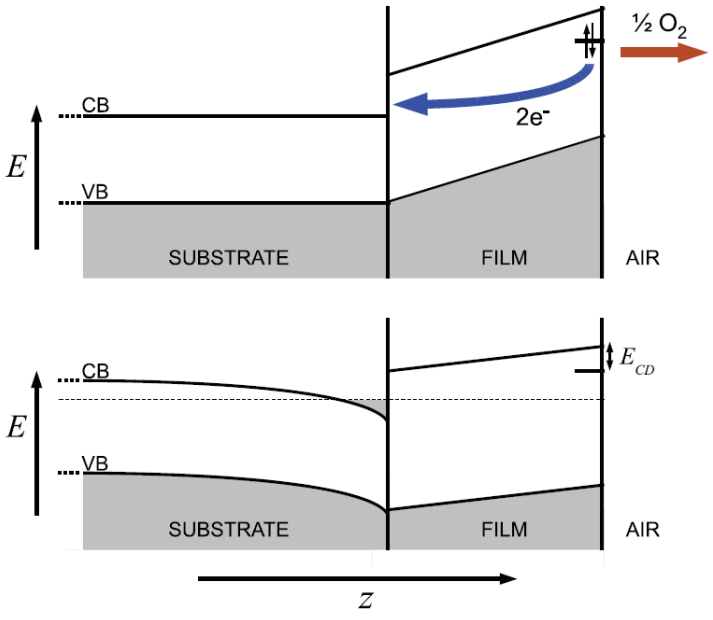

Figure 1.13: *Schematic representation of a donor state at the surface, created via a redox reaction, giving rise to an electron transfer and reducing the electric field. Picture adapted from reference [84]*

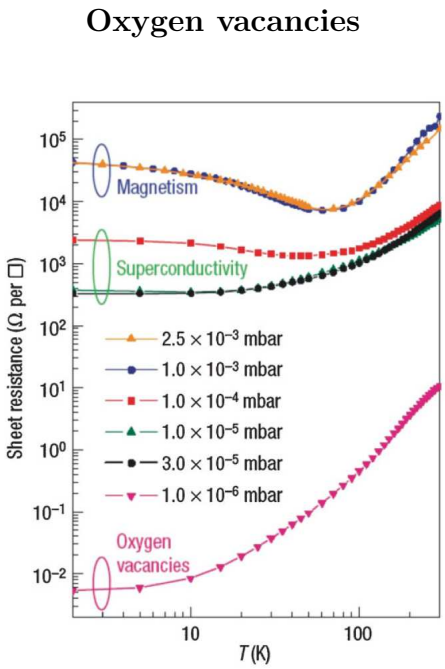

Figure 1.14: *The 3 different regimes that arise due to various partial pressure during growth. Data from reference [30] and picture from reference [86]*

Oxygen vacancies in $SrTiO_3$ are known to transform this insulator into a semiconductor with high carrier mobility [35, 37, 87] and to highly affect the $LaAlO_3$-$SrTiO_3$ system [1, 37] (see figure 1.14). For these reasons, oxygen vacancies are a possible mechanism for the formation of the 2DEG [36–38]. Nevertheless, the quality of the formal $SrTiO_3$ substrates are too high to explain the large charge densities observed in the $LaAlO_3$-$SrTiO_3$ system. But when the first layer of $LaAlO_3$ is deposited on the substrate, the species can have a high kinetic energy that ablates the STO surface, known to easily form oxygen vacancies [88]. These oxygen vacancies can also form if the oxygen partial pressure is too low (10^{-6} mbar) during the growth or the annealing step as observed in reference [37] for example. For higher oxygen partial pressure (10^{-4} mbar), or if the sample is annealed, it was shown that charge densities dropped below the intrinsic charge carrier limit of 0.5 e^-/S and that intrinsic carriers are playing the major role [30]. However, the fact that no metallic interface is observed for very high partial pressure (10^{-2} mbar) can rise some doubt on the intrinsic mechanisms. In addition the same metal-insulator transition is obtained at the $LaAlO_3$-$SrTiO_3$ (111) system, or even with amorphous LAO, which are not of the polar/non-polar type [70]. For the (111) system, it can be argued that the polar surface of STO (111) is compensated before depositing LAO, becoming by this fact, non-polar[15]. Turning the system back to the non-polar polar interface since LAO (111)

[15] Any polar substrate should undergo such a reconstruction, even before the film deposition.

is polar. It is the same reason why a STO film on a LAO substrate is not becoming conducting [89]. The LAO substrate reconstructs, becoming non-polar, and the polar discontinuity does not exist anymore. In the case of the amorphous system, annealing the samples removes the conductivity [74]. However, for a while, these two experiments were a strong argument against the polar discontinuity. Finally, the 2DEG was only observed in $SrTiO_3$ substrate systems, suggesting a strong importance of the chemistry (such as the easy formation of oxygen vacancies in $SrTiO_3$).

The main features of this mechanism is the natural appearance of oxygen vacancies in the $LaAlO_3$-$SrTiO_3$ system. The causes are multiple as the lack of oxygens in the atmosphere or the impact of high velocity atoms during the growth. In addition no electric field is needed for this mechanism and there is no need for polar discontinuity.

Cation intermixing

Cation intermixing is another mechanism proposed which can possibly explain the formation of the 2DEG through La-doped $SrTiO_3$ [60] (see figure 1.15). Indeed starting with a pristine interface and exchanging La and Sr cations can lead to a n-type doping of $SrTiO_3$ and then conductivity. In perovskites the usual inter-diffusion mechanism is between the same type of atoms i.e. A or B[16]. In our case, it is then $Al^{3+} \Leftrightarrow Ti^{4+}$ and $La^{3+} \Leftrightarrow Sr^{2+}$ inter-diffusion across the interface that occurs. The La-Sr exchange between interface and surface (across the whole film) can reduce the overall energy by canceling the potential divergence, as done by the 0.5 electron transfer. However an exchange of that type through several unit cell of $LaAlO_3$ is not necessarily kinetically possible. It is then important to consider both thermodynamic and kinetic aspects.

In fact a local (or indeed non-local) inter-diffusion across the interface ($Al^{3+} \Leftrightarrow Ti^{4+}$ or $La^{3+} \Leftrightarrow Sr^{2+}$) is not expected to dope the interface since an electron and a hole are created at each side and they will recombine. Moreover these two types of diffusion are supposed to be correlated in the sense that they have the same extent. For these reasons, a simple inter diffusion mechanism is not able to explain the doping of the interface and a full set of chemical processes are needed to clearly understand the complex mechanism at the origin of the 2DEG. A review on the instabilities and the intermixing is given in reference [10]. For instance, after a $La^{3+} \Leftrightarrow Sr^{2+}$ inter-diffusion, the hole can be trapped by a defect (Sr vacancy). Some of the La in STO are then electrically active, as explained

[16]Oxygen inter-diffusion is also allowed but does not affect the system.

in reference [10]. Finally, a La-doped $SrTiO_3$ is created which is known to be metallic.

The main features of this mechanism is a defective interface in a globally stoichiometric system that stabilize the structure compared to an abrupt interface without the need of any electric field. Some additional chemical processes also need to be involved.

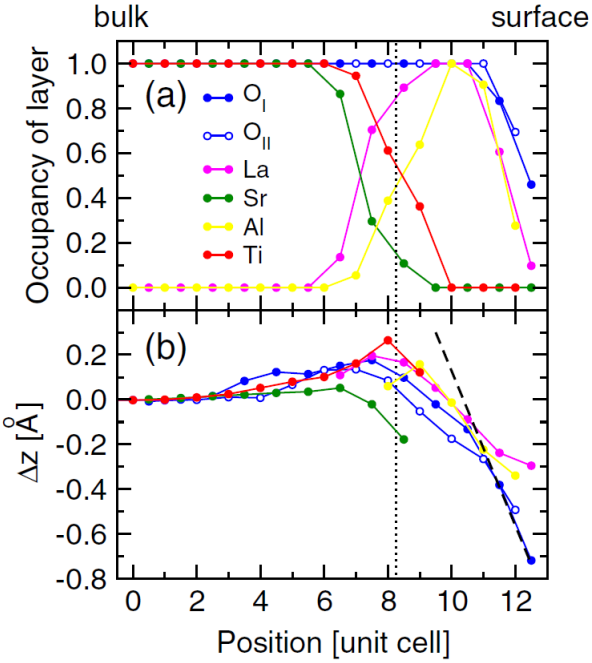

Figure 1.15: *Cations concentration per layer, showing the interdiffusion at the LAO-STO interface. Adapted from reference [60].*

1.6 Remaining puzzles

In the previous section we described different mechanisms that were introduced to explain the 2DEG at the polar/non-polar interface of $LaAlO_3$-$SrTiO_3$ system. If no consensus has emerged yet within the scientific community, it is because none of them can provide a unified explanation of all experimental data. In this section we will describe the major incompatibilities for each of these mechanisms.

1.6.1 Electric field driven mechanisms

The "toy" model that is the electronic reconstruction is not compatible with some experimental results. First of all, spectroscopic measurements [39, 42] observed a signal of doped STO ($Ti^{3.5+}$) but before the critical 4 unit cells. However the appearance of

conductivity at 4 u.c. in transport measurements [39, 42] was a strong argument in favor of the electronic reconstruction. In this model, LAO is not polar only for infinite thicknesses where a total of 0.5 e^-/S is transfered. However an experiment [90] have shown that this regime is already reached at 6 unit cells and that the carrier density is one order of magnitude lower than expected. In addition the transport measurements [1, 32] are not able to detect any signature of holes at the LAO surface which is predicted by the electronic transfer model. In addition recent soft x-ray angle-resolved resonant photoelectron spectroscopy citePhysRevLett.110.247601 sees no states crossing the Fermi level at the surface. However, experiments with capping STO layers on top of the LAO film were able to detect the existence of holes at the surface [41, 91]. This suggest that the holes may exist but might be trapped and undetectable.
We remind the reader that the redox reaction mechanisms could possibly explain these problems. For instance the vacancies created at the LAO surface are naturally immobile and the parameters allow a smaller critical thickness than 4 unit cells.

However, none of these mechanisms could explain why the value of 0.5 e^-/S is not recovered for large $LaAlO_3$ thicknesses for instance. Moreover these mechanisms are based on the polar discontinuity and do not require any external defects to occur. However the $LaAlO_3$-$SrTiO_3$ system is far from being ideal and some disorder or defects have to be added to improve the level of description of such mechanisms based on pristine compounds. The problem of these model are then their lack defects which can, for instance, add the possibility of Anderson localization or of trapped charges by acceptors created by cationic diffusion.

1.6.2 Non electric field driven mechanisms

The semiconductor community is used to associate external defects, such as cationic inter-diffusion, to the formation of an electronic gas. In addition, it is known that the $LaAlO_3$-$SrTiO_3$ interface experience inter-diffusion and that $SrTiO_3$ is very sensitive to La or vacancy doping. These effects can prevent the polar discontinuity to occur but only if they travel across the whole film. However, the case of oxides thin film heterostructures might be different from semi-conductors since a new pathway is feasible. Indeed the appearance of conductivity only after 4 u.c. is difficult to explain by these mechanisms. In addition after annealing the sample at high oxygen partial pressure, it is still conducting with a quantity of carriers that is too large to be explained by simply an oxygen vacancy

doping [28]. In addition a recent paper by Warusawithana *et al.* [92] showed that results on samples grown by molecular beam epitaxy (MBE)[17] excluded extrinsic causes such as La-doped $SrTiO_3$ or as oxygen vacancies in STO due to less aggressive growth conditions. The oxygen vacancies and the intermixing are surely present and playing a role in the $LaAlO_3$-$SrTiO_3$ heterostructure. However, it is not likely that they can, by themselves, explain all the results on the system.

1.6.3 Open issues

Within the last 10 years many different groups have grown $LaAlO_3$-$SrTiO_3$ samples with their own growth conditions. These growth methods evolved during the last 10 years as well as our understanding of the complex chemistry that arises in these systems. In addition the field has evolved rapidly and our understanding of some effects also. For that reasons a huge amount of different samples has been grown with different growth conditions and we know now that a small difference in the stoichiometry for instance can affect the mobility by two orders of magnitude or even destroy the metal-insulator transition[92]. It is known that nature always uses the easiest path, here to cancel the diverging potential, and depending on the sample (La rich, O_2 poor, ...) this path can be either electronic or cationic. First thing to do is then to ensure ourselves that the system is really in a polar discontinuity regime. If some defects occur, as La doping or oxygen vacancies, the fact that a 2DEG gas is formed due to defects is not excluding the polar discontinuity scenario. But only means that in this particular case the easiest path was that one. In addition, sometimes, a study can add some confusion for the community, as for the $LaAlO_3$-$SrTiO_3$ (111) or the LAO amorphous cases, previously discussed.

We will then split the systems into two categories, the one where the polar discontinuity exist and the ones where it doesn't. Indeed it is known that $SrTiO_3$ can be doped by La or oxygen vacancies and become a semi-conductor and in that case the question of electronic reconstruction or whatever is pointless because there is no need of it. However, what happens if such a polar discontinuity exist? What would be the consequence and properties of those systems? This is what this thesis is about. For that reason we will focus on the polar discontinuity and the consequences of the polar discontinuity.

[17] MBE allows for high quality samples due to much lower kinetic energy species during the growth.

1.7 Goals of this work

Notice that, whilst a fairly large amount of theoretical works exist in literature based on density functional theory (DFT) calculations, they are invariably carried out by local density (LDA) or generalized-gradient (GGA) approaches. It is worth emphasizing that whilst structural properties for insulating oxides are satisfactorily described in LDA and GGA, whatever concerns the LDA or GGA description of the conduction band alignment at the interface (a crucial aspect in the description of Zener breakdown, indeed) must be considered seriously faulted and not at all reliable.

For that reason, one initial motivation in this work was to reproduce the main results on the $LaAlO_3$-$SrTiO_3$ system previously obtained by local or semi local functional approximation using a more advanced approach. This will be the first fully consistent study of the $LaAlO_3$-$SrTiO_3$ system using a hybrid functional, B1-WC. This will not only reproduce the previous results on $LaAlO_3$-$SrTiO_3$ system but also improve the description of the electronic behavior known to be poorly characterized by conventional functionals. We will show that our results are in fact in qualitative agreement with the previous DFT calculations and also with the polar catastrophe scenario. These results are part of chapter 3.

The second part of this thesis is dedicated to testing the origin of the 2 dimensional electron gas within a polar discontinuity background with the help of experimentalists. Using the $LaAlO_3$-$SrTiO_3$ systems described in chapter 3 for different thicknesses we will show, in an indirect way, that the evolution of the lattice parameter in $LaAlO_3$ measured experimentally is in agreement with the prediction of the build-in electric field of the polar catastrophe. This is part of chapter 4 which is based on the results already published in reference [90]. In chapter 5 we will show that the critical thickness, t_c, can be tuned with respect to the formal charge of the compound that is deposited on the $SrTiO_3$ substrate. By choosing a solid solution of $LaAlO_3$ and $SrTiO_3$ we create an insulating material in which the formal charge of LAO is diluted by STO with respect to the ratio of the 2 materials. The evolution of t_c is observed experimentally and corresponds to the theoretical prediction of the electronic reconstruction as presented in reference [93].

Despite the fact that our results with the hybrid functional are qualitatively in agreement with conventional functionals we have access to a better description of the electronic properties of the system. We will use this advantage to describe the properties of the 2 dimensional electronic gas in the third part of this work. In chapter 6 the repartition of

the carriers in the Ti 3d orbitals is given with respect to the charge density. A threshold in the density is observed where new kind of Ti bands, having others transport properties, start to be populated. These results are based on reference [94].

This will finalize the work realized on the $LaAlO_3$-$SrTiO_3$ system where we characterized the system (chapter 3), look at the origin of the 2DEG (chapter 4 and 5) and finally studied the gas properties (chapter 6).

Chapter 2

First principles methods and theoretical background

The aim of this chapter is to give a brief description of the first-principles techniques used in this thesis. In addition, some practical details concerning theoretical calculations are given and, finally, we describe the systems that have been modeled. Additional information on density functional theory can be found for example in the review of K. Capelle [95] or the book of R. M. Martin [96].

2.1 The many body problem

To describe a macroscopic crystal, one needs in principle to obtain the quantum mechanical ground-state of the interacting electrons and nuclei by solving the time-independent Schrödinger equation:

$$H(\mathbf{R},\mathbf{r})\Psi(\mathbf{R},\mathbf{r}) = E(\mathbf{R},\mathbf{r})\Psi(\mathbf{R},\mathbf{r}), \tag{2.1.1}$$

where $H(\mathbf{r},\mathbf{R})$ is the Hamiltonian of the system, $\Psi(\mathbf{r},\mathbf{R})$ is the many-body wave function of all the particles and E is the total energy of the system. The potential energy comes from different interactions: *i)* between the electrons V_{ee}, *ii)* between the nuclei V_{NN}, *iii)* and between the electrons and the nuclei V_{eN}. In addition the electrons and the nuclei have their own kinetic energy, respectively T_e and T_N. If the set of nuclei coordinates $\{\mathbf{R}_I\}$ and of electrons coordinates $\{\mathbf{r}_i\}$ is respectively written $\mathbf{R}$ and $\mathbf{r}$ the Hamiltonian of the interacting electrons plus nuclei is:

$$H(\mathbf{R},\mathbf{r}) = T_N(\mathbf{R}) + T_e(\mathbf{r}) + V_{ee}(\mathbf{r}) + V_{NN}(\mathbf{R}) + V_{eN}(\mathbf{R},\mathbf{r}), \tag{2.1.2}$$

where we have

$$T_N(\mathbf{R}) = -\frac{\hbar^2}{2}\sum_I \frac{1}{M_I}\frac{\partial^2}{\partial \mathbf{R}_I^2} \tag{2.1.3}$$

$$T_e(\mathbf{r}) = -\frac{\hbar^2}{2}\sum_i \frac{1}{m_i}\frac{\partial^2}{\partial \mathbf{r}_i^2} \tag{2.1.4}$$

$$V_{ee}(\mathbf{r}) = \frac{e^2}{2}\sum_{I\neq J} \frac{1}{\|\mathbf{R}_I - \mathbf{R}_J\|} \tag{2.1.5}$$

$$V_{NN}(\mathbf{R}) = \frac{e^2}{2}\sum_{i\neq j} \frac{Z_I Z_J}{\|\mathbf{r}_i - \mathbf{r}_j\|} \tag{2.1.6}$$

$$V_{eN}(\mathbf{R},\mathbf{r}) = -e^2\sum_{iI} \frac{Z_I}{\|\mathbf{r}_i - \mathbf{R}_I\|}, \tag{2.1.7}$$

$$\tag{2.1.8}$$

with Z_I and M_I the charge and the mass of nucleus I and $-e$ and m_i the charge and the mass of electron i.

A common approximation is to neglect $T_N(\mathbf{R})$ due to the relation between the masses: $m_i << M_I$. This constitutes the usual approximation due to Born and Oppenheimer, allowing to separate the electronic and the nuclear degrees of freedom, $\Psi(\mathbf{r},\mathbf{R}) = \varphi(\mathbf{r})\gamma(\mathbf{R})$, given that the mass on a nuclei is much bigger than that of the electron. This is equivalent to consider that the electrons instantaneously follow the nuclei displacement. In this approximation the Born Oppenheimer Hamiltonian can be written as:

$$H_{BO}^{\mathbf{R}}(\mathbf{r}) = T_e(\mathbf{r}) + V_{ee}(\mathbf{r}) + V_{NN}(\mathbf{R}) + V_{eN}(\mathbf{R},\mathbf{r}), \tag{2.1.9}$$

where the ion coordinates are no longer a variable but a parameter.

Within this approximation only remains the kinetic energy operator of the electrons T_e, their interaction energy operator V_{ee}, the interaction energy of the nuclei V_{NN} and the potential energy operator of the interacting electrons with the nuclei V_{eN}. The advantage of the electronic Hamiltonian is that now, the electrons can be seen as interacting with an external potential that is fixed by the nuclei positions. Finally, $V_{NN}(\mathbf{R})$ can be omitted since it is now just a constant that shifts the eigenvalues.

In principle one could use the Schrödinger equation to determine the electronic wave function $\psi(\mathbf{r})$ of a system at fixed ionic positions and then calculate the total energy. Unfortunately, even in this simplified context, it is impossible to solve the equation 2.1.1 for a macroscopic solid that contains a very large number of interacting electrons. A possible way to solve this problem was proposed by P. Hohenberg, W. Kohn and L. J.

Sham. They created the basis of a new field, the density functional theory, which is the most widely used theoretical approach to date.

2.2 Density functional theory

2.2.1 Hohenberg and Kohn theorem

The seminal paper by P. Hohenberg and W. Kohn [97] set the main concept of the density functional theory. The purpose is to replace the many body wave function by the density $n(\mathbf{r})$ as a basic variable of the system. The key feature of this achievement is the one-to-one correspondence between the electronic ground state density and the external potential that fixes the Hamiltonian. If the density fixes completely the Hamiltonian it should *de facto* provide access to all the properties of the system. The authors so deduced the existence of a functional of the density $F[n(\mathbf{r})]$ for which the minimum value of the total energy density functional

$$E_{el}[n(\mathbf{r})] = \int V_{\text{ext}}(\mathbf{r}) n(\mathbf{r}) d\mathbf{r} + F[n(\mathbf{r})] \tag{2.2.1}$$

is the ground-state energy of the system, where V_{ext} is the external electrostatic potential due to the nuclei. Conversely, since it is a one-to-one correspondence, the electronic density which corresponds to the ground state minimizes the energy, under the condition that

$$\int n(\mathbf{r}) d\mathbf{r} = N, \tag{2.2.2}$$

where N is the number of electrons. This formalism allows to replace the search of the many-body wavefunction that depends simultaneously of 3N degrees of freedom by that of a density that only depends on the three spatial coordinates. However at this stage, it is simply a proof of concept that can only become useful and tractable as long as $F[n(\mathbf{r})]$ is known which is, unfortunately, not the case.

2.2.2 Kohn and Sham *ansatz*

A tractable approach to DFT was delayed until a second paper, written by W. Kohn and L. Sham [98], where they proposed a way to obtain the functional $F[n(\mathbf{r})]$ corresponding to the many-body system. It is still now the underlying idea of the first-principles

implementation in condensed matter. The concept is to map the system of interacting particles into a set of fictitious non-interacting particles moving in an effective potential such that both have the same ground state electronic density.

The many-body electronic energy corresponding to equation 2.1.9 can be written in term of the density as

$$E_{el}\left[n(\mathbf{r})\right] = \int V_{\text{ext}}(\mathbf{r})n(\mathbf{r})d\mathbf{r} + \overbrace{T_e\left[\varphi\right] + \underbrace{\frac{1}{2}\int \frac{n(\mathbf{r})n(\mathbf{r}')}{\|\mathbf{r}-\mathbf{r}'\|}d\mathbf{r}d\mathbf{r}'}_{E_H}}^{F[n(\mathbf{r})]} + E_{xc}\left[n(\mathbf{r})\right] \tag{2.2.3}$$

where the successive terms represent, respectively, the interaction between the electrons and the fixed ions corresponding to an external potential, the electronic kinetic energy, the Hartree energy $E_H\left[n(\mathbf{r})\right]$ that corresponds to the classical Coulombic interaction between electrons and finally the exchange-correlation energy $E_{xc}[n]$ that contains all the electron-electron interactions going beyond the classical Hartree term.

At this stage, the functional $F\left[n(\mathbf{r})\right]$ appears as made of three terms and $E_H\left[n(\mathbf{r})\right]$ already depends explicitly on the density. Then, within the Kohn and Sham *ansatz*, the kinetic energy of the non-interacting particles can be obtained from the single particle wave functions. In this context, $F\left[n(\mathbf{r})\right]$ can be written as:

$$\begin{aligned} F\left[n(\mathbf{r})\right] &= T_e\left[\varphi\right] + E_H\left[n(\mathbf{r})\right] + E_{xc}\left[n(\mathbf{r})\right] && (2.2.4)\\ &= T_s\left[\psi\right] + E_H\left[n(\mathbf{r})\right] + \underbrace{E_{xc} + T_e - T_s}_{E_{xc}^{\text{DFT}}[n(\mathbf{r})]} && (2.2.5) \end{aligned}$$

where, using the one-body wave function ψ_i,

$$\begin{aligned} T_s\left[n_s(\mathbf{r})\right] &= -\frac{1}{2}\sum_i \langle\psi_i|\nabla^2|\psi_i\rangle && (2.2.6)\\ n_s(\mathbf{r}) &= \sum_i \|\psi_i(\mathbf{r})\|^2 && (2.2.7) \end{aligned}$$

are respectively the kinetic energy and the electronic density of the non-interacting particles. In equation 2.2.5, a new term, $E_{xc}^{\text{DFT}}\left[n(\mathbf{r})\right] = E_{xc} + T_e - T_s$, has been introduced[1]. This term corresponds to the many-body exchange-correlation energy, supplemented by a small kinetic energy contribution coming from the fact that the kinetic energy of the non-interacting and interacting systems are not exactly the same.

[1]This transformation of the exchange-correlation energy in DFT compared to the one of the many-electron interacting system is an important aspect that will appear for the class of hybrid functionals, see later.

Initially $F[n(\mathbf{r})]$ was unknown and the DFT was not usable. At this stage and after all these transformations, E_{xc}^{DFT} is still unknown. The advantage of this reformulation is that an approximate form of E_{xc}^{DFT} is more easy to find as it will be discussed in the next section.

Kohn and Sham have shown that the many-body and one-body systems can have the same electronic ground state density making possible to pass from one system to the other one. The only condition is that the particles of the non-interacting system move in an effective potential given by:

$$v_s(\mathbf{r}) = V_{\mathrm{ext}}(\mathbf{r}) + V_H(\mathbf{r}) + V_{xc}(\mathbf{r}), \tag{2.2.8}$$

$$= V_{\mathrm{ext}}(\mathbf{r}) + \int \frac{n(\mathbf{r}')}{\|\mathbf{r}-\mathbf{r}'\|} d\mathbf{r}' + \frac{\delta E_{xc}[n]}{\delta n(\mathbf{r})} \tag{2.2.9}$$

that represents the contribution of all the ions and all the other electrons. It assumes that such a system of non-interacting particles exists. Moreover, the exchange and correlation terms are still unknown and need to be approximated, as it will be further discussed in the next section.

In summary, the real many-body interacting electron problem can be mapped into a non-interacting particle system that move in an effective potential, both having the same exact ground state electronic density. One of the practical methods to obtain this density is to use the one-body wave functions ψ_i with the usual Schrödinger equation, the normalizing condition $\langle\psi_i|\psi_j\rangle = \delta_{ij}$ and the following set of equations :

$$\begin{cases} \left[-\frac{1}{2}\nabla^2 + v_s\right]|\psi_i\rangle = \epsilon_i|\psi_i\rangle \\ v_s[\mathbf{r}] = V_{\mathrm{ext}}(\mathbf{r}) + \int \frac{n(\mathbf{r}')}{\|\mathbf{r}-\mathbf{r}'\|} d\mathbf{r}' + \frac{\delta E_{xc}[n]}{\delta n(\mathbf{r})} \\ n_s(\mathbf{r}) = \sum_i \|\psi_i(\mathbf{r})\|^2 \end{cases} \tag{2.2.10}$$

The ground state total energy $E_{el}[n(\mathbf{r})]$ (equation 2.2.1) is not equal to the sum of the independent eigenenergies ϵ_i that overcounts the electron-electron interaction. However the density $n_s(\mathbf{r})$ is supposed to be equal to the one of the real system and can be used in equation 2.2.3 to finally deduce the ground state total energy $E_{el}[n(\mathbf{r})]$.

The equations 2.2.10 are used by the simulation program CRYSTAL [99] that solves the Schrödinger equations i.e. that diagonalizes a matrix. Another method, used in the simulation package ABINIT [100], is to obtain the ground state density by minimizing the equation 2.2.10b. Here, we explain the method used by CRYSTAL since it is the

simulation package we used for this work. At this stage the original many-body problem is greatly simplified but the equations 2.2.10 are highly nonlinear and need to be solved self consistently. As a starting point, a guess electronic density $n_{i-1}(\mathbf{r})$ for a fixed set of atomic positions $\mathbf{R}$ is used to generate the effective potential $v_s[\mathbf{r}]$. The Schrödinger equations are solved giving the ground state wave functions $|\psi_i\rangle$, which are used to generate the new density $n_i(\mathbf{r})$. At that point, a self-consistent criterion is considered:

$$|n_{i-1}(\mathbf{r}) - n_i(\mathbf{r})| \leq \epsilon, \tag{2.2.11}$$

where ϵ is the threshold to stop the self-consistent cycle. If the criterion is not satisfied, a new density n_{i+1} is generated via the mixing of the two previous ones n_i and n_{i-1} and the self-consistent cycle continues. When the criterion is finally satisfied, it means that the density $n_i(\mathbf{r})$ corresponds to the density of the fully interacting many-body system. $n_i(\mathbf{r})$ can be used in the real system, fixing by this fact $V_{\text{ext}}(\mathbf{r})$ and the Hamiltonian.

This procedure can be schematically represented as followed:

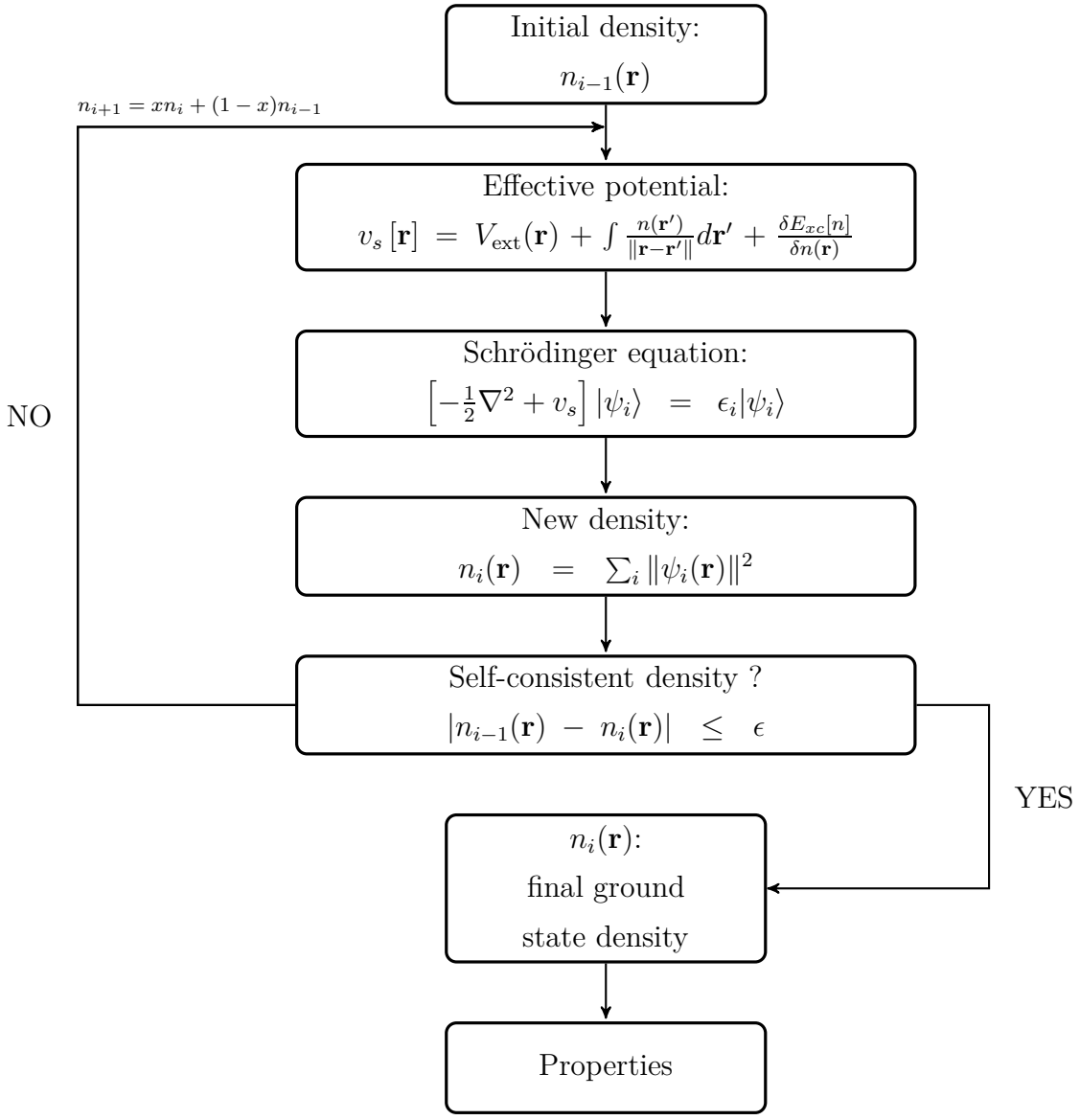

2.3 Practical implementation of DFT

In the previous section we have shown that the Hohenberg and Kohn theorem combined with the Kohn and Sham *ansatz* give rise to a theory based on the density, able to describe a quantum many-body system. However, even if mathematically exact, this theory does not provide the exchange and correlation energy that needs to be approximated.
Here, we introduce some approximations that are used in the density functional theory. These are of two types. Firstly, a choice has to be made to approximate the exchange and correlation terms. This choice can affect the ability of a simulation to properly describe a system. This is the biggest approximation that is done in DFT and changing from

one to another choice does not necessarily improve the results. Secondly, computational approximations are also needed to make the calculations tractable, as usually done by coarse graining, and are linked to time consideration. For example, an infinite sum needs to be truncated and it is always possible to increase the precision by adding more terms to the sum. In this case, adding these terms will always lead to a more precise result, increasing however, the computational time and the resources needed. For that reason, convergence calculations are mandatory to obtain a good precision of the material properties in a reasonable computational time. This section is a general approach; the choice of the basis sets, pseudopotentials and other technical details are given in the next section.

2.3.1 Exchange and correlation functional

In the Kohn and Sham formalism, the only reason why the theory is not exact is due to the exchange and correlation term. In any DFT calculations, a choice has to be made to approximate these interactions. In this section, we describe the different possible approximations.

Local and semi-local approximations

The first and still widely used approximation that was proposed to describe the DFT exchange-correlation term is the Local Density Approximation (LDA) [98]. In this functional, the exchange and correlation energy per particle ϵ_{xc}(r) at point r is assumed to i) only depend on the density at that point and ii) be the one of a homogeneous electron gas with the same density:

$$E_{xc}^{\mathrm{LDA}}[n] = \int \epsilon_{xc}^{\mathrm{hom}}([n], \mathbf{r}) n(\mathbf{r}) d\mathbf{r}. \tag{2.3.1}$$

The analytic form of the exchange energy of a homogeneous electron gas is known exactly,

$$\epsilon_{x}^{\mathrm{hom}}[n] = -\frac{3}{4\pi}\left(3\pi^2 n\right)^{1/3}, \tag{2.3.2}$$

while the correlation part can be calculated from quantum Monte Carlo simulations [101] once for ever and used in all calculations. This approximation, despite being crude, is widely used since it gives a (surprisingly) good agreement with the structural and dynamical experimental data, with the advantage of its simplicity. However, it is commonly accepted that the bond lengths are typically too small and cohesive energy not very well

described. Also, the band gap energy is almost always, and usually highly, underestimated by this functional.

An obvious extension to the LDA approximation, which however does not necessarily improve it, is to include the additional information contained in the variation of the density. A first attempt was to include terms as $|\nabla n(\mathbf{r})|$ or $|\nabla^2 n(\mathbf{r})|$ *etc.*, to the LDA approximation giving rise to what is called semilocal (quasilocal) approximation. However, the effect was not an improvement but was usually worse than the local functional. Finally, a breakthrough was reached when one realized that a more general function of the density and the gradients and higher order derivatives was a better choice than a power series expansion, leading to the concept of generalized-gradient approximation (GGA) [102],

$$E_{xc}^{\mathrm{GGA}} = \int f\left(n\left(\mathbf{r}\right), \nabla n(\mathbf{r})\right) d\mathbf{r}. \tag{2.3.3}$$

In the LDA approximation the number of different functionals (Perdew-Zunger, Teter ...) are linked to various fit of Monte Carlo data for the correlation term. However the GGA functionals [102] are much more different due to various fitting parameters and various constraining conditions. For a long time, the most popular functional was the Perdew, Burke and Ernzerhof (GGA-PBE) [103] approximation later improved to increase the description of solids and surfaces [104]. It was Wu and Cohen that pointed out the incapacity of the PBE functional to properly describe solid and surface aspects, resulting to their own functional (GGA-WC) [105]. The PBE-sol just applies this improvement to the PBE functional.

Hybrid functionals

A shortcoming of the DFT is that some parts of the exchange and correlation energy are not the one of a fully interacting system but are a specific average of non, partially and fully interacting systems[2]. This problem gives rise to the concept of hybrid functional that try to reobtain the exact exchange energy as in the Hartree-Fock theory. The hybrid functional is a mix of usual LDA or GGA approximations with an exact exchange from the Hartree-Fock theory. A formal justification of this mix can be provided through the adiabatic connection formula [106, 107] that continuously link the non-interacting system of KS ($\lambda = 0$) to the fully interacting system ($\lambda = 1$) where λ characterize the electron-electron interactions (the interaction strength is λe^2).

[2]As discussed in the previous section, a part of the kinetic energy is transferred in the exchange and correlation DFT term: $E_{xc}^{\mathrm{DFT}} = E_{xc}^{\mathrm{MB}} + T_e^{\mathrm{MB}} - T_{KS}$.

It was A. Becke who for the first time used and showed the improvement brought by such functionals [108] that includes one or more parameters. Since that time many hybrid functionals have been developed, B3LYP [109, 110], HSE [111] etc, that differs by the number of parameters and the source of the exchange and correlation corrections (*ab initio* or empirical). As an example, the B3LYP[3] approximation is given by:

$$\begin{aligned} E_{xc}^{\mathrm{B3LYP}} = E_x^{\mathrm{LDA}} + & \quad a_0 \left(E_x^{\mathrm{HF}} - E_x^{\mathrm{LDA}} \right) \\ + & \quad (1-a_0) a_x \left(E_x^{\mathrm{GGA}} - E_x^{\mathrm{LDA}} \right) + E_c^{\mathrm{LDA}} \\ + & \quad a_c \left(E_c^{\mathrm{GGA}} - E_c^{\mathrm{LDA}} \right) , \end{aligned} \tag{2.3.4}$$

where $a_0 = 0.20$, $a_x = 0.9$ and $a_c = 0.81$; E_x^{GGA} and E_c^{GGA} are respectively the exchange terms of Becke [112] and the correlation of Lee, Yang and Parr [113]. In addition, many alternative functional can be defined by tuning the parameters to fit with the experimental data[4].

Although very popular and widely used, B3LYP was shown to be inappropriate for perovskite compounds like $BaTiO_3$ or $PbTiO_3$, providing a fake super tetragonal ground-state comparable to that obtained in GGA-PBE. The problem was traced back in the Becke's GGA exchange part [114]. In order to bypass that problem a new hybrid functional was introduced for ABO_3 compounds. It relies on a much simple B1 approach, involving only one parameter and the Wu and Cohen GGA that was shown to reproduce nicely the structural properties of perovskites. The so-called B1-WC functional is defined as:

$$E_{xc}^{\mathrm{B1-WC}} = E_{xc}^{\mathrm{GGA-WC}} + a_0 (E_x^{\mathrm{HF}} - E_x^{\mathrm{GGA-WC}}), \tag{2.3.5}$$

with $a_0 = 0.16$ (it corresponds to equation 2.3.4 with a_c and a_x fixed to 1 and the resulting simplifications). The a_0 parameter was fixed by Bilc *et al.* in order to best fit the electronic and structural properties of $BaTiO_3$. It was then shown that the so-defined B1-WC functional reasonably reproduce the electronic and structural properties of various perovskite oxides, including magnetic systems and multiferroïcs [115–117]. Its main advantage over typical LDA or GGA approaches is that it provides more correct bandgaps while retaining the accuracy of the GGA-WC functional at the level of the structural properties. A recent review by Franchini [118] is dedicated to hybrid functionals applied to perovskites.

[3] B for Becke approximation, 3 for the number of parameters and LYP for the approximation of Lee, Yang and Parr

[4] It is actually not the case for the B3LYP functional.

2.3.2 Periodic boundary conditions

When modeling periodic crystals, it is often convenient to use Born-von Karman periodic boundary conditions. It allows to i) represent the system with a basic unit cell[5] that is infinitely and periodically repeated in the three spatial directions and to ii) represent the wave functions of the system with a particular form: the Bloch functions. The Bloch's theorem, that requires a periodic potential, shows that the wave function can be written as the product of a plane wave and a function $u_{n\mathbf{k}}(\mathbf{r})$ that has the crystal periodicity, giving

$$\psi_{n\mathbf{k}}(\mathbf{r}) = e^{i\mathbf{k}.\mathbf{r}} u_{n\mathbf{k}}(\mathbf{r}), \tag{2.3.6}$$

where $\mathbf{k}$ is a vector of the reciprocal space and n is the band index. In this reciprocal space, also called the $\mathbf{k}$-space, several vectors $\mathbf{k}$ correspond to the same $\psi_{n\mathbf{k}}(\mathbf{r})$ and usually, the $\mathbf{k}$-space is restricted to non equivalent vectors, referred as the first Brillouin zone.

In the limit of an infinite solid, the sum over a fixed number of k-points is transformed into an integral over an infinite number of k-points. In practical DFT calculations, the number of k-point used to represent the wave function is truncated and convergence calculations are needed to include enough k-points to reach a sufficient precision within a reasonable computation time. This is called the $\mathbf{k}$-point sampling and it is always possible to increase the level of accuracy of a calculation by increasing this sampling.

These periodic boundary conditions are very convenient to represent bulk materials or superlattices but are less appropriate for isolated thin films or systems containing defects. For this reason, we briefly describe some particular approaches used in DFT, such as the primitive cell or the supercell. In this way, we hope to help the reader not used to DFT calculations to understand why, in DFT, some systems are easily modeled and why some others are not.

Point defects

The restrictions due to the repetition of a building block to represent the system are shown with a particular simple example. The system in figure 2.1a is composed of A and B atoms and can be reproduced with the unit cell shown in dashed line[6]. In this case,

[5] This one is called primitive cell if it is the smallest cell that reproduces the crystal.

[6] The choice of the unit cell is not unique and the smallest unit cell that can reproduce the solid is generally called the primitive unit cell.

the description of the crystal is realized through the primitive unit cell that contains only 2 atoms. Nevertheless, to model the same system but with one over 4 B atoms missing, figure 2.1b, it not possible to use the same primitive unit cell. Indeed, by removing the atom B of this cell, all the atoms B of the system are removed. A possible solution is to take a bigger unit cell of at least 8 atoms, 4 A plus 4 B, and to remove one B atom in that bigger unit cell. However, the system contains additional atoms (8 instead of 2). It is then more time consuming, or even impossible, to model a system that contains defects[7]. More importantly, this unit cell represents only a specific way to model a 25% defect system. It does not necessarily correspond to the conformation of the sample where defects can be agglomerate, homogeneous *etc.*

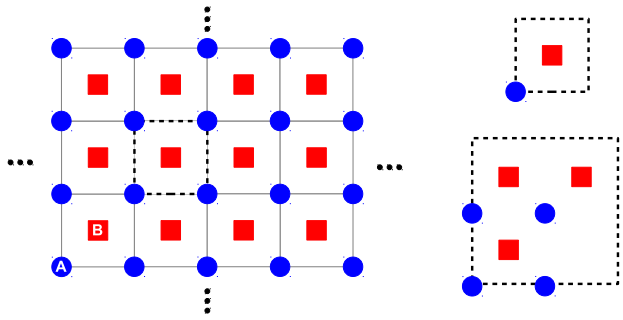

Figure 2.1: *A system composed of A and B atoms with the corresponding unit cell at top right. Down right is shown the unit cell to obtain 1 over 4 B atom defect*

Supercell approach

In viewpoint of periodic system, the interface or surface can be considered as a two-dimensional defect. Some tricks are required to overcome the limitations due to the periodicity imposed in the DFT calculations. As example, the figure 2.2 represents a system composed of 3 layers of A atoms with 2 layers of B atoms on top. The use of a particular cell, that already contains the complete system, allows to reconstruct it. This approach is called the supercell. In our example, by choosing a supercell composed of 3 A atoms and 2 B atoms, as represented in figure 2.2, the periodic boundary conditions lead to a repeated series of 3 A atom layers and 2 B atom layers stacks. However, due to the periodicity, not only a A-B interface is created but also an additional B-A interface. If this interface in not desired, it is possible to add some vacuum at the end of the supercell, creating isolated system, as represented in figure 2.2. The vacuum has to be large enough

[7]In addition it can also break symmetries further increasing the complexity and calculation time.

to avoid any interactions (electrostatic which is long range) between the repeated cells. In many DFT programs making use of a plane-wave basis set, an increase of the vacuum thickness leads to an increase of the computational cost due to the complexity to represent the vanishing of the electronic density in the vacuum. This problem is avoided when making use of local basis functions like in CRYSTAL or SIESTA [119]. In this case, very large vacuum regions can be included at no cost and isolated slabs can be properly modeled (in practice periodic boundary conditions are preserved but vacuum regions of 500 Å or more are included).

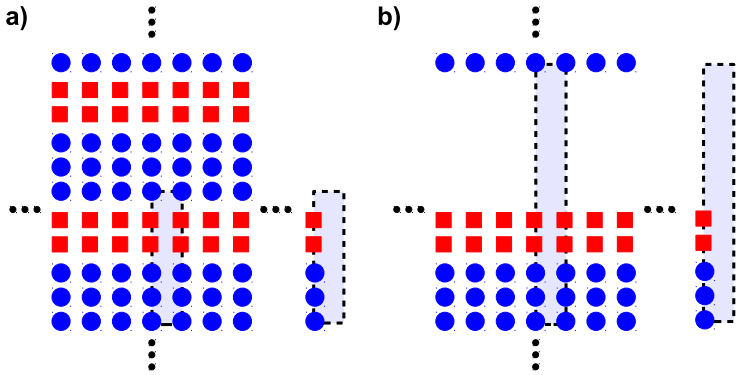

Figure 2.2: *Representation of a system with a supercell approach. a) The system, with two interfaces due to the periodicity, and its supercell. b) The same system, but with only one interface thanks to the addition of vacuum, and its supercell.*

2.3.3 Basis set

We have shown that in an infinite and periodic solid with Born-von Karman periodic boundary conditions, the wave functions can be written in terms of Bloch functions (equation 2.3.6). Various mathematical representations, also called basis sets, are possible. Due to the form of the Bloch function, it is very convenient to use a plane wave basis set: $\psi_{n\mathbf{k}}(\mathbf{r}) = Ce^{i(\mathbf{k}+\mathbf{G}).\mathbf{r}}$ where $\mathbf{G}$ is a vector of the reciprocal space. Practically, the number of plane waves is limited by a cutoff energy which requires convergence calculations to be determined. Again, an increase of the cutoff energy always leads to more accurate calculations. The difficulty to reproduce highly localized orbitals with plane waves basis set leads to the concept of a pseudopotential, see later.

Another approach, usually more common in chemistry, is the linear combination of atomic

orbitals (LCAO). Then the atomic orbitals can be described by Gaussian orbitals[8]. Unfortunately, a single Gaussian is not able to describe the electronic wave function near the nucleus and so they are usually contracted as follow:

$$\chi\left(r,\theta,\phi\right)=\left(\sum_{j}C_{j}e^{-\alpha_{j}r^{2}}\right)\left[r^{l}Y_{lm}(\theta,\phi)\right], \tag{2.3.7}$$

where $Y_{lm}(\theta,\phi)$ are spherical harmonics and the C_j is the contraction coefficient with a α_j exponents. The atomic orbitals of each atom are then a linear combination of Gaussian basis functions. In this case, it is not a cutoff energy that is needed but the number of contractions that is used to describe a specific orbital. With Gaussian it is more convenient to reproduce the tightly bound core orbitals allowing to describe both valence and core electrons, called all electrons basis. However, pseudopotentials are usually used for heavy atomic elements.

2.3.4 Pseudopotentials

The rapid variation of the wave function around the nuclei of core electrons is not easily described with a limited basis set. In addition these core electrons are subject to relativistic effects and the internal electrons close to the nucleus are subject to a diverging Coulomb potential. For these reasons, it is not easy and it is time consuming to describe heavy elements through a limited basis set. Thankfully, some simplifications can be realized thanks to different considerations.

Firstly, the core electrons are only slightly affected by the crystal formation and only the valence electrons form the chemical bonds. In addition the properties of solids are mainly linked to valence electrons. It is then reasonable to approximate the core electrons wave functions by the one of the isolated atom. This is the frozen-core approximation.
Secondly, the properties of the crystal are not really sensitive to the valence electrons wave functions in the core region due to the large screening by the core electrons in that region. It is then legitimate to transform the diverging potential yielding fast oscillating wave functions in the core region to a smooth pseudo-potential. This is equivalent to consider that the core electrons are gathered with the nucleus to form a rigid ion and that the valence electrons are interacting through an effective potential with that ion.

[8] Another common choice is to use numerical atomic orbitals as it is done in the simulation package SIESTA [119].

This is the pseudopotential approximation [120, 121]. Within this approximation the previous problems of the basis set are avoided and the calculations are faster.

2.4 DFT study of the LAO/STO interface

In this section, we describe the different choices of approximations that we used for this work, such as the exchange and correlation functional, the pseudopotentials or the convergence criteria. In addition, we describe the different kind of systems that we modeled for this work.

2.4.1 Technical details

Exchange and correlation functional

If standard local (LDA) and generalized-gradient (GGA) approximations are reasonably accurate in the description of structural properties of wide bandgap insulators, they both fail to correctly treat strongly correlated and localized systems (3D systems, surface/interface, ...). Moreover, because of the typical bandgap problem they usually fail to reproduce the correct band alignment at interfaces.

LDA+U or GGA+U are giving better results concerning the electronic properties but the value of U is unknown and it is not transferable between different systems or different simulation programs. In addition, the improvement on the electronic structure thanks to a better electron localization has a cost. For instance, it is know that LDA+U can have a large impact on phonon frequencies and on the polarity of the modes, affecting the dielectric constant for instance. In fact, depending on the U value, the dielectric constant of $SrTiO_3$ can decrease from $\sim$ 300 to $\sim$ 30 while this parameter has a large impact on the $LaAlO_3$-$SrTiO_3$ properties, especially the screening and the localization of the gas in STO.

For the systems described in this work these shortcomings have a major importance and an appropriate beyond-local density functional method should be exploited. For these reasons, in this work the so called B1-WC hybrid functional [114] will be used.

Basis set and pseudopotential

The Gaussian basis set has the advantage that it is localized functions, decreasing computation time comparing to plane wave basis set which are extended in space. This kind of localized basis is an advantage when modeling finite system such as two-dimensional slab [119]. Indeed, in a slab, the electronic density brutally vanish at the surface and localized Gaussians easily reproduce that behavior, unlike plane waves. In addition the interactions of the $3d$ electrons are more easily represented with atomic orbitals than plane waves[9]. Finally the exact exchange energy, which is used in B1-WC, is easily expressed in term of Gaussians.

All the electrons have been included in Ti [122], O [123] and Al [124], while we use a Hartree-Fock pseudopotential [123] for Sr and the Stuttgart energy-consistent pseudopotential [125] for La. The basis sets of Sr and O were specifically optimized for $SrTiO_3$. In the basis set of La, the Gaussian exponents smaller than 0.1 were disregarded and the remaining outermost polarization exponents for the 10s, 11s shells (0.5672, 0.2488), 9p, 10p shells (0.5279, 0.1967), and 5d, 6d, 7d shells (2.0107, 0.9641, 0.3223), together with Al 4sp (0.1752) exponent from the 8-31G Al basis set, were optimized for $LaAlO_3$.

Reciprocal space

The Brillouin zone integrations were performed using a 6×6×1 mesh of k points, and the self-consistent calculations were converged up to an energy threshold of 10^{-8} Hartree. An extra-large predefined pruned grid consisting of 75 radial points and 974 angular points was used for the numerical integration of charge density. After relaxation, new wavefunctions are obtained using an energy threshold of 10^{-9} Hartree and a 12×12×1 mesh of k-points. In addition, we used a gilat mesh that is always doubled compare to the latter mesh giving us a better description of the Fermi energy and the density matrix. All properties are obtained using a new k-mesh of 24×24×1 and doubled gilat mesh.

Convergence criteria

The structural optimizations were performed until reaching together thresholds of 3 10^{-5} Hartree/Bohr on the root-mean square values of forces and of 1.2 10^{-4} Bohr on the root-mean square values of atomic displacements. The level of accuracy in evaluating the

[9]The d orbitals are strongly localized compare to other orbitals

Coulomb and exchange series is controlled by five parameters [99]: the values used in our calculations are 7, 7, 7, 7, and 14.

Simulation package

The B1-WC calculations have been performed using the linear combination of atomic orbitals (LCAO) as implemented in the CRYSTAL code [99], which adopts Gaussian-type basis sets including polarization orbitals. Additionally, the CRYSTAL [99] simulation program allows a very large vacuum thickness (500 Å) without any additional time cost. In a fictitious way, this cancels the periodic boundary conditions without any dipole correction. This program is then well suited for the modelisation of a $LaAlO_3$ thin film on top of a (001) $SrTiO_3$ substrate.

2.4.2 Modeled systems

Generalities

In this work, we always referred to the $LaAlO_3$-$SrTiO_3$ system in a general way. However, different kind of systems can be modeled that differ by the choice of some degrees of freedom. In addition, this work has different concerns as the possible origins of the 2DEG or its properties. To reach these goals, some specific $LaAlO_3$-$SrTiO_3$ systems had to be modeled but by taking into account the specific ways a system is modeled in DFT.

In this work, only the (001) oriented STO substrate is considered. In that specific orientation, $LaAlO_3$ is formed of charged planes, $(LaO)^+$ and $(AlO_2)^-$ and $SrTiO_3$ of neutral planes, $(SrO)^0$ and $(TiO_2)^0$. For all cases, a few layers of $LaAlO_3$ are deposited on a thick $SrTiO_3$ substrate which clearly imposes a planar tensile strain on LAO and a resulting c axes contraction, as discussed in the previous section.

The systems modeled in this work are based in the following degrees of freedom:

$\rightsquigarrow$ First of all, theoretically, it is possible to model a 2 dimensional slabs or a 3 dimensional superlattice. The latter is a repetition of a supercell which is a cell containing a certain number of layers, without any vacuum. Slabs are composed of $LaAlO_3$ and $SrTiO_3$ layers but surrounded by vacuum. This one has to be big enough to avoid the interaction between two repeated systems which cannot be avoid due to the three directional boundary condition imposed by the DFT.

$\rightsquigarrow$ An other degree of freedom is the layers in contact that create the interface. We have 2 types of layers for $LaAlO_3$ that can form an interface with 2 types of $SrTiO_3$ layers, leading to 4 different kinds of interfaces: $(LaO)^+/(TiO_2)^0$, $(SrO)^0/(AlO_2)^-$, $(LaO)^+/(SrO)^0$ and $(TiO_2)^0/(AlO_2)^-$. The 2 last interfaces are not energetically favorable and the 2 first are called respectively n-type and p-type interfaces.
$\rightsquigarrow$ The surface termination of the 2 dimensional slabs is also important. In this work, the stoichiometry is fixed which involves that the surface termination is fixed by the kind of interface. For the n-type interface, the surfaces are SrO on one side and AlO_2 on the other side.
$\rightsquigarrow$ The number of $LaAlO_3$ and $SrTiO_3$ layers is also a parameter since it can directly affect the properties of the 2 DEG.
$\rightsquigarrow$ Finally, a choice of a pristine or defect system can be made. At first the systems are completely ideal (interface, surface, no vacancies) but additional systems with intermixing and alloys are also used in this work.

Studied systems

The first choice is between a slab or a superlattice. In this work both are modeled and they are respectively written as vacuum/$(STO)_m$/$(LAO)_n$/vacuum and $(STO)_m/(LAO)_n$ where m and n represent the number of cells[10] of $LaAlO_3$ or $SrTiO_3$. These systems, represented in figure 2.3, are in fact very different and will be presented in more details.

$\rightsquigarrow$ *superlattice:* The simplest LAO/STO heterostructure that can be modeled is the one we call "fully compensated": $(LAO)_m/(STO)_n$. This structure contains 2 ideal n-type (p-type) interfaces TiO_2/LaO (SrO/AlO_2) with in-plane lattice parameters fixed to the STO bulk value. Due to a symmetry center, each layer has its own mirror layer except for the additional TiO_2 and LaO layers for n-type. For this reason the system is non-stoichiometric and the additional plane in LAO brings a +1 charge in the system that is evenly shared by the 2 interfaces. These 0.5 extra electrons dope the 2 interfaces and this is exactly the value needed to fully compensate the field in LAO. In the polar catastrophe scheme it corresponds to a system with a large number of LAO cells. 3 superlattices with two n-type interfaces are modeled, differing by the number of LAO and STO cells: 4.5, 6.5 and 8.5. A fourth supercell, with n = 6.5 and a p-type interface is also modeled. No atomic mixing, oxygen vacancies or oxygen rotations are present in these structures.

[10] In superlattice, m and n are half-integer since an additional LaO and TiO_2 layer is imposed.

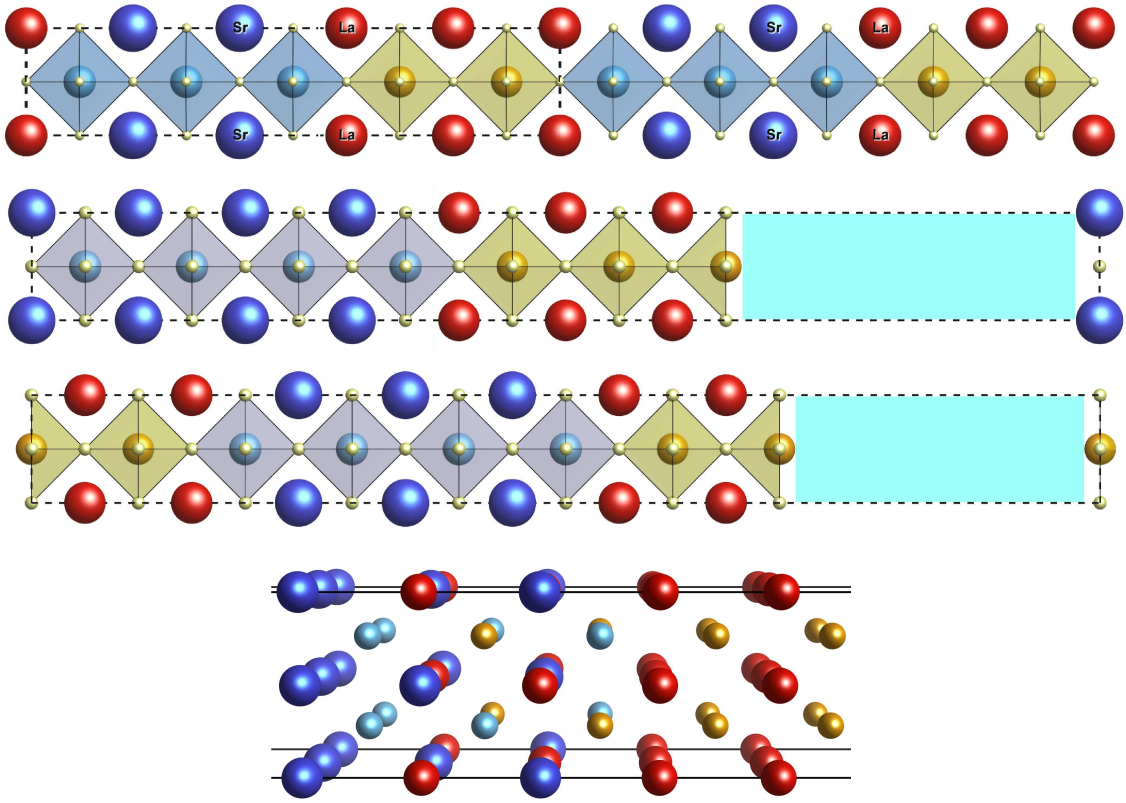

Figure 2.3: *top: $(SrTiO_3)_{2.5}/(LaAlO_3)_{2.5}$ n-type superlattice with the supercell in dashed line. middle top: $(SrTiO_3)_4/(LaAlO_3)_3$/vacuum slab with a n-type interface. middle bottom: $(LaAlO_3)_2/(SrTiO_3)_{3.5}/(LaAlO_3)_2$/vacuum symmetric slab with two n-type interfaces. bottom: the interface region of a $LaAlO_3$-$SrTiO_3$ system with intermixing.*

$\rightsquigarrow$ *slab:* Isolated vacuum/$(STO)_7$/$(LAO)_n$/vacuum stacks with n ranging from 2 to 12 were also modeled. $SrTiO_3$ contains 7 unit cells to have a good description of both the electronic and the structural behavior within a reasonable time cost. A full atomic relaxation is performed, imposing the in-plane lattice constant to the STO bulk value (3.88 Å). The 5 atoms at $SrTiO_3$ surface are fixed to the cubic STO to simulate the effect of a thick substrate. In practice, CRYSTAL makes use of periodic boundary conditions and allows isolated finite systems to be modeled using a large supercell of 500 Å in the direction along which the system is not periodic.

In addition to check the validity of this 2D approach, we also considered symmetric vacuum/$(LAO)_n$/$(STO)_{14}$/$(LAO)_n$/vacuum stacks. In this case, the system is identical to the "single" one except that the STO surface is removed. In both cases (single and symmetric), the atomic structure and the c/a ratio are similar and single systems will

usually be used due to time consideration[11].

$\rightsquigarrow$ *intermixed system:* In addition, to study the extrinsic effects mentioned in chapter 1, we model different systems that include some intermixing. In these ones, the ideal interface is replaced by an exchange between La and Sr atoms or Al and Ti atoms. The mixing is restricted[12] to the first layers of the interface even if experimentally the extent is slightly different[13] [60]. The stoichiometry is kept fixed and 50% of the interfacial atoms are mixed i.e. the cell is doubled in the a and b directions.Slabs and superlattices are modeled with this particular intermixing leading respectively to vacuum/$(STO)_4$/$(LAO)_n$/vacuum systems and $(LAO)_m$/$(STO)_n$/$(LAO)_m$.

$\rightsquigarrow$ *solid solution system:* Finally, $LaAlO_3$ can be replaced by a solid solution of $LaAlO_3$ and $SrTiO_3$ in slabs or superlattices. These cases are more complex and are explicitly described in the chapter 5.

[11]Because of the STO surface, some energy states can appear at lower energies in the band structure, called surface states. By fixing the 5 atoms at the STO surface, we artificially (almost) cancel this problem that will not be further discussed in this work.

[12]As previously discussed, adding some defects always complicate the calculations due to the boundary conditions.

[13]The mixing is in larger range for La/Sr compare to Al/Ti exchange.

Chapter 3

$LaAlO_3/SrTiO_3$ interface

In this chapter, we give a more complete description of the electronic reconstruction model, one of the mechanisms which possibly leads to the creation of the 2DEG. We also describe, starting from the bulk compounds, the results of our first-principles calculations with the B1-WC functional on the $LaAlO_3$-$SrTiO_3$ systems and the important features related to the 2DEG. By this way, we will show that first-principles calculations with the B1-WC functional are well suited to describe the appearance of the 2DEG at the pristine $LaAlO_3$-$SrTiO_3$ interface.

3.1 Bulk properties of LAO and STO

The original compounds used by Ohtomo and Hwang [1] are the two insulators $LaAlO_3$ (LAO) and $SrTiO_3$ (STO). Although many different materials are now used to investigate the appearance of a 2DEG at interfaces, such as $SrTiO_3$ and $LaTiO_3$ [81], $LaGaO_3$ [82] or $LaVO_3$ [83], in this work we will focus on LAO and STO. The latter is an undistorted cubic perovskite at room temperature with a lattice parameter of 3.905 Å and $LaAlO_3$ adopts a rhombohedral structure that can be approximated by a pseudo-cubic structure with a lattice parameter of 3.791 Å. Both materials are band insulators with an experimental band gap of 3.2 eV and 5.6 eV respectively. In the (001) direction, $LaAlO_3$ is composed of charged planes $(LaO)^+$ and $(AlO_2)^-$ and $SrTiO_3$ of neutral planes $(SrO)^0$ and $(TiO_2)^0$ as represented in figure 3.1. In this section we will describe these two bulk materials using the hybrid B1-WC functional.

A very important aspect of our employed approach is the accurate description of the constituent bulk materials. In order to appreciate the relevance of B1-WC method for

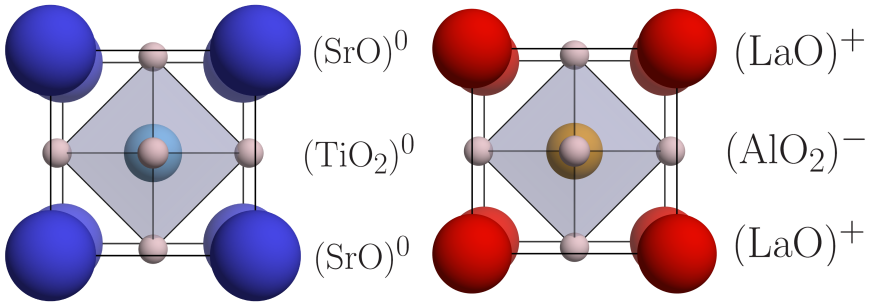

Figure 3.1: *Bulk $SrTiO_3$ and $LaAlO_3$ in cubic phase. The planes are charged corresponding to oxidation numbers as follow: $(La^{3+}O^{2-})^+$, $(Al^{3+}O_2^{2-})^-$, $(Sr^{2+}O^{2-})^0$ and $(Ti^{4+}O_2^{2-})^0$.*

the correct rendition of STO and LAO, in the following we compare the results not only with the experiment, but also with values obtained with reference local and semi-local functionals (LDA and GGA, respectively), typically used in most *ab initio* studies of $LaAlO_3$-$SrTiO_3$. We will also add results with the VPSIC functional since a collaboration with Dr Alessio Filippetti at the university of Cagliari was realized as further discussed in chapter 6.

Relaxed atomic structure

The optimized structural parameters are reported in Table 3.1, in comparison with the experiment [126, 127], for cubic STO and LAO. For both materials, our calculations predict lattice parameters within an error bar of 1% (lower for B1-WC and LDA, higher for VPSIC) compare to the experimental value. A LAO tetragonal distortion following the lock of in-plane lattice constant to the theoretical STO value, 3.88 Å, is also reported in the table, since relevant to the epitaxial STO/LAO heterostructure. Clearly, this imposes a planar tensile strain on LAO and a resulting c axis contraction. The B1-WC functional yields $c_0 = 3.75$ Å (thus c/a = 0.97), corresponding to a Poisson ratio of 0.24, in perfect agreement with the experimental value [128].

Oxygen octahedral rotations

At room temperature, in which usually the experiments are performed, the $SrTiO_3$ is in a cubic structure while $LaAlO_3$ is rhombohedral ($a^-a^-a^-$ in Glazer notation). In addition, it was shown in reference [131] that the octahedral tilts are present in $LaAlO_3$ and penetrate, to a certain extent, into $SrTiO_3$. However, our calculations are not taking

Lattice parameters					
	STO	LAO			
	Cubic	Cubic	Tetragonal		
	a	a	a	c	c/a
expt.	3.905[a]	3.811[b]	3.905	3.75	0.96
B1-WC	3.880	3.791	3.880	3.747	0.97
VPSIC	3.932	3.842	3.932	3.617	0.92
LDA	3.889	3.815	3.889	3.694	0.95

Table 3.1: *Cell parameters with few functionals.* [a] *[129],* [b] *[130].*

any oxygen rotation tilts into account neither in $SrTiO_3$ or in $LaAlO_3$. The main reason is that it would have been more complex and time consuming to model these instabilities that only appear in larger simulation cells. It nevertheless has to be noted that these octahedral tilts are affecting some properties of the systems such as the dielectric constant or the tetragonality (c/a), which are important parameters of this study. Fortunately, a work by Spaldin [132] studied these effects in $LaAlO_3$ (001) under biaxial strain. The author have shown that the usual $a^-a^-a^-$ LAO structure ($R\bar{3}c$) changes to $a^-a^-a^0$ ($Imma$) tilts under the biaxial strain imposed by STO, as confirmed in reference [133]. These in-plane tilts are usually leading to a reduced c-parameter, which will not change our conclusions in chapter 4, and, anyway, they effect on the c/a ration is negligible. Finally, our results on dielectric constant are in agreement with the experimental results.

Electronic band gap

Two key bulk quantities for the formation of the 2DEG are the band gap and the dielectric constant. Concerning band gaps, reported in Table 3.2, both B1-WC and VPSIC functionals give a substantial improvement over the same values of the respective reference functionals (GGA and LDA), shrinking the discrepancy with the experiment down to just about 10%. Notice that for STO this discrepancy has a different sign for B1-WC and VPSIC, respectively, but this can be due to the respective starting point (i.e. the LDA and GGA results) which are also quite different. Both theories coherently predict the LAO tetragonal distortion induced by the STO substrate to have a relatively minor effect ($\sim$ 0.1 eV increase) on the LAO band gap. These much improved band gaps are instrumental to relieve the well know systematic error affecting *ab initio* predictions of

band alignment at the interface.

Band gap						
		LDA	VPSIC	GGA	B1-WC	Expt.
$SrTiO_3$	ΔE_i	1.69	2.94	2.0[d]	3.57[b]	3.25[a]
	ΔE_d	2.04	3.30		3.91[b]	3.75[a]
$LaAlO_3$	ΔE_i	2.83	5.23	3.70[d]	5.19	5.6[c]
	ΔE_d	3.17	5.51		5.50	5.60[c]
$LaAlO_3^T$	ΔE_i		4.84		5.23	
	ΔE_d		5.21		5.62	

Table 3.2: *Direct (ΔE_d) and indirect (ΔE_i) band gap energies (in eV) for cubic STO, cubic LAO, and tetragonal-distorted LAO^T, calculated within LDA, VPSIC, GGA, and B1-WC, compared to the experimental values.*
[a] *[134]*, [b] *[114]*, [c] *[135]*, [d] *[52]*

Dielectric constant

As for the dielectric constant of STO and LAO, the calculations reported in Table 3.3 are in satisfying agreement with the experimental data [136] relative to the room-temperature cubic phase (whereas the large STO value reflects the presence of the soft ferroelectric mode). Notice that the LAO tetragonal distortion changes quite sensibly the screening properties in the interface-orthogonal direction, reducing ϵ_{33} by about 20 % of its value. We will see in the following that this aspect is relevant to the mechanism of interface metal/insulator transition which follows the Zener breakdown.

We will show that the dielectric constant is a key parameter that affects the appearance of the 2DEG but also its confinement. The advantage of the B1-WC is to properly describe the structure but also the electronic properties. Another method widely used is LDA +U or GGA +U, which arbitrarily add some correlation on some atoms (here the Ti) to increase the band gap and go against the usual under estimation of the functional. However this improvement can affect some other properties, which are fundamental for this study, such as the hardness of the polar phonon and by this fact the dielectric constant.

Dielectric constant			
	ϵ_{11}	ϵ_{33}	exp
STO_C	265	265	300[a]
LAO_C	28	28	21-24[b]
LAO_T	37	22	

Table 3.3: *Dielectric constant predicted by B1-WC functional for cubic (STO_C and LAO_C) and constrained LAO (LAO_T). Experimental values are coming from references [a] [137] and [b] [138].*

3.2 The band offset

The question of the band alignment is crucial since the electronic behavior of the heterostructure highly depends on it especially when the system is doped. The band alignment is a well-established problem in semiconductors physics however in oxides new difficulties may arise. A complete study of this question is not the aim of this work, however additional information can be obtained in the study of Stengel *et al.* [139] as a discussion on metal induced gap states [140] in $LaAlO_3$-$SrTiO_3$ systems.

The usual semiconductor heterostructure combines two materials with unequal band gaps. The Fermi level of both materials has to match across the interface, resulting to the relative alignment of the bands with two different possibilities[1], see figure 3.2. The values of the band gaps are recovered if evaluated sufficiently far away from the interface. The heterostructure is then electronically described by the two bulk band gaps and the misalignment of the valence bands (valence band offset, VBO) and of the conduction bands (conduction band offset, CBO). The bands in each part of the heterostructure are flat and do not evolve with the thickness of the two materials. However, in a polar/non-polar heterostructure the problem is not similar. Indeed, for a LAO thin film on a STO substrate, the bands evolve with the $LaAlO_3$ thickness due to the built-in electric field. To obtain a case similar to the semiconductors i.e. the flat bands, the electric field has to be canceled exactly as when 0.5 e^-/S are transferred in the fully compensated system. However, to model such a system, an infinitely large $LaAlO_3$ film is needed.

Another possibility is to use the superlattice method described in chapter 2. In this case, a new difficulty arises due to the boundary conditions that are imposed in the DFT calculations. Indeed, the superlattice is an infinite system that consist of a succession of

[1] There is in fact 3 possibilities, the last one being type III or the broken type.

thick $SrTiO_3$ and $LaAlO_3$ films represented by a simulation cell that contains two interfaces. To construct a stoichiometric superlattice, it is mandatory to have the two different types of interface, n and p. When considering a np superlattice within periodic DFT, an electric field appears in STO due to the closed circuit electrical boundary conditions imposed by the periodic boundary conditions[141]. However for the case studied in this thesis i.e. a LAO film on a STO substrate under open circuit boundary conditions in which no electric field in STO is expected, this np superlattice geometry is therefore not appropriate. Another attempt is to create two n-type interfaces, changing the system into a non-stoichiometric one with an additional $(LaO)^+$ and $(TiO_2)^0$ layers. The system is then doped by the additional charge and to equilibrate, half an electron is transferred at both interfaces. This value corresponds exactly to the charge density needed to cancel the polar mismatch i.e. to reach the full compensation limit. The nn superlattice is similar to conventional semiconductor heterostructures with flat energy levels and by this fact the relative alignment is independent of the $LaAlO_3$ or $SrTiO_3$ thicknesses. We expect that this nn superlattice is a good trick to simulate an infinitely large LAO film. Unfortunately, the use of the nn superlattice can only approximate the band offset since the system is doped and then conducting, which may affect the alignment. A more rigorous method is given in reference [139].

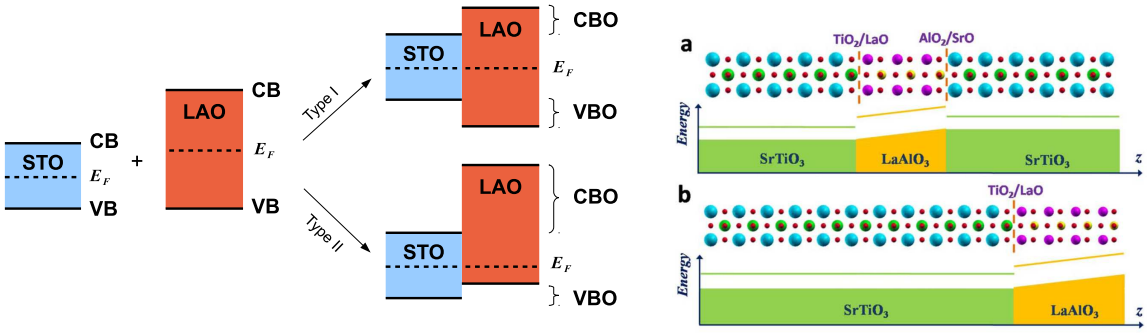

Figure 3.2: *Left: Schematic picture of the band structure in STO, LAO and the heterostructure. Right: Structure and potential in np superlattice and n slab respectively in a) and b). Figure adapted from reference [142].*

Some previous works have already calculated the band offset of $LaAlO_3$-$SrTiO_3$ systems without any real agreement. Indeed, the predictions of references [53, 64, 142–144] are in a large range: -0.9 to 1.1 eV for the valence band offset (VBO). The first reason may be attributed to the well know difficulty of conventional functionals to properly describe the band gap [145, 146] but the different conditions in which the system is evaluated is another possible reason. These conditions should be properly handled in order to

reach a careful and unbiased determination of the band offset. For this reason and to obtain a complete description of the LAO/STO system within the framework of the hybrid B1-WC functional, we recomputed these values. As discussed previously, we used the superlattice approach with two n-type interfaces with different thicknesses, already described in section 2.4.2.

We proceed as follows: the VBO may be extracted from the disalignment of orbitally projected density of states (DOS) (specifically the DOS with a $2p$ character on the most bulk-like TiO_2 and LaO layers) across the interface. This give $\sim$ -0.2 eV, with the top of the valence bands of LAO lower than the top valence bands of STO i.e. type 1, in fair agreement with the experimental value of -0.35 eV [75]. With the same approach we evaluated the misalignment between the Ti $3d$ and the La $4d$ states giving a CBO of 1.5 eV. Notice also that in the most bulk-like layers, the band gaps of bulk STO and LAO are correctly recovered.

As a confirmation of these values, we also performed another calculation for the insulating interface (i.e. before the Zener breakdown in a two-dimensional slab). In order to extract the effect of the field, we extrapolated the zero-field top valence band in the LAO side assuming a constant electric field in LAO of 0.24 V/Å (according to our results, see later) corresponding to a change of $\sim$0.9 eV per cell. This method can only give a rough approximation but is, however, in good agreement with the previous result of nearly aligned valence bands.

Finally, in the electronic reconstruction model, see the next section, the Zener breakdown occurs when the band gap is reduced to zero. For the n-type interface, this closing is intrinsically linked to the bang gap of $SrTiO_3$ and the VBO. We will show in the next section that $E_g^{\mathrm{STO}} + VBO$ (or Δ) is estimated by our calculations to be slightly bigger than E_g^{STO}, in good agreement with a small VBO of type 1.
The same method was applied to a superlattice with two p-type interfaces, $SrTiO_3$(6.5)/-$LaAlO_3$(6.5). The VBO we calculated in this case is smaller than -0.1 eV and the CBO is between 1.5 and 1.7 eV. These results are comparable to the case of the superlattice with two n-type interfaces. In fact, the valence bands correspond to the similar O $2p$ states in both compounds, justifying intuitively why they are almost aligned.

The VBO and CBO problem was already mentioned in reference [142] and, in this work, we used 3 different approaches, all in agreement with a small value ($\sim$ 0.2 eV) of the VBO of type 1. Finally, the band offsets obtained with the hybrid functional are comparable to LDA or GGA calculations that applied scissor or dipole corrections. For non perfect

interfaces, as in the case of experimental samples, the band alignment can be affected for instance by the intermixing. Nevertheless, as explained in reference [93] (see chapter 5), this has only a small effect and the band alignment must be in a range between 0 and -0.2 eV. Thus the description given in figure 3.3 is representative of the electronic behavior in the $SrTiO_3/LaAlO_3$ thin film systems.

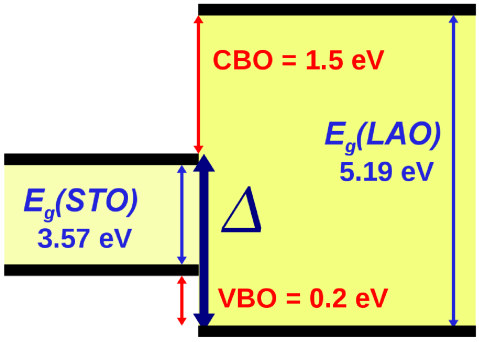

Figure 3.3: *Band alignment in the $SrTiO_3$(8.5)/$LaAlO_3$(8.5) supercell. The values, in agreement with band gaps obtained in table 3.2, are calculated using the central layer in LAO and STO. $\Delta = E_g^{(\mathrm{STO})} + \mathrm{VBO} = 3.77$ eV is the key parameter leading the Zener breakdown.*

3.3 Polar catastrophe and Zener breakdown

Typically in conventional semi-conducting heterostructures, the built-in polarity is compensated by interface or surface atomic reconstructions. In oxide interfaces, however, another mechanism is possible, since they typically include transition metal atoms (e.g. Ti) which are much keener than conventional s,p elements to change their bulk valence state (e.g. from Ti^{4+} to $Ti^{3.5+}$). This allow for the redistribution of charges across the interface and the restoration of the overall electrostatic equilibrium conditions. As a byproduct of this "electronic reconstruction", a bi-dimensionally confined electron gas remains trapped in the Ti 3d orbitals.

In the following, we revisit the fundamental electrostatic behavior of the $LaAlO_3$-$SrTiO_3$ interface using the elegant formalism developed in reference [25], based on the conservation of the normal component of the displacement field **D** across the interface. In addition, Bristowe *et al.* [24] observed that in the centrosymmetric systems, the symmetries impose the center of the Wannier functions to localize at the center of the atoms. For this specific reason, there is no additional dipoles in the system. In the end, the works of Bristowe and Stengel show that considering the formal point charges for the

anions and cations (±e for LAO and 0 for STO) is enough and in agreement with the new theory of polarization.

In the (001) direction, the LAO layers can be assimilated to a series of capacitors with LaO^+ and AlO_2^- layers, corresponding to surface charges $\sigma_0^{\mathrm{LAO}} = 0.5\ \mathrm{e}^-/\mathrm{S}$, see figure 3.4a. Due to $\pm e$ polarity of each LAO monolayer, LAO possesses a dipole moment of $d = -ec/2$, where c is the thickness of a single LAO unit. On the other hand, STO planes are neutral and there is no dipole moment. The formal polarizations of both materials are then given by:

$$P_0^{\mathrm{STO}} = 0 \tag{3.3.1}$$

$$P_0^{\mathrm{LAO}} = -\frac{e}{2S} \tag{3.3.2}$$

In the case of a STO/LAO/vacuum system, as schematically represented below, the orthogonal component of the displacement field in each compound is:

$$D^{\mathrm{STO}} = \epsilon_0 E_0^{\mathrm{STO}} + P_0^{\mathrm{STO}} \quad ; \quad D^{\mathrm{LAO}} = \epsilon_0 E_0^{\mathrm{LAO}} + P_0^{\mathrm{LAO}} \quad ; \quad D^{\mathrm{vac}} = 0. \tag{3.3.3}$$

STO	**LAO**	**vacuum**

According to basic electrostatics, in absence of free charges, the normal component of the displacement field at any interface has to be preserved[2], meaning here that $D = 0$ in the whole system due to the vacuum. This simple relation, the equations in 3.3.3 and the polarizations given in equations 3.3.2 impose that there is no field in STO and that a built-in electric field appear in LAO: $E_0^{\mathrm{LAO}} = P_0^{\mathrm{LAO}}/\epsilon_0$. Not taking into account any screening ($\chi = 0$, $\epsilon_r = 1$), the expected electric field in LAO is 5.94 V/Å, which would produce a drop of potential of about 24 V per unit cell.

Since $LaAlO_3$ is an insulator, the material will polarize under the effect of the electric field, leading to a depolarizing electric field and the corresponding surface induced charges $\sigma_{ind}^{\mathrm{LAO}}$. The depolarizing field $\mathbf{E}_{ind}^{\mathrm{LAO}}$ screens $\mathbf{P}_0^{\mathrm{LAO}}$ with respect to the dielectric constant. The resulting electric field $\mathbf{E}^{\mathrm{LAO}}$ and surface charges σ^{LAO} are given by (see figure 3.4b):

$$E^{\mathrm{LAO}} = E_0^{\mathrm{LAO}} - E_{\mathrm{ind}}^{\mathrm{LAO}} = \frac{P_0^{\mathrm{LAO}}}{\epsilon_0 \epsilon_r^{\mathrm{LAO}}} = 0.24\ V/\mathring{A} \tag{3.3.4}$$

$$\sigma^{\mathrm{LAO}} = E^{\mathrm{LAO}} \epsilon_0 = 0.02\ e^-/cell \tag{3.3.5}$$

$$\sigma_{\mathrm{ind}}^{\mathrm{LAO}} = \sigma_0^{\mathrm{LAO}} - \sigma^{\mathrm{LAO}} = 0.48\ e^-/\mathrm{cell} \tag{3.3.6}$$

[2]It is a direct consequence of the interface theorem [26].

where we used the dielectric constant for bulk LAO, $\epsilon_r = 25$.

We estimate, with the electronic reconstruction model, the built-in electric field to be equals to 0.24 V/Å. As consequence, the electrostatic potential in LAO evolves linearly with the thickness, the slope corresponding to the value of the field. Each additional LAO unit cell (3.75 Å for strained LAO) corresponds roughly to an increase of $3.75 \times E^{\mathrm{LAO}} = 0.9$ eV. A schematic representation of the bands is show in figure 3.5(left).

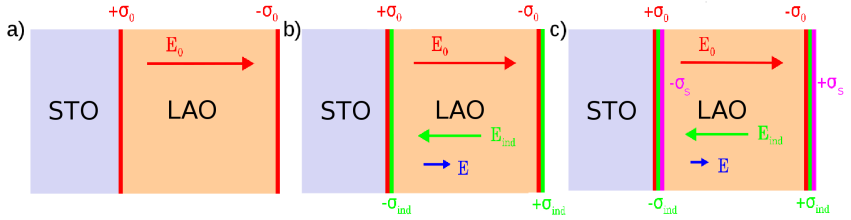

Figure 3.4: *Capacitor model for the LAO/STO system (a) Electric field,* $\mathbf{E}_0$ *in LAO due to* $\pm e$ *polarity of each monolayer. b) Induced charges (green) due to dielectric material reducing the field to* $E = 0.24$ *V/Å (blue). c) Charges are transferred,* σ_S *(purple), and the electric field* **E** *decreases.*

The first-principles calculations on two-dimensional systems[3] are in agreement with the previous model. Indeed, in figure 3.5(right) is represented the electrostatic potential for n = 2, 3 and 4 (black, red and green respectively). As expected, in STO, the potential is flat i.e. no polarization arises. In $LaAlO_3$, however, the potential drop, corresponding to the electric field through LAO, is roughly equal to 0.24 V/Å for the three thicknesses. This estimation of the field by first-principles and the equation 3.3.7 give a relative permittivity of 25, in good agreement with our previous first-principles calculations on bulk but also of the experimental values, both given in table 5.3.1.

We predicted, with the electronic reconstruction model, that each additional $LaAlO_3$ unit cell reduces the gap by ~ 0.9 eV. In figure 3.6, we represent the electronic density of states (DOS) for the 3 thicknesses. The band gaps are respectively of 2.30, 1.35 and 0.40 eV for n equals 2, 3 and 4 unit cells, corresponding to a decrease of approximately 0.95 eV per additional cell. It is the titanium $3d$ orbitals that move toward the O $2p$ orbitals of LAO. For $n = 4$, the system is still insulating but with a small band gap of $E_g = 0.4$ eV.

In the electronic reconstruction model, the metal/insulator transition takes place via the closing of the band gap i.e. through a Zener breakdown. This special limit is reached for a specific thickness, call the critical thickness t_c. At that particular point, the drop of

[3] $\mathrm{vacuum}/(SrTiO_3)_7/(LaAlO_3)_n/\mathrm{vacuum}$.

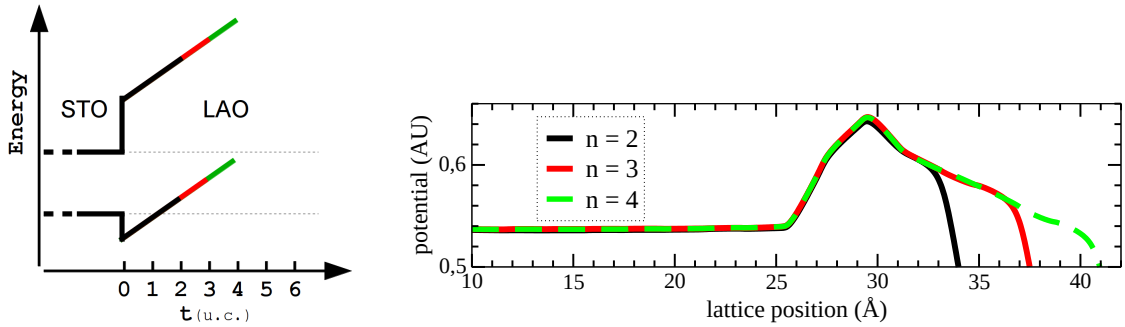

Figure 3.5: *Left: Schematic picture of the band structure with the bending of the LAO bands. Right: Macroscopic average of the electrostatic potential in vacuum/STO_7/LAO_n/vacuum system with n=2, 3 and 4. The slope corresponds to a built-in electric field of 0.24 V/Å through LAO for each thicknesses.*

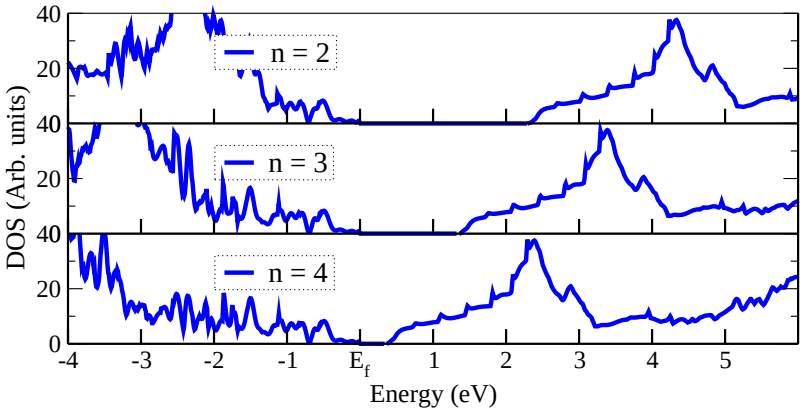

Figure 3.6: *The total DOS obtained for insulating slab systems. Band gaps are 2.30, 1.35 and 0.40 eV respectively for n=2, 3 and 4.*

potential Δ is identical to the band gap of STO plus the additional valence band offset i.e. $\Delta = E_g^{\mathrm{STO}} + VBO = 3.77$ eV. For this reason, t_c can be evaluated as the thickness needed to reach a drop of potential Δ if the slope is the electric field E, giving:

$$t_c = \frac{\Delta}{E^{\mathrm{LAO}}} = \frac{\epsilon_0 \epsilon_r^{\mathrm{LAO}} \Delta}{e P_0^{\mathrm{LAO}}}, \tag{3.3.7}$$

as represented in figure 3.7(left). With $c^{\mathrm{LAO}} = 3.75$ Å, $\epsilon_r^{\mathrm{LAO}} = 25$ and equation 3.3.7 we estimate the critical thickness t_c to be ≈ 4.2 unit cells. The critical thickness depends on the band gap of $SrTiO_3$ (plus the valence band offset), on the $LaAlO_3$ dielectric constant and on the $LaAlO_3$ formal charge, all being intrinsic parameters. In addition, equation 3.3.7 accounts for an ideal interface and surface. Since each additional LAO unit cell corresponds to a drop of ~0.9 eV, it is clear that our first-principles calculations also predict a critical thickness between 4 and 5 unit cells. We need to mention here that this prediction is larger than the metal/insulator transition observed experimentally

which is between 3 and 4 unit cells. However, this can be certainly attributed to the overestimation of the band gap of $SrTiO_3$ (3.6 eV instead of 3.2 experimentally), a value that we also used in the electronic reconstruction model.

When the critical thickness is reached, each additional LAO cell contains valence electrons that are at higher energy compare to the STO conduction bands. These electrons will therefore be transferred from the LAO surface to the STO interface to minimize the energy through a mechanism usually referred to as a Zener breakdown. Due to this mechanism, the valence band edge in LAO remains pinned to the conduction band minimum in STO, see figure 3.7, and the electric field is given by

$$E^{\mathrm{LAO}} = \frac{\Delta}{t^{\mathrm{LAO}}}. \tag{3.3.8}$$

As consequence, since Δ is constant, the electric field decreases for increasing thicknesses as 1/t. The electron transfer gives rise to a new kind of charge in the system, the free charge of the 2DEG, with density σ_S, see figure 3.4. From equations 3.3.7 and 3.3.8 we can evaluate the quantity of free charge in $SrTiO_3$ [51]:

$$\sigma_S = \sigma_0^{\mathrm{LAO}} + \epsilon_0 \epsilon_r^{\mathrm{LAO}} \frac{\Delta}{t^{\mathrm{LAO}}} = \sigma_0 \left(1 - \frac{t_c}{t^{\mathrm{LAO}}}\right). \tag{3.3.9}$$

In the electronic reconstruction model, the free charge density σ_S depends on the dielectric constant, the band gap of STO and the LAO thickness.

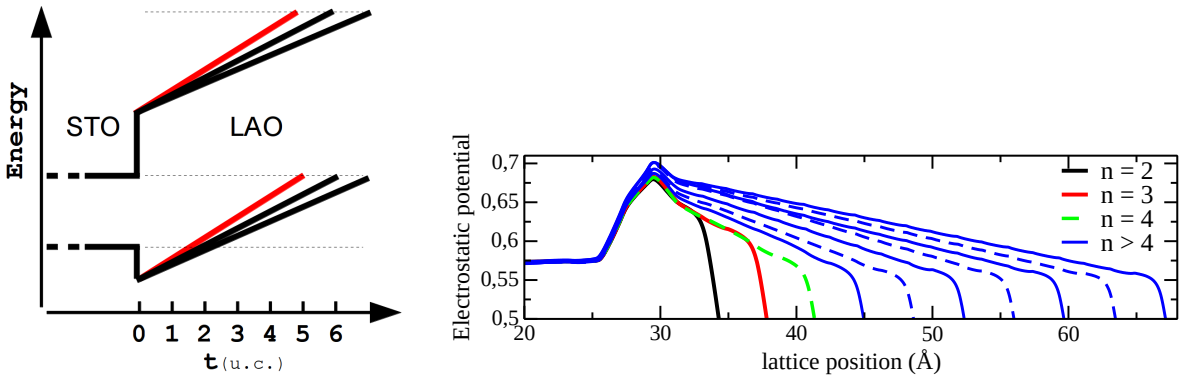

Figure 3.7: *Left: Evolution of the electronic bands in LAO with in red the band at the critical thickness, t_c and in black the bands for $t > t_c$. Right: Macroscopic average of the electrostatic potential with additional blue lines corresponding to n>4.*

The main predictions of the polar catastrophe model after the electronic reconstruction are the thickness dependence of the density of charges and of the electric field. We use our first-principles calculations on vacuum/$(SrTiO_3)_7$/$(LaAlO_3)_n$/vacuum systems, for n $\geq$ 5, to test the agreement between the two approaches. For each thicknesses, the comparison

is done for the electric field and the density of charges within the two methods. In figure 3.7(blue) is represented the electrostatic potential for $n > 4$ where, as expected, the slopes of the blue lines decrease for larger n. In addition the potential drop is pinned as represented by the dashed line.

As shown in the density of state in figure 3.8, the band gap disappeared for n ≥ 5. This corresponds to the Ti $3d$ conducting states that cross the Fermi level and start to be occupied. The Ti $3d$ electrons are free[4] and rely in the Ti t_{2g} bands since these are the first accessible orbitals with the lowest energy. In figure 3.8 is represented the charge density in each Ti for a given thickness. As the LAO thickness increases, the density of free charges increases with respect to equation 3.3.9, corresponding to additional states below the Fermi level. A complete description of the orbitals occupancy and confinement is done in chapter 6.

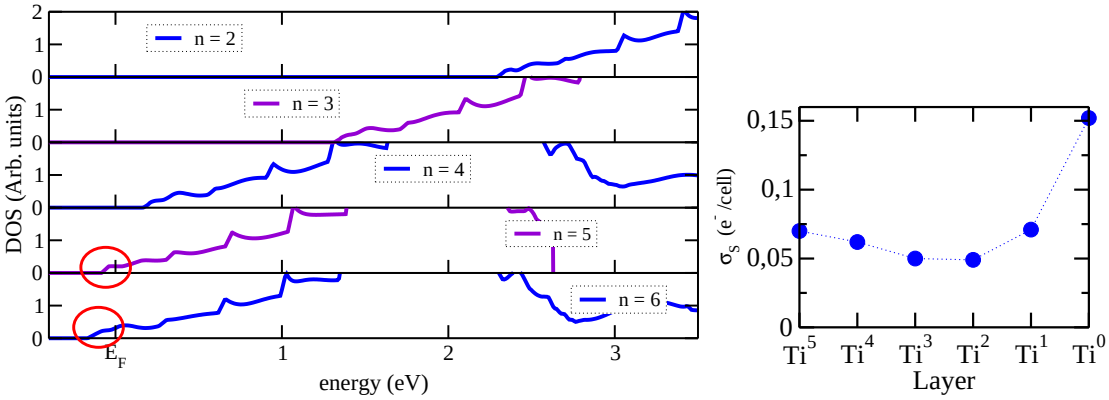

Figure 3.8: *left: Evolution of the DOS of interface Ti atoms with the LAO thickness. Right: The total quantity of charge in the Ti orbitals, Ti^0 being at the interface.*

In figure 3.8 is shown the Ti $3d$ orbitals reaching the Fermi level for n equals 5 and 6. The charges density are equals to 3×10^{13} and 7×10^{13} e/cm^2 respectively for 5 and 6 unit cells, in very good agreement with other calculations [51]. The charge densities for each thicknesses are represented in figure 3.9 (dots) as the evolution predicted from the polar catastrophe model in equation 3.3.9 (line). It is clear that the charge densities obtained by first-principles calculations fit well with the polar catastrophe predictions. The transfer of charge is progressive and only reach the 0.5 e^-/S^5, corresponding to a fully compensated system, for infinitely large thicknesses.

[4]Some electrons are possibly highly localized due to Anderson mechanism.

[5]or $\sim 3 \times 10^{14}$ e/cm^2.

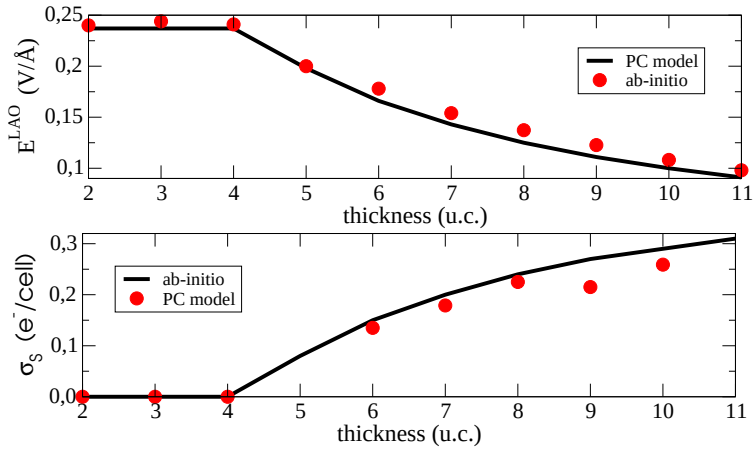

Figure 3.9: *Evolution of (a) the electric field inside the LAO layer, (b) the surface charge density at the LAO/STO interface*

Discussion

In this section, we have described the physics of an ideal $LaAlO_3$-$SrTiO_3$ interface, without hte existence of any kind of defect or extrinsic effect. The first-principles calculations predict a Zener breakdown at increasing thicknesses in close agreement with a simple electrostatic model. The main features can be summarized as follows:

$\rightsquigarrow$ Before t_c, the appearance of a constant built-in electric field in LAO,

$\rightsquigarrow$ At t_c, the closing of the band gap and the metal/insulator transition through a Zener breakdown.

$\rightsquigarrow$ After t_c, the appearance of free charges in Ti $3d$ orbitals, the 2DEG. Its density increases with the thickness while the electric field is reduced.

Finally, we have shown that first-principles calculations, using the hybrid B1-WC functional, reproduce these key elements. The main reason is that, in the pristine $LaAlO_3$-$SrTiO_3$ system, the electronic reconstruction is the only possible way to cancel the polar mismatch. No cations exchange or oxygen vacancies can form since the structure is fixed to a perfect $LaAlO_3$-$SrTiO_3$ system. A direct comparison with experimental results is certainly more complex due to the presence of defects in samples that enable other possible mechanisms of reconstruction. As first step, we focus here on the model and the first-principles results, leaving the relation with experiments for further discussions.

Some criticisms can be address to equation 3.3.7. First of all, the dielectric constant in LAO depends on the electric field as already studied by Chen *et al.* [142]. Moreover the electric field is not constant everywhere in LAO, especially close to the surface and the interface, and is usually averaged. Additionally, the electrostatics can be affected by the

chemical species (dipole at the interface, see later) or the defects, like the cationic inter-diffusion at the interface. This, however, only affects locally the interface, and cannot affects the built-in electric field as showed in [12]. In addition the pinning of the bands is not precisely exact as again discussed in the recent review of Bristowe [12]. However, despite these approximations, the electronic reconstruction model and our first-principles calculations are in very good agreement.

The electronic reconstruction can be considered as a naive view of the $LaAlO_3$-$SrTiO_3$ mechanism. However, we need to mention that, the only systems that can be described are the equilibrium ground state before and after the transfer. This means that the exact mechanism that occurs between these 2 equilibrium states is not know and is not affecting the 2 final states. Saying for instance that the electrons in the additional LAO cell are transferred to the STO is only a picture helping to visualize the situation. Only the two equilibrium states are physically representative no matter how or when the electrons are transferred.

3.4 Atomic relaxation

Geometry

In the previous section, only the results in relation with the polar catastrophe model were shown. In this one, a complete structural description of both fully relaxed $(LaAlO_3)_m$/-$(SrTiO_3)_n/(LaAlO_3)_m$ and vacuum/$(SrTiO_3)_7/(LaAlO_3)_n$/vacuum is done. The usual way to present the structure is to describe the structural distortions compare to the formal constituents.

The $SrTiO_3$ part of the structure is close to bulk geometry with an average lattice parameter perpendicular to surface of 3.88 Å. However, at the interface (and surface if not fixed to bulk STO positions) STO is locally distorted due to the dipole created by the interface. The $LaAlO_3$ has a less bulk-like structure with an average lattice parameter of 3.84 Å. This is much larger than the 3.75 Å expected when the LAO is under an epitaxial strain, see table 3.1. Compared to the in-plane constrained LAO, the atoms are globally shifted leading to the expansion of the cell, see figure 3.10. This effect is expected due the presence of the electric field in $LaAlO_3$, knows as the electrostriction and further discussed in chapter 4. This field implies a force on the ions but with different amplitudes, leading to an orthogonal displacement and a relative motion of the anions and cations,

see figure 3.10. As consequence, perpendicularly to the interface, the La and O (Al and O) atoms are not longer belonging to the same plane. We have to define an average plane that is at equal distance from these two atoms. The rumpling is then define by the distance of these atoms relatives to the average plane, or equally, by the cation-anion distance divided by 2. This average plane is always shifted, due to electrostrictive effect, in a way that the cell expands. The two planes, LaO and AlO_2, have a different shift, and the two different planes do not occupy half of the volume each anymore i.e. one is larger that the other, see figure 3.10. The atomic displacement of La and Al atoms are larger than for oxygen atoms and in opposite direction leading to a displacement of the average plane and the expansion of the lattice parameter. The average lattice parameter (3.84 Å) is then an average of large ($\approx$ 2.1 Å) and small ($\approx$ 1.74 Å) interplane distances. The whole picture is represented in figure 3.10.

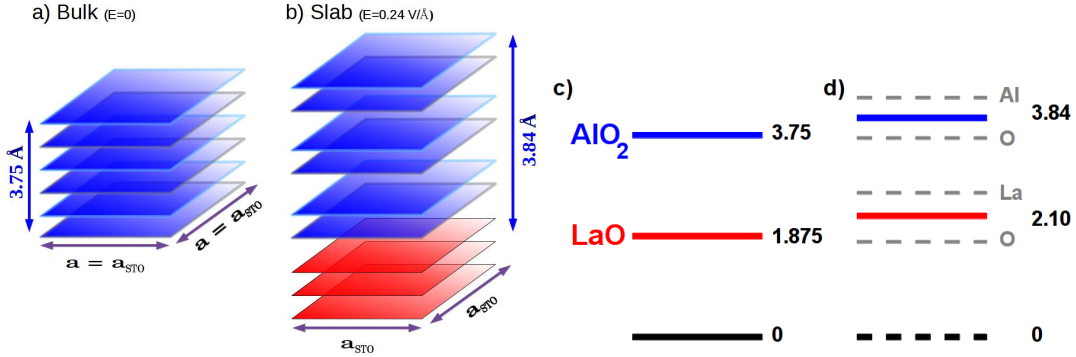

Figure 3.10: *Left: The layers, LaO and AlO_2, for the bulk $LaAlO_3$ with in plane tensile strain. The perpendicular lattice parameter relaxes to 3.75 Å with equidistant LaO and AlO_2 planes. Right: The electric field leads to the expansion of the perpendicular lattice with different inter-plane distances.*

Rumpling

We just shown that there is a direct link between the electric field and the structural distortions in LAO. The later can thus be a useful signature to study the electric field. For instance, in figure 3.11 we show that the buckling and the rumpling effects decrease with increasing thicknesses. This is in perfect agreement with equation 3.3.8 that predicts a smaller field for larger thicknesses. Additionally, the atomic displacements, larger for LaO compared to AlO_2, are relatively constant in all the system, showing that the macroscopic average of the electric field is a good approximation (except for surface and interface layers). If we express the rumpling ϕ in Å and the field E in V/Å, we have the two

following relations: $E/\phi^{LaO} \approx 2.2$ and $E/\phi^{AlO_2} \approx 3.4$. The evolution of the electric field and rumpling with the thickness is represented in figure 3.11.

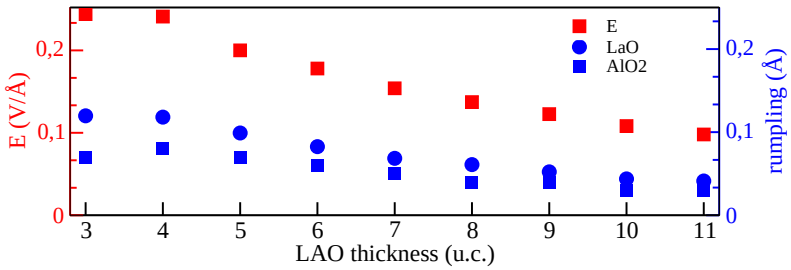

Figure 3.11: *The rumpling in Å (blue) and the electric field in V/Å (red) versus the thickness in unit cell.*

Interdiffusion

Previously, we argued that the atomic inter-diffusion is only modifying the electrostatic at the vicinity of the interface. In addition it cannot affect the electric field [12]. To check these affirmations, we calculated the electrostatic potential in non pristine systems (described in section 2.4.2), still with the B1-WC functional. Two types of inter-diffusion are considered, A cations exchange only (La $\leftrightarrow$ Sr) or A and B cations exchange (La $\leftrightarrow$ Sr and Al $\leftrightarrow$ Ti). This exchange is only in a 1 unit cell range away from the interface. The potentials are represented in figure 3.12 for a 4 LAO unit cell thick systems.

Such an inter-diffusion can only affect the electrostatic at the interface leaving unchanged the field in LAO. This is a direct consequence of the Gauss's law. Indeed, the results shows that the electrostatic potential is the same for the 3 cases in the LAO region, close to the surface (right). In addition the potential in the STO region stays flat as expected. The electric field is then identical in the 3 cases except close to the interface. Closer to the interface, the dipole is affected by the cation mixing, possibly leading to a rigid shift of the potential. Indeed, in case of the A-type inter-diffusion, the potential is shifted in the STO part (the 3 curves are manually shifted to align in the LAO surface region). This shift can reduce or increase the band gap of the system, potentially changing the critical thickness $t_c \rightarrow t_c \pm 1$. However, this inter-diffusion is not expected to dope the system since it corresponds to an exchange of donor and acceptor across the interface.

The cations exchange can affect the intrinsic parameters of equation 3.3.7. However, we have shown in reference [93] (presented in chapter 5), that the dielectric constant of the LAO-STO alloy is very close to the one of $LaAlO_3$. In addition, since the valence band

offset is mainly due to O $2p$ orbitals of both materials, VBO is not expected to change in presence of inter-diffusion at fixed stoichiometry.

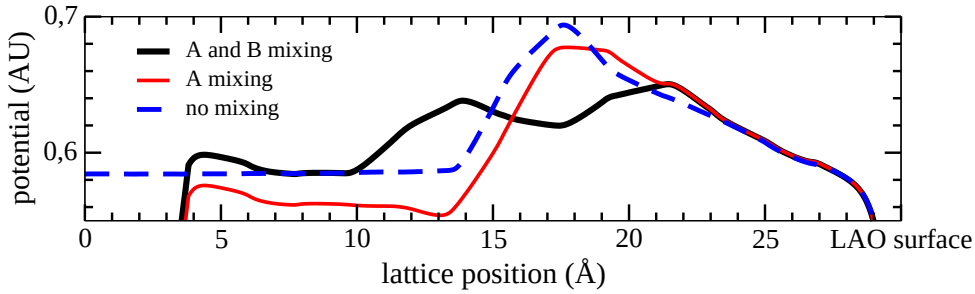

Figure 3.12: *The electrostatic potential for 3 different cases: pristine interface (blue dashed line), inter-diffusion of A atoms (red line) and inter-diffusion of A and B atoms (black line).*

3.5 The p-type interface

In this section, we briefly mention the p-type interface, usually less studied because, experimentally, no metal/insulator transition was observed. The concepts are the same that for the n-type interface. However, in this case the dipole at the interface is reversed as the slope of the electrostatic potential in LAO. The bands are then bend in opposite direction compare to n-type, see figure 3.13. The Zener breakdown occurs when the bottom of the conduction bands of $LaAlO_3$ reaches the top of the valence band in $SrTiO_3$, creating free holes in the O $2p$ orbitals. The equation 3.3.7 is still valid at the condition that, it is the band gap of $LaAlO_3$ that need to be used to estimate Δ. Since $E_g^{\mathrm{LAO}} > E_g^{\mathrm{STO}}$, the critical thickness is larger compare to the n-type case and estimated to $t_c \approx 6.2$. As for the n-type interface, the electric field is constant until t_c is reached, and then E decreases with the LAO thickness, as represented in figure 3.13. Without going into too much detail, one can observed in figure 3.14 the spreading on the charge carriers into the whole heterostructure, far from the behavior of electrons in n-type interface that rely in Ti $3d$ states. Additional information are given in chapter 6.

The purpose of this section is not to redo all the analysis as for the n-type interface, but rather to show that first-principles calculations predict the p-type interface to have a metal/insulator transition. For a while, this wrong prediction was a strong argument against the electronic transfer mechanism, but also against the real ability of first-principles calculations to properly describe the $LaAlO_3$-$SrTiO_3$ system. However, it only

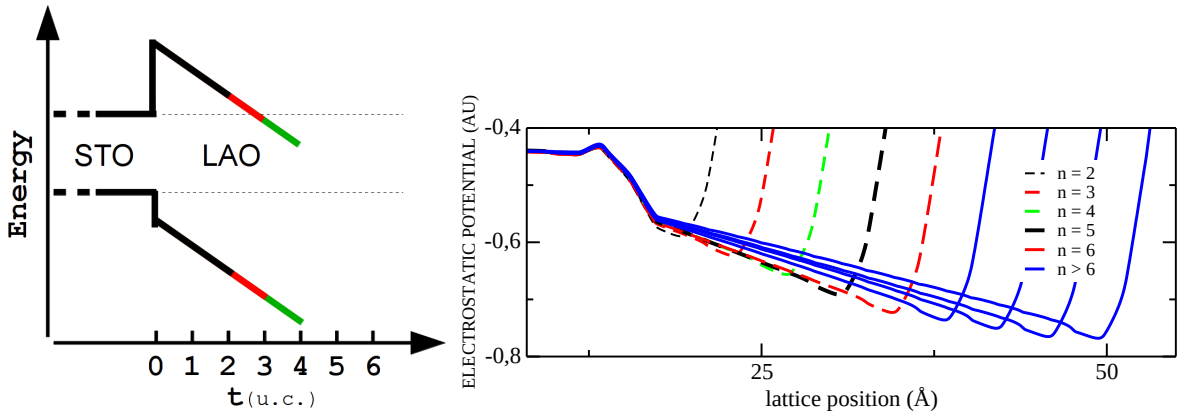

Figure 3.13: *Left: schematic representation of the bands in a p-type interface system. Right: Electrostatic potential obtained by first-principles calculations for several thicknesses.*

means that, in a real p-type sample, another mechanism is at the origin of the cancellation of the polar mismatch, while in the present calculation, the electronic transfer is the only possibility.

We already discussed this problem in chapter 1. Even if some systems reconstruct via cationic exchange or defects formation, we want to discuss the possibility of an electronic reconstruction in the systems where the polar mismatch exists. Chapters 4 and 5 are in fact dedicated to this study.

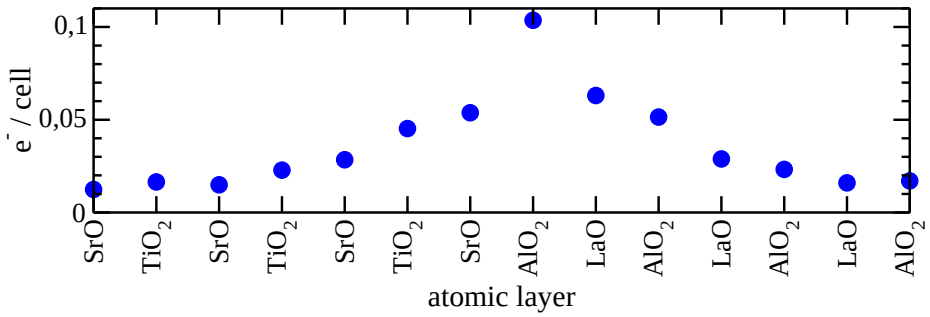

Figure 3.14: *Charge density in O 2p states. In p-type interface, the carriers are not confined and spread in the whole heterostructure.*

3.6 Conclusion

A complete description, starting with the bulk compounds, of the pristine $LaAlO_3$-$SrTiO_3$ system was complete with an advanced functional: B1-WC. We shown that problematic but key parameters, such as the dielectric constants, the band gaps or the band offsets for

instance, are well reproduced with this approach. We tackled the $LaAlO_3$-$SrTiO_3$ system by different manners: the 2D stacking and the superlattice, each time with different thicknesses. We have shown that simple electrostatic and Zener breakdown model fit perfectly well with the first-principles calculations on a pristine $LaAlO_3$-$SrTiO_3$ heterostructure. The main reason is that, in that case, the electronic reconstruction is the only way to cancel the polar mismatch leading to the polar catastrophe. The critical thickness, the carrier densities or the built-in electric field are only few examples of the good agreement with the two different approaches.

Experimental samples are, however, far from being perfect. The oxygen vacancies, atomic mixing or adsorbates are only examples of the additional defects that can alter the properties of the system. In real samples, these defects are difficult to avoid and for that reason, a part of the community at least believes that these defects are the only cause of the 2DEG appearance. For this reason, the results on pristine $LaAlO_3$-$SrTiO_3$ systems, presented in this chapter, are only one piece of the puzzle. Nevertheless, we shown that the B1-WC functional approach is satisfactory and can be used for more advanced calculations.

In the pristine $LaAlO_3$-$SrTiO_3$ interface, the electronic reconstruction is the only way to cancel the polar mismatch leading to the appearance of a built-in electric field. The presence of an electrostriction effect in our approach is then not sufficient to establish any link with the experimental samples, which can possibly reconstruct through different mechanisms that are not involving the presence of an electric field. The relation between experimental and first-principles results concerning the electrostriction is done in chapter 4. In chapter 5 we add some defects to the system through the modelization of a solid solution. Both works have shown that the Zener breakdown mechanism remains a plausible explanation of the experimental results on the $LaAlO_3$-$SrTiO_3$ system, despite the presence of defects in the samples.

Chapter 4

Electrostriction at the $LaAlO_3/SrTiO_3$ interface

A basic ingredient of the $LaAlO_3$-$SrTiO_3$ interface is the polarization mismatch between $LaAlO_3$ and $SrTiO_3$, that should give rise to an electric field in LAO, responsible for the Zener breakdown at a given LAO thickness. The presence of this electric field is howhever controversial and highly debated in the literature. In order to probe the existence of an electric field in $LaAlO_3$ and give credit to the polar catastrophe scenario, in this chapter we present a direct comparison between experimental data and *ab initio* calculations for the electrostrictive effect in the polar $LaAlO_3$ layer grown on $SrTiO_3$ substrates. From the structural data, a complete screening of the $LaAlO_3$ dipole field is observed for film thicknesses between 6 and 20 uc. For thinner films, an expansion of the c axis of 2% matching the theoretical predictions for an electrostrictive effect is observed experimentally, so supporting the existence of an electric field in $LaAlO_3$. The results of this chapter were published in reference [90] where the experimental results are realized by the coauthors of the paper.

4.1 Introduction

The $LaAlO_3$-$SrTiO_3$ heterostructure is a complex system in which the mechanism at the origin of the 2DEG is still very controversial. Among others, the $SrTiO_3$ could be conducting due to the creation of oxygen vacancies during the LAO film deposition. However, we have shown in chapter 3 that in a pristine system, a polar mismatch arise, leading to the appearance of a built-in electric field in $LaAlO_3$. Unfortunately, it is not

simple to measure the built-in electric field in such a system[1] and its real existence in $LaAlO_3$ is largely debated [61, 75–79]. In chapter 2, we have shown the restrictions of DFT and the difficulty to model defects, especially in a system as complex as $LaAlO_3$-$SrTiO_3$ interface. *Ab initio* calculations are simply not capable to model a system with such disorders or randomness. For these reasons, we based our approach on simpler and more basic elements of the theory: the electric field arising from the polarization mismatch between LAO and STO and its consequences on the LAO atomic structure.

In this work, we study a pristine $LaAlO_3$-$SrTiO_3$ system where the polar mismatch take place and we analyze the intrinsic consequences of the built-in electric field: a lattice expansion through the electrostrictive effect. We study the evolution of this effect before and after the Zener breakdown, giving that the field is decreasing with the film thickness. Finally, our first-principles calculations, combined with the experimental measurements, allow us to check the validity of our hypothesis: the existence of an electric field in $LaAlO_3$-$SrTiO_3$ samples. Although it does certainly not rule out the presence of additional extrinsic effects, our work support the polarization mismatch at the interface and its consequences as a plausible intrinsic origin of the 2DEG.

4.2 Theory

In chapter 3, we have shown that, in the $LaAlO_3$-$SrTiO_3$ polar-nonpolar system, a diverging potential with the LAO thickness takes place. According to the polar catastrophe scenario, the corresponding electric field through LAO (≈ 0.24 V/Å) is constant before the electronic reconstruction ($t < t_c$) and then decreases according to equation 3.3.8:

$$t < t_c \quad : \quad E^{\mathrm{LAO}} = \frac{P_0^{\mathrm{LAO}}}{\epsilon_0 \epsilon_r^{\mathrm{LAO}}} \quad , \quad t > t_c \quad : \quad E^{\mathrm{LAO}} = \frac{\Delta}{nc}, \tag{4.2.1}$$

The quantity of charges that is transferred after the critical thickness t_c is given by equation 3.3.9

$$t < t_c \quad : \quad \sigma_S = 0 \quad , \quad t > t_c \quad : \quad \sigma_S = \sigma_0 - \epsilon_0 \epsilon_r^{\mathrm{LAO}} \frac{\Delta}{nc}. \tag{4.2.2}$$

It increases as $1/t$, reaching the expected value of 0.5 e^-/S only for an infinitely large film thickness.

[1] Among other things, the metallic electrodes used for the experiments can affect the electric field [147].

The built-in electric field should affect the average lattice parameter of $LaAlO_3$ via the electrostrictive effect[2] $c = c_0 + \alpha' E^2$, rewritten with respect to the strain as:

$$\eta = \alpha E^2. \tag{4.2.3}$$

Using equation 4.2.1 and neglecting in first approximation the evolution of c ($c \approx c_m$), we can approximate the strain as:

$$t < t_c \quad : \quad \eta = \alpha \left(\frac{P_0^{\mathrm{LAO}}}{\epsilon_0 \epsilon_r^{\mathrm{LAO}}} \right)^2 \quad , \quad t > t_c \quad : \quad \eta = \frac{\alpha \Delta^2}{n^2 c_0^2}. \tag{4.2.4}$$

This predicts an expansion of the c-parameter of LAO in the $LaAlO_3$-$SrTiO_3$ system through electrostrictive effect that depends on intrinsic parameters: the LAO film thickness, the energy band gap of STO, the valence band offset and finally the dielectric constant of $LaAlO_3$.

4.3 Technical details

4.3.1 First-principles

To characterize the LAO/STO interface, we considered isolated vacuum/$(STO)_7$/$(LAO)_n$-/vacuum stacks with perfect surfaces and interfaces, made of n LAO layers (n ranging from 2 to 11) on top of 7 uc of STO. We remember the reader that a full atomic relaxations was performed, imposing the in-plane lattice constant of STO and fixing the atomic position of the first STO layer to simulate the effect of a thick substrate. Thanks to a 500 Å supercell, the slab can be considered as isolated. To check the validity of this approach, we also considered symmetric vacuum/$(LAO)_n$/$(STO)_{14}$/$(LAO)_n$/vacuum stacks and got similar results. Additional details are given in chapter 2.

The determination of the out of plane lattice parameter in $LaAlO_3$ is a key element, both theoretically and experimentally. However there is no unique way to define the c-axis parameter of LAO in the case of a relaxed LAO-STO interface due to the appearance of atomic rumpling and inhomogeneous strains within the LAO layer. It is therefore important to define properly how we extracted this parameter and also to clarify to which extent the parameter extracted from the first-principles calculations can be compared to

[2]Since $LaAlO_3$ is centro-symmetric there is no piezoelectric response allowed by symmetry.

what is measured experimentally. We considered two methods. First, the theoretical c-axis length was estimated from the average La-La distance within the film. Second, we generated the x-ray spectrum corresponding to the relaxed atomic structure obtained at the first-principles level and, then, extracted the c-axis length from this spectrum as it was done for the experimental spectra. Both methods provide similar results, clarifying that the c-axis parameter extracted from x-ray measurements can be directly compared to the average La-La distance. For the simulations with intermixing, only the second approach was used, for proper comparison with experimental data.

The charge densities σ_s were obtained by integrating the density of states of the titanium. In the case of fully compensated system i.e. with 0.5 electron transferred, this method lead to a charge of 0.45 corresponding to a precision within 10 percent.

In this work, the assumption of an ideal AlO_2-terminated LAO surface severely restricts the possible microscopic mechanisms that are available to the system for transferring charge from the surface to the interface. In particular, only Zener tunneling is possible, where holes are created at the surface and conduction electrons appear at the interface.

4.3.2 Experience

The $LaAlO_3$ films were grown on (001) TiO_2-terminated $SrTiO_3$ substrates by pulsed laser deposition at 870°C in an oxygen pressure of 10^{-4}mbar. The laser fluence was 0.6 J/cm^2 and the laser repetition rate 1 Hz. After the deposition, the films were kept at about 530°C in 0.2 bar of oxygen for 1 hour before cooling down to room temperature over one hour [148]. The growth mode and film thickness were monitored in-situ using reflection high-energy electron-diffraction (RHEED). A layer-by-layer growth mode for the LAO film was observed below a layer thickness of $\sim$ 20 u.c. Above this thickness, a progressive transition to a three dimensional growth mode was detected with a decrease of the reflected intensity due to surface roughening. The change from a streaky to a spotty RHEED pattern is clearly observed above 40 uc. As shown in figure 4.1a, atomic force microscopy (AFM) reveals atomically flat terraces separated in height by step of one unit cell up to a LAO thickness of $\sim$ 20 uc. For thicker samples, AFM reveals cracks on the surface, displayed in figure 4.1b.

As the LAO/STO interface is known to be sensitive to photodoping [32, 39, 40, 64], the variation of the two points-contact resistance for samples with thicknesses above and below the critical value has been monitored during the x-ray measurements. No effect of

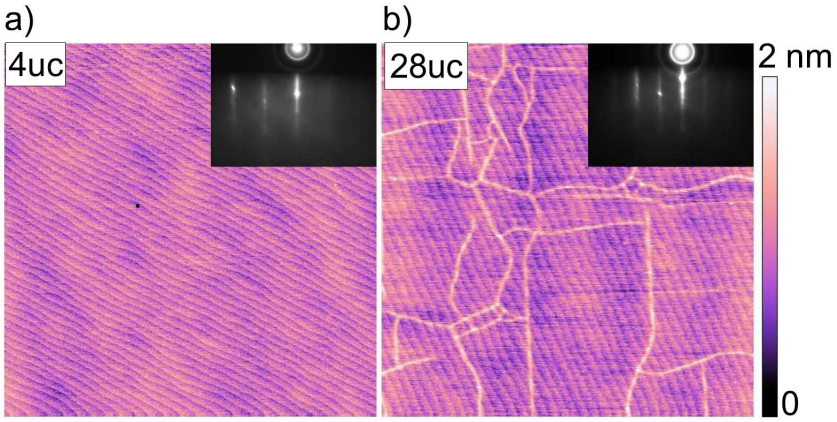

Figure 4.1: *Atomic force microscope 5×5 μm^2 topographies of a 4 uc (a) and a 28 uc (b) thick LAO film with RHEED patterns shown as inset.*

the x-ray radiation (8-15 keV) was observed on the resistance of the samples. The major contribution to the change in the resistance was given by the ambient light in the room and only for samples below the critical thickness. All the measurements discussed in this work were performed in the dark and after waiting a sufficiently long time to make the samples below the critical thickness completely insulating.

4.4 Experimental results

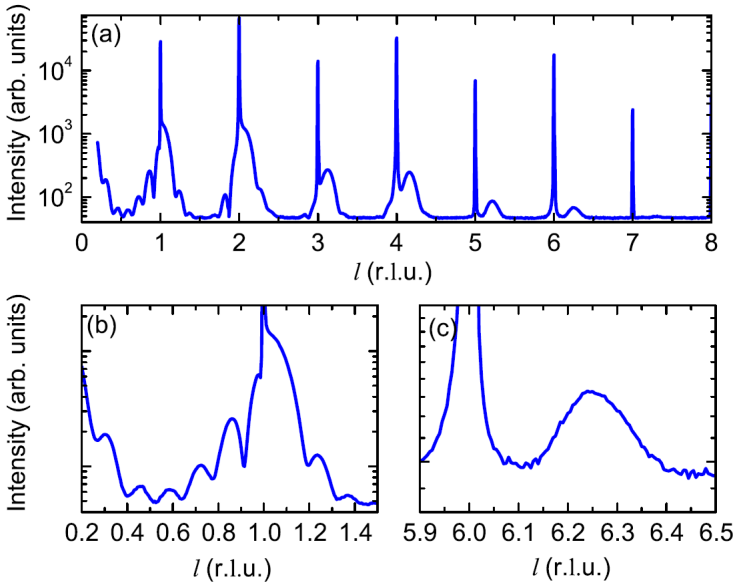

Figure 4.2: *(a) l scan along 00 crystal truncation rod of an 8-uc-thick LAO film. (b) Finite size fringes around the $l = 1$ reflection and (c) $l = 6$ LAO reflection. Reciprocal lattice units (r.l.u.) are defined by the STO reflections.*

The lattice constant of $LaAlO_3$ films were measured using x-ray diffraction performed in house and at the surface diffraction beam line of the Swiss Light Source. Figure 4.2a shows an l scan along the (00) crystal truncation rod for an 8 unit cell (uc) sample. Finite size effects (see figure 4.2b) allow the precise determination of the thickness of the LAO layer, while $00l$ reflections up to the seventh order provide accurate values for the c axis (error bars < 0.01 Å). In-plane lattice parameters were obtained from reciprocal-space maps of the $(\bar{1}\ 0\ 3)$ reflection. In figure 4.3, the measured a- and c-axis values are plotted as a function of the number of LAO unit cells. For thicknesses up to 20 uc, the in-plane a axis equals that of $SrTiO_3$, indicative that the LAO layer is perfectly strained with the STO substrate. In the same range, however, the c axis displays a complex behavior. From 2.5 to 6 uc, the c parameter decreases from 3.82 to 3.745 Å and then remains constant up to a thickness of $\sim$ 20 uc. The constant value observed from 6 to $\sim$20 uc agrees with the value c_0 expected from a purely elastic deformation imposed by the STO substrate and a Poisson ratio for LAO of 0.24 [149]. Above 20 uc the epitaxial strain is released with both in-plane and out-of-plane lattice parameters relaxing to bulk values. Analyses of the x-ray rocking curves confirm the observed relaxation. Up to 20 uc, the shape of the rocking curve is determined by the substrate. For thicker films a diffuse component is observed, a signature of dislocations [150, 151].

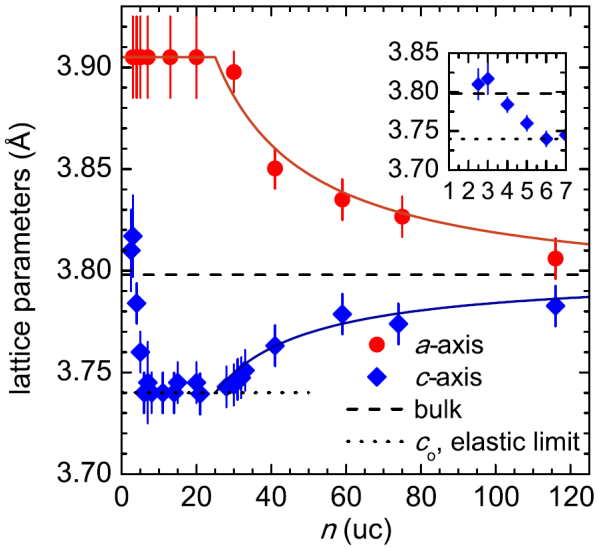

Figure 4.3: *LAO a- and c-axis parameters plotted as a function of the film thickness. The solid lines are a guide to the eye. The dashed horizontal line indicates the pseudocubic LAO bulk lattice constant. The inset shows in detail the expansion of the c axis for low LAO thicknesses.*

The large c-axis expansion observed at very low LAO thicknesses (+ 2.1% with respect

to c_0) is consistent with previous ultrahigh-resolution transmission microscopy [131] and surface x-ray diffraction data [60, 61]. These techniques access the atomic spacings across the structure and reveal that the interlayer distance in the interfacial region is anomalously high, then settles to the expected pseudomorphically strained value further up in the LAO film. These observations were related to the presence of trivalent Ti ions at the interface over typically 2-3 uc. An expanded out-of-plane lattice parameter could however also be due, as discussed below, to an electrostrictive effect expected in the presence of a large electric field. In order to quantify the magnitude of a possible electrostrictive effect, density-functional theory calculations (within the local-density approximation) were performed on bulk LAO at constrained displacement field D [152, 153]. The use of D as the independent electrical parameter is particularly convenient for our study, since it corresponds exactly to the compensating planar charge density, σ_S, that accumulates at the LAO/STO interface and, with opposite sign, at the LAO surface. The in-plane lattice parameter was fixed to the calculated equilibrium value for cubic $SrTiO_3$ to mimic epitaxial strain. As shown in figure 4.4a, LAO contains oppositely charged atomic layers, $(LaO)^+$ and $(AlO_2)^-$. This yields a "built-in" polarization $P_0^{LAO} = -e/2a^2$ [25], where a is the in-plane lattice value and e the electronic charge; conversely, in STO the built-in polarization vanishes, $P_0^{STO} = 0$. To fully compensate for this polarization discontinuity, one needs to supply an external interface charge $\sigma_S = -e/2a^2$. In this limit, $D^{LAO} = P_0^{LAO} = -e/2a^2$. This means that the internal field within LAO vanishes and the out-of-plane LAO cell parameter c_0 is determined by the elastic deformation due to the epitaxial strain. In the opposite limit (absence of compensating charges, i.e., $D^{LAO} = 0$), the mismatch between D^{LAO} and P_0^{LAO} produces a large internal field in LAO, $E = 0.24$ V/Å, consistent with an average LAO dielectric constant $\epsilon_r = 25$. This field, in turn, produces a sizable c-axis expansion of 1.7% with respect to the fully screened case value c_0 (see figure 4.4c), compatible with measurements on films of 2-3 uc (2.1%). As LAO is not a piezoelectric material, the vertical expansion must arise entirely from the electrostrictive effect. Indeed, the evolution of the c-axis strain, $\eta = (c - c_0)/c_0$, with the field is almost perfectly quadratic. The real LAO/STO system is however more complex than in this simple bulk model, and involves surface and interface effects. Also, there is no guarantee that the electrostatic response (electrostriction and dielectric constant) is identical in bulk and in ultrathin films. We thus performed additional density-functional theory calculations which are presented in the next section.

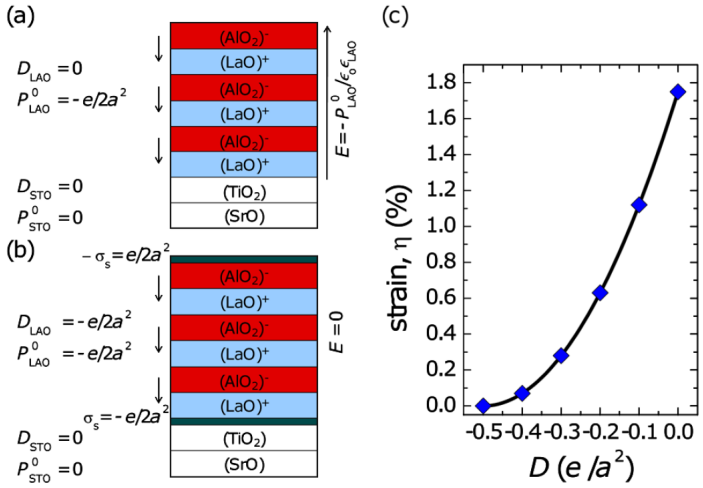

Figure 4.4: *(a-b) Schematic view of the atomic layer sequence in LAO, showing the most relevant electrical quantities in the system: "built-in" polarization P_0 (small downward-pointing arrows), electric displacement field D (D^{LAO} is equal to the interface charge σ_S), and internal electric field in LAO, E (large upward-pointing arrow). The uncompensated (a) and fully compensated (b) limits are shown. (c) Calculated electrostrictive response of LAO bulk as a function of the electric displacement field D.*

4.5 First-principles results

As previously discussed the electric field in LAO appears by construction of the polar-nonpolar LAO-STO system. First-principles calculations are then here to show that the evolution of the electric field, as predicted by the electronic reconstruction, can change the c parameter through electrostrictive effects in a way compatible with experimental results.

The evolution of the strain, the charge density of the 2DEG and the electric field obtained by first-principles calculations are represented in figure 3.9 together with experimental results. We choose to represent the strain $\eta = \frac{c-c_0}{c_0} = \alpha' E^2$ in place of the average lattice parameter to overcome small discrepancies between experimental and theoretical values. The model and first-principles results are in good agreement and a fit of the electric field with thickness, using equations. 3.3.8, gives $\Delta = 3.9$ eV, only slightly bigger than the value obtained in the band alignment, 3.77 eV. This overestimation can certainly be attributed to the macroscopic average of the field that we considered constant in all the LAO which seems to be a very good approximation. The electrostrictive effects are related to the constant $\alpha' = 0.4$ Å^2/V^2. These electrostrictive effects vanish as the field

is decreasing, giving a system similar to the supercell case for large thicknesses.

The valence-band offset between STO and LAO is equal to -0.2 eV, yielding an energy difference between the valence band of LAO and conduction band of STO of $\Delta = 3.77$ eV. This value is slightly larger than that calculated from the experimental band gaps (3.35 eV [50]) as a result of our slight overestimation of the STO band gap. The effect of the electric field is to lift the band energy of each atomic layer inside the LAO, thus reducing the energy band gap Δ.

For thicknesses $n \leq 4$, the system is insulating, and as obtained from macroscopic average techniques, the LAO layer experiences a roughly constant electric field of 0.24 V/Å (figure 4.5a), which translates into an effective dielectric constant for LAO $\epsilon_r = 25$, remarkably identical to that calculated for the bulk. This shows that bulk dielectric properties can be rapidly recovered in thin LAO films. In order to compare the theoretical predictions to experimental data, we generated the x-ray diffraction pattern associated to the relaxed theoretical atomic structure and then deduced the average lattice constant from the peak positions, exactly as it is done experimentally. For these thicknesses, the average c parameter of LAO expands to c_m, a value 2.2% larger than the calculated c_0 (3.75 Å) corresponding to a pure elastic relaxation. This expansion of the c axis is similar to that experimentally measured (2.1%) and close to that calculated for bulk LAO (1.7%).

At $n > 4$, the drop of potential across the LAO layer becomes equal to ΔE, yielding a Zener breakdown. For $n > 4$, the system becomes conducting due to a progressive transfer of electrons from the surface to the interface, ensuring the pinning of the top of the LAO valence band at the surface, at the level of the bottom of the STO conduction band at the interface[3]. Coherently with that, the electric field within the LAO layer smoothly decreases as a function of LAO thickness, according to $E^{\mathrm{LAO}} = \Delta E/nc$ as shown in figure 4.5a. Concomitantly, the two-dimensional carrier density increases, and using basic electrostatics, its evolution can be deduced from that of the field through equation 4.2.2 (figure 4.5b). In the limit of infinite LAO thickness, the internal field goes to zero for a total charge transfer of half an electron per unit cell (3.3×10^{14}e/cm^2). The average c axis parameter, illustrated in figure 4.5c, decreases progressively as the LAO layer thickness increases. As previously discussed, the amplitude of the c parameter of LAO is linked to the internal electric field within the layer through the electrostrictive

[3]As already discussed in chapter 3 the overestimation of the critical thickness is due to the overestimation of the STO band gap.

effect. Our calculations are consistent with this effect: the strain with respect to c_0 evolves with the thickness according to the reduction of the electric field, following equation 4.2.3 with $\alpha = 0.4$ Å^2 V^{-2}, comparable to the bulk calculation. The evolution of the strain with respect to the LAO film thickness is plotted in figure 4.5c. These calculations thus confirm the large electrostrictive effects predicted in the bulk for the unscreened configuration. They also predict a progressive screening of the electric field and a gradual reduction of the c axis LAO lattice parameter as the layer thickness is increased above the critical value, qualitatively similar to what is experimentally observed.

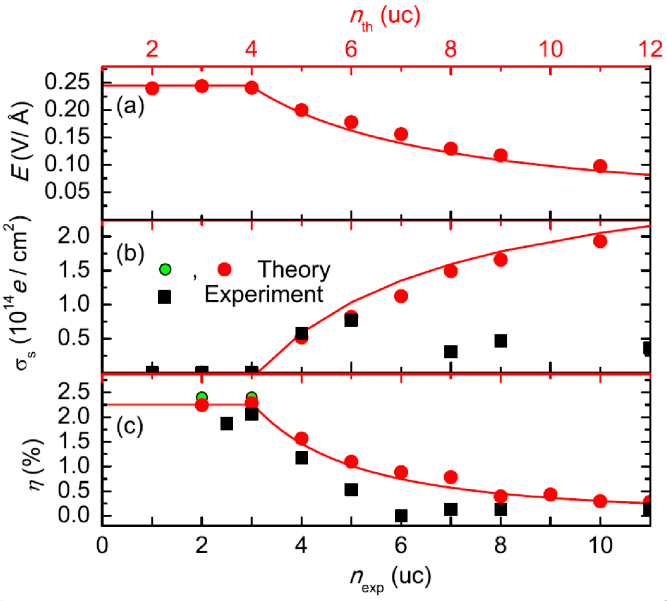

Figure 4.5: *Evolution of (a) the electric field inside the LAO layer, (b) the surface charge at the LAO/STO interface, and (c) the LAO strain with the LAO layer thickness, according to ab initio calculations (red circles) and experiments (black squares). In (a), (b), and (c) the curves joining the points are explained in the text. Two x scales are reported (top red for theory and bottom black for the experiment) to normalize at the same critical thickness (4 uc and 5 uc for experiment and theory, respectively). The green points (circled dots) show the calculated intermixed case.*

4.6 Discussion

One observes that the large c-axis expansion measured in ultrathin LAO films (2.1%) is in good agreement with the one predicted by the electrostrictive effect (2.2%) assuming a sharp LAO/STO interface. However, as similar values of the c axis have been previously related to the presence of ionic intermixing, we calculated *ab initio* the effect of La-Sr and

Al-Ti exchange at the interface. To that end, we doubled the supercell size in-plane and, within the first STO and LAO unit cells on both sides of the interface, we interchanged one Sr with one La atom and one Ti with one Al atom, producing a 2-uc-thick 50-50 intermixed region at the interface. This kind of intermixing does not bring any compensating charge to the interface. From our calculations, the breakdown LAO thickness remains unaffected and the system is insulating for $n \leq 4$. As shown in figure 4.5c, the c-axis values of LAO before breakdown stay remarkably similar to those obtained for the sharp interface. However, decoupling the electrostrictive effect and intermixing is very delicate, since the expanded c-axis parameter due to the electrostrictive effect is very similar to the one expected for an intermixed region, according to the Vegard's law. In qualitative agreement with our simulations, recent measurements at $LaAlO_3$-$SrTiO_3$ interfaces by Pauli *et al.* [61] show the coexistence of intermixing and buckling, the latter signature of a large electric field. Both intermixing and electrostriction may thus contribute to the expanded c axis. The abrupt transition of the c-axis parameter observed experimentally from 3 to 6 unit cells is faster than the progressive decay predicted from our calculations ($\eta \approx 1/n^2$, see figure 4.5c]. From 6 to ∼20 u.c., the c-axis value remains constant and equal to c_m, pointing to the absence of an internal electric field and hence to a complete screening after the breakdown ($\sigma_S = e/2a^2$). To clarify these points, we estimated the number of mobile carriers from the Hall measurements. Figure 4.5b shows (black square symbols) the two-dimensional carrier density estimated at 100 K for one-band conduction as a function of the LAO thickness[4]. Despite some scattering in the values in the metallic regime, we observe that the number of carriers is almost constant up to 11 u.c., in agreement with previous reports [32]. Its value (5×10^{13} cm^{-2}) is about an order of magnitude lower than that calculated for a complete screening (3×10^{14} cm^{-2}). This discrepancy could be due to different reasons, such as the inadequacy of the one band model for this system [154] or a large number of trapped states at the surface [53]. In any case, the structural data indicate that the electric field is screened at the interface for LAO thicknesses above 5 to 6 unit cells in agreement with recent results of Pauli *et al.* [61]. The difference between the progressive charge transfer predicted theoretically and the abrupt one observed experimentally from the structural and transport data suggests that the screening mechanism at the LAO top surface may proceed in a different

[4]Below 100 K, a reduction of the apparent carrier concentration is observed in Hall measurements and has been ascribed to carrier freeze-out or multiband conduction. We, however, notice that in both cases the charges are still present and, even if they do not contribute to the conduction, they do contribute to screening.

manner. Compensation by bound charges arising from various origins (oxygen vacancies, hydrogen adsorbates, or mixed termination) would alter the theoretical picture, removing the pinning of the Fermi level at the bottom of the LAO valence band. This means that full compensation at 4 uc is in principle possible.

4.7 Conclusion

We have presented a direct comparison between experimental data and *ab initio* calculations for the electrostrictive effect in the polar LAO layer grown on STO substrates. Our study shows that in polar materials the electrostrictive effect leads to a sizable lattice expansion which can be probed by x-ray diffraction. From the structural data, a complete screening of the LAO dipole field is observed for film thicknesses between 6 and 20 uc. For thinner films, an expansion of the c axis matching the theoretical predictions for an electrostrictive effect is observed experimentally.

Chapter 5

Tunable conductivity threshold at polar oxide interfaces

In this chapter we show that interface conductivity is also exhibited when the $LaAlO_3$ layer is diluted with $SrTiO_3$, and that the threshold thickness required to show conductivity scales inversely with the fraction of $LaAlO_3$ in this solid solution, and thereby also with the layer's formal polarization. These results can be best described in terms of the intrinsic polar-catastrophe model, hence providing the most compelling evidence, to date, in favor of this mechanism.

These results are part of reference [93]. The theoretical results, in the latter paper or in this chapter, are the results of this thesis. However, all the experimental results have been realized by the coauthors of this paper either by the group of P.R. Willmott at the Paul Scherrer institut or by the group of J.-M. Triscone at the university of Geneva.

5.1 Introduction

In a polar/non-polar system, the electric field is of a major importance given that it leads to the metal/insulator transition for a given thickness t_c. For the pristine interface, this thickness is directly linked to the formal charge associated to each (001) layers of the polar film i.e. the formal polarization. We want to study the consequences of a change of these layer formal charges on the electric field and the impact on the critical thickness. However, the system needs to be simple enough to be simulated by DFT calculations. A solid solution thin film between $LaAlO_3$ and $SrTiO_3$ is perfectly adapted to this work since it can be modeled both theoretically and experimentally. Moreover, it allows to

control the layer formal charge through the composition x of $(LaAlO_3)_x/(SrTiO_3)_{1-x}$.

In this study, we want to takle the creation of the 2DEG thanks to basic and intrinsic concepts that appears in a polar/non-polar interface. We will analyze the evolution of the metal/insulator critical thickness due to a change of the layer formal charges of the polar film. These predictions on pristine systems are then compared to experimental results on more complex samples in which several reconstruction mechanisms are enabled.

5.2 Principle

The intrinsic doping mechanism, illustrated in figure 5.1, was elegantly reformulated in the framework of the modern theory of polarization [25]: as discussed in the previous chapter, LAO has a formal polarization $P_0^{\mathrm{LAO}} = \frac{e}{2S} = 0.529$ C m^{-2} (where S is the unit-cell cross-section in the plane of the interface), whereas in nonpolar STO, $P_0^{\mathrm{STO}} = 0$. The preservation of the normal component of the electric displacement field D along the STO/LAO/vacuum stack in the absence of free charge at the surface and interface ($D = 0$) requires the appearance of a macroscopic electric field E^{LAO} the existence of which has been probed in the previous chapter. Because of the dielectric response of LAO, this field is $E^{\mathrm{LAO}} = \frac{P_0}{\epsilon_0 \epsilon_r^{\mathrm{LAO}}} = 0.24$ V/Å, where $\epsilon_r^{\mathrm{LAO}} \approx 24$ is the relative permittivity of LAO [138]. The electric field in LAO will bend the electronic bands, as illustrated in figure 5.1a. At a thickness t_c, the valence O $2p$ bands of LAO at the surface reach the level of the STO Ti $3d$ conduction bands at the interface and a Zener breakdown occurs. Above this thickness, electrons will be transferred progressively from the surface to the interface, which hence becomes metallic (figure 5.1b-d). This simple electrostatic model not only explains the conduction, but also links the formal polarization of LAO, its dielectric constant, and t_c such that

$$t_c = \frac{\epsilon_0 \epsilon_r^{\mathrm{LAO}} \Delta}{e P_0^{\mathrm{LAO}}}, \tag{5.2.1}$$

where $\Delta \approx 3.3$ eV is the difference of energy between the valence band of LAO and the conduction band of STO, and e is the electron charge. This yields an estimate of $t_c \approx 3.5$ monolayers[1] (ML), in perfect agreement with experiment [32].

Varying the composition of the LASTO:x films (that is, x) allows one to tune continuously the formal polarization such that $P_0^{\mathrm{LASTO:x}} = x P_0^{\mathrm{LAO}}$. For instance, for $x = 0.5$,

[1] Notice that here we used the experimental band gap of STO instead of the overestimated B1-WC value.

the random solid solution has alternating planes with +0.5 and -0.5 formal charges (figure 5.1e,f), compared with +1 and -1 charges in pure LAO. One must, however, also consider possible changes of the other fundamental quantities determining the critical thickness expressed in equation 5.2.1. This is part of the next section.

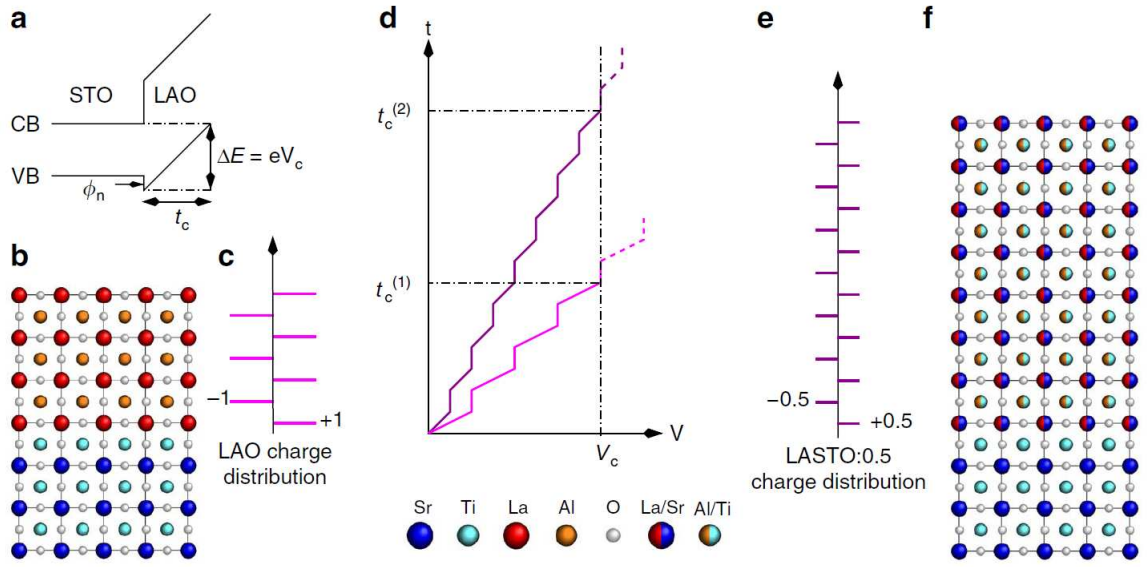

Figure 5.1: *Electrical potential build-up at polar interfaces. (a) The band-level scheme shows band bending in the pure LAO layer of the valence band (VB) and conduction band (CB), and the critical thickness t_c and potential build-up eV_c required to induce the electronic reconstruction. ϕ_n is the valence-band offset between STO and LAO. (b) LAO schematic atomic structure and (c) LAO planar charge distribution. (d) Schematic of the potential build-up as a function of its thickness t for LAO and LASTO:0.5, assuming the same relative permittivity but different formal polarizations P_0 induced by the charge of the successive A-site and B-site sublayers. The critical thicknesses for the electronic reconstruction are labelled $t_c^{(1)}$ and $t_c^{(2)}$ for LAO and LASTO:0.5, respectively. (e) LASTO:0.5 planar charge distribution and (f) schematic atomic structure. For (b) and (f), the atom legend is shown at the bottom.*

5.3 The other intrinsic parameters

5.3.1 Band gap

The energy band gap Δ formally depends on the electronic band gap of STO and the valence-band offset ϕ_n (figure 5.1) between the two materials, which can evolve with x.

In practice, however, the O $2p$ valence bands of STO and LAO ($x = 1$) are virtually aligned ($\phi_n = 0.1$ eV [53] and $\phi_n = 0.2$ eV with B1-WC) and ϕ_n further diminishes with x, so that we can confidently approximate $\Delta \approx E_g^{\mathrm{STO}}$, irrespective of the composition.

5.3.2 Dielectric constant

For pure bulk compounds in the cubic perovskite structure, the hybrid B1-WC approach yields a lattice constant and static dielectric constant for STO ($a^{\mathrm{STO}} = 3.88$ Å, $\epsilon_r^{\mathrm{STO}} = 265$) and LAO ($a_{\mathrm{LAO}} = 3.80$ Å, $\epsilon_r^{\mathrm{LAO}} = 28$), see chapter 3, in good agreement with experimental data at room temperature ($\epsilon_r^{\mathrm{STO}} \approx 300$, $\epsilon_r^{\mathrm{LAO}} \approx 24$). When the in-plane lattice constant of LAO is expanded to that of STO to accommodate the epitaxial strain, the c-parameter contracts as expected from elastic theory, yielding $c_0 = 3.75$ Å ($c_0/a = 0.97$) and the dielectric constant becomes anisotropic: $\epsilon_{zz}^{\mathrm{LAO}} = 23$, $\epsilon_{xx}^{\mathrm{LAO}} = \epsilon_{yy}^{\mathrm{LAO}} = 37$. The static dielectric constant combines a frozen-ion electronic part (that is, the optical dielectric constant ϵ^{∞}) and a relaxed-ion phonon contribution through the expression

$$\epsilon_{ij}^{\mathrm{ABO}} = \epsilon_{ij}^{\infty} + \frac{4\pi}{\Omega_0} \sum_m \frac{S_m^{ij}}{\omega_m^2}, \tag{5.3.1}$$

where the sum runs over the transverse optic modes TO_m, Ω_0 is the unit-cell volume, S_m^{ij} is the oscillator strength of mode m and ω_m^2 its frequency (Table 5.1).

Calculated dielectric constants of STO and LAO

Contribution	Mode	$SrTiO_3$		$LaAlO_3$	
		$\omega(\mathrm{cm}^{-1})$	ϵ_{STO}	$\omega(\mathrm{cm}^{-1})$	ϵ_{LAO}
Electronic			5		4
Phonons	TO_1	91	251	171	19
	TO_2	180	7	411	4
	TO_3	559	2	679	1
Total			265		28

Table 5.1: *Electronic and phonon transverse optical mode (TO_m) contributions to the static dielectric constant of $SrTiO_3$ and $LaAlO_3$, in the cubic perovskite structure at the optimized lattice constant.*

To estimate theoretically the static dielectric constant of $(LaAlO_3)_x/(SrTiO_3)_{1-x}$ solid solutions for $x = 0.5$ and $x = 0.75$, we adopted a supercell approach and considered

different atomic orderings as illustrated in figure 5.2. The in-plane lattice constant of the supercell was fixed to $a_{\mathrm{STO}} = 3.88$ Å. Periodic boundary conditions were used: the atomic positions and the out-of-plane lattice parameter c (along z) were relaxed and the electronic and phonon contributions to the dielectric constant were computed. For $x = 0.5$, four different atomic arrangements, compatible with a 20-atom-supercell, were considered (figure 5.2). The "checkerboard" (CB) configuration corresponds to the case in which Al and Ti atoms at the B site, and La and Sr atoms at the A site, are perfectly alternating along the three Cartesian directions of the cubic perovskite unit cell; it is the atomic configuration most representative of a perfect mixing achievable within the chosen supercell. The "chain" configurations then preserve Ti and Al chains (for C1) and Ti and Al and Sr and La chains (for C2) along the z direction; these configurations mimic arrangements in which columns of STO and LAO are in parallel. Finally, the "planar" configuration (P1) corresponds to a STO/LAO 1/1 superlattice in which STO and LAO planes alternate along the z direction, and therefore corresponds to having STO and LAO in series.

In all cases, the static dielectric constant along z remains close to that of LAO under the same strain conditions ($\epsilon_r^{\mathrm{LAO}} = 23$). In the CB configuration, we obtain $\epsilon_r^{\mathrm{LASTO:0.5}} = 27$. For the P1 arrangement, we also nearly recover the dielectric constant of LAO, as expected when putting LAO and STO in series, while the dielectric constant increases for C1 and C2, as expected when placing them in parallel. All these results are compatible with the fact that the large dielectric constant of STO arises from the contribution of the low-frequency ferroelectric mode, which requires a correlation of the atomic displacement along Ti-O chains, which is suppressed by atomic disorder. The C1 and C2 orderings exhibit the highest dielectric constants and have the highest energies; these are, therefore, unlikely to appear spontaneously. The energetically most stable configuration is P1. However, as the growth is not at thermodynamic equilibrium and there is no experimental evidence from X-ray diffraction of any kind of spontaneous superlattice ordering, we consider the theoretical configuration most representative of the experimentally grown system to be the CB ordering, which exhibits a static dielectric constant nearly equal to that of LAO. We notice that averaging over the different orderings would still produce a dielectric constant close to that of LAO. This conclusion is further confirmed experimentally.

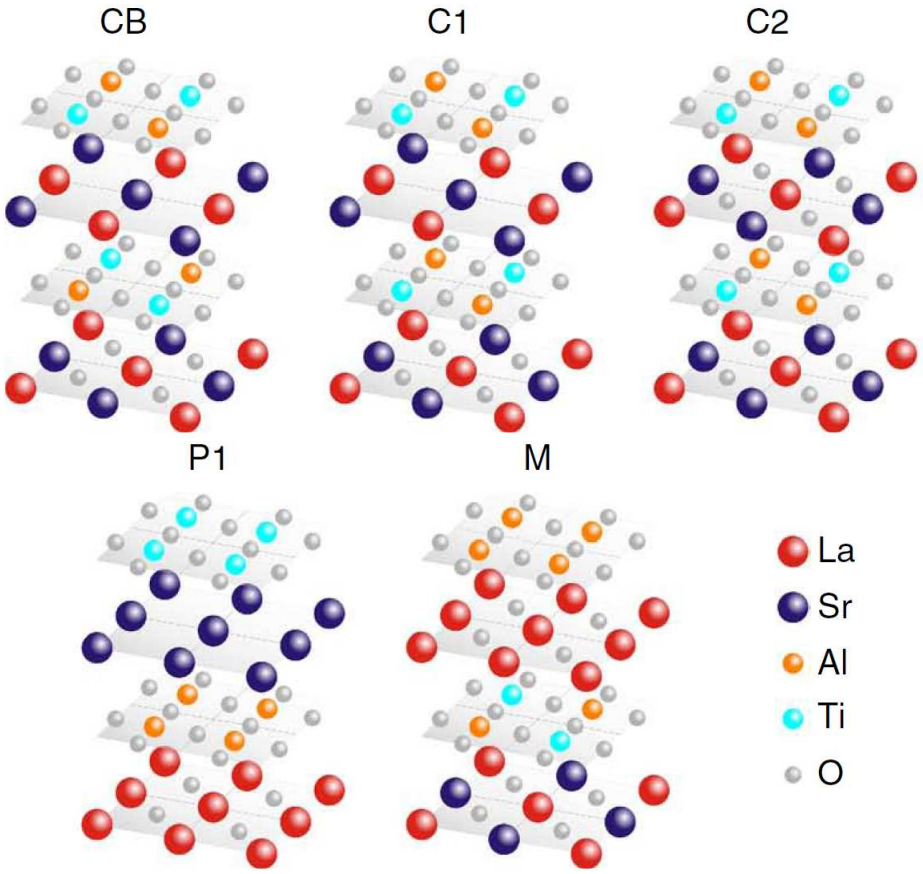

Figure 5.2: *$(LaAlO3)_x(SrTiO3)_{1-x}$ atomic configurations simulated by first-principles calculations. Four configurations for $x = 0.5$ and one for $x = 0.75$ were considered. The static dielectric constant along z, $\epsilon_{zz}^{\mathrm{LASTO}}$, and the difference of energy Δ (in eV/f.u. of 5 atoms) with respect to the reference energy $E^{\mathrm{ref}} = xE^{\mathrm{LAO}} + (1-x)E^{\mathrm{STO}}$ corresponding to the sum of the individual energy of bulk LAO and STO in the same strain conditions, are summarized in table 5.2.*

Calculated dielectric constants

Model	x	$\epsilon_{zz}^{\mathrm{LASTO}}$	ΔE
CB	0.5	27	0.055
C1	0.5	34	0.131
C2	0.5	52	0.077
P1	0.5	32	0.028
M	0.75	26	0.020

Table 5.2: *Four investigated models for x=0.5 and one model for x=0.75 are considered.*

5.4 First-principles results

Hence, from the discussion above, it seems that varying the composition of the LASTO:x films ($0.5 \leq \mathrm{x} < 1$) allows one to tune the formal polarization while keeping the other quantities in equation 5.2.1 essentially constant, that is,

$$t_c^{\mathrm{LASTO:x}} = t_c^{\mathrm{LAO}}/x \tag{5.4.1}$$

On the basis of these findings, we subsequently modelled STO/(LASTO:0.5)$_m$/vacuum stacks, considering the CB atomic arrangement. First, before breakdown, the computed electric field within LASTO:0.5 is equal to about 0.1 V/Å, roughly half that observed in pure LAO (0.24 V/Å) and consistent with the fact that the dielectric constant remains approximately the same, whereas the formal polarization is half that of pure LAO. The average lattice constant within LASTO:0.5 is equal to 3.84 Å, slightly larger than the value of 3.81 Å for CB bulk LASTO:0.5 in the same strain conditions, consistent with the electrostrictive effect. This value is comparable to what is measured experimentally. Increasing m, the first-principles calculations predict that the system becomes metallic for m between 6 and 7, in perfect agreement with the polar catastrophe scenario and the experimental measurements. For $x = 0.75$, we considered the atomic arrangement of configuration M in figure 5.2, that corresponds to a checkerboard arrangement in plane. Here again the static dielectric constant of the alloy remains essentially equal to that of LAO: $\epsilon_r^{\mathrm{LASTO:0.75}} = 26$. Using the model of the electronic reconstruction we therefore predict that $t_c = 7$ ML and 5 ML for $x = 0.5$ and 0.75, respectively, a result confirmed for $x = 0.50$ from first-principles calculations.

5.5 Experimental results

The crystallographic quality of the films is shown in figure 5.3. Growth was layer-by-layer, as also seen from clear RHEED oscillations and the atomic flatness observed in atomic-force micrographs. All films were perfectly strained. The out-of-plane lattice constant of the LASTO:0.5 films was determined to be 3.83 ± 0.01 Å, in agreement with *ab initio* calculations for strained growth on STO (the pseudocubic lattice parameter of the bulk pulsed laser-deposition (PLD) target was 3.85 ± 0.01 Å). No evidence could be found either in plane or out of plane from superstructure peaks that there was any spontaneous ordering of the cations, at least for superstructures with a periodicity an even multiple

of that of the normal unit cell. Neither of the mixed-composition film stoichiometries

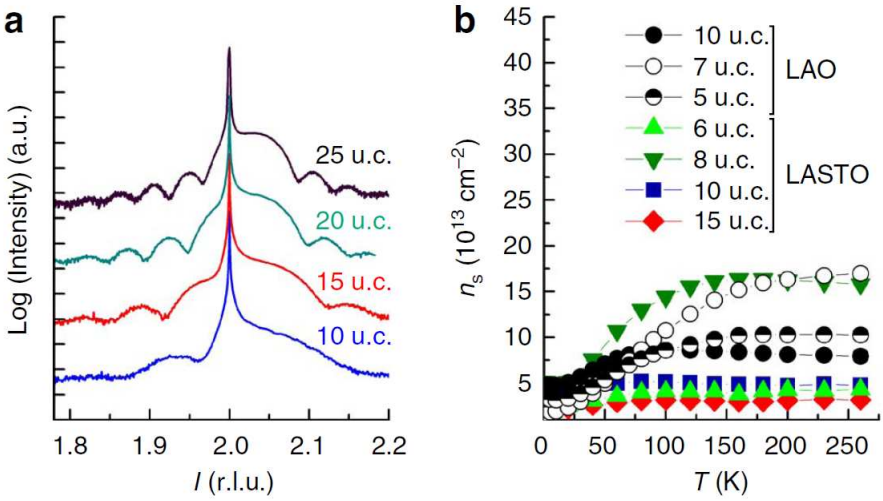

Figure 5.3: *(a) X-ray diffraction patterns recorded as a function of reciprocal lattice units (r.l.u.) around the (002) peaks of the STO substrate (sharp feature) and the LASTO:0.5 films, for different film thicknesses. (b) Sheet carrier density as a function of temperature and film thickness for pure LAO and LASTO:0.5.*

investigated produce layers that increase in conductance with thickness, as one might otherwise expect for intermixed materials that were intrinsically electrically conducting. In addition, none of the films are conducting at the top surface, but instead require careful bonding at the interface to exhibit conductivity. These metallic interfaces were characterized for their transport properties using the van der Pauw method. All samples remained metallic down to the lowest measured temperature of 1.5 K. The sheet carrier densities n_s are in the range 3 to 15×10^{13} cm^{-2}, although with no obvious dependence on composition or thickness of the layers (figure 5.3b).

According to the polar-catastrophe model, we should expect LASTO:x samples to exhibit a lower carrier density, as the screening charge scales as $x.\,e/2S$, whereby S is the unit-cell surface area. However, as already observed for LAO/STO interfaces, the estimation of the carrier density from the Hall effect yields values up to one order of magnitude smaller than those predicted from theory, possibly suggesting a large amount of trapped interface charges [58]. This can explain the known scattering of data from one sample to another, irrespective of composition or layer thickness, and precludes the possibility of testing the polar-catastrophe scenario simply from inspection of n_s. The Hall mobility μ ($\sim$ 500 cm^2 V^{-1} s^{-1} at 1.5 K) and sheet resistance ($\sim$5-20 k$\Omega/\square$ at room temperature) of the LASTO:x interfaces measured as a function of temperature exhibit essentially the same dependence as those for the interfaces with pure LAO films [149] . To probe exper-

imentally the dielectric constant, capacitors were fabricated with different thicknesses of pure LAO and the $x = 0.5$ films, using palladium as the top electrode. A serious complication in measurements of such ultrathin films is the significant contribution of the electrode-oxide interface on the capacitance [155], which means that the results can only be viewed semi-quantitatively. We observe that the dielectric constants of the LASTO:0.5 and LAO display values in the range of 20 to 30, and are in good agreement with previous reports on ceramic solid-state solutions, where no large enhancement of the relative permittivity was observed for the solid solution up to 80% STO [156]. Measurements of the temperature dependence and the electric-field tunability confirm that LASTO:x behaves like LAO rather than STO. Cooling the films to 4 K produces a small change of the dielectric constant, in sharp contrast with the low-temperature divergence of STO. These experimental results show that there is no large enhancement of the dielectric constant in LASTO:0.5 with respect to pure LAO, as predicted by our first-principles calculations.

Figure 5.4 is the central result of this work. The conductance of the interface as a function of the LASTO:x film thickness is shown for $x = 0.5$ (figure 5.4a), $x = 0.75$ (figure 5.4b), and $x = 1$ (pure LAO, figure 5.4c). The conductivity is given in conductance (left axis) and/or sheet conductance (right axis). The step in conductance for $x = 1$ is observed between 3 and 4 unit cells, as first observed by Thiel *et al.*. [32] and reproduced by several groups. For $x = 0.75$ and 0.50, the data unambiguously demonstrate that the critical thickness increases with STO-content in the solid solution, with $t_c^{\text{LASTO:0.75}}$ close to 5 unit cells, and $t_c^{\text{LASTO:0.5}}$ between 6 and 7 unit cells.

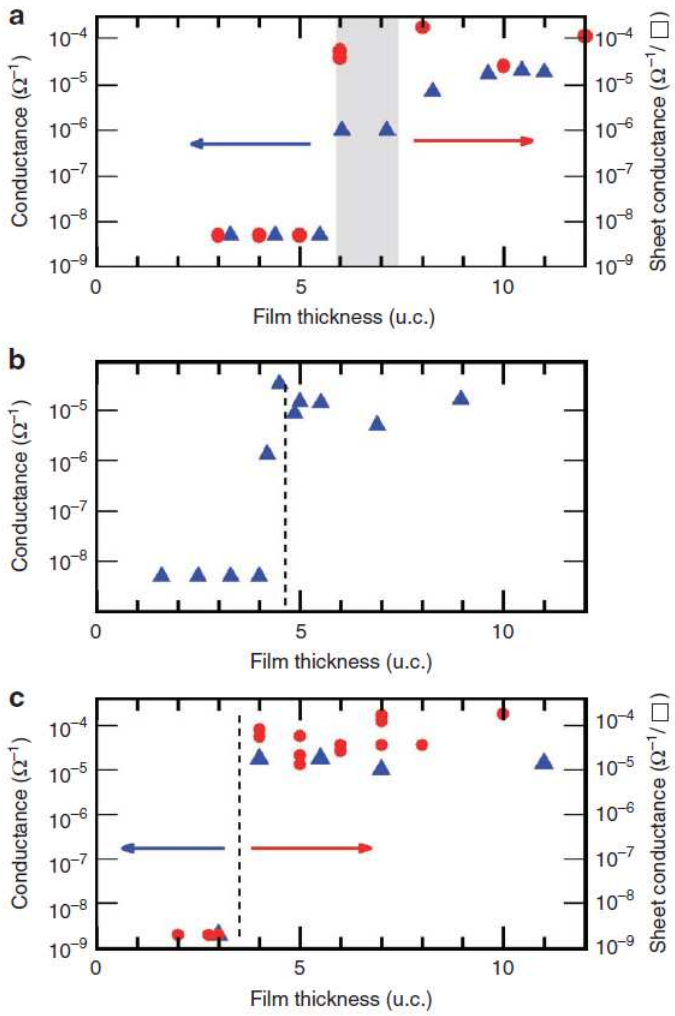

Figure 5.4: *Dependence of the conductivity threshold thickness on film composition. Room-temperature conductance of LASTO:x films for (a) $x = 0.50$, (b) $x = 0.75$, and (c) $x = 1$. The dashed vertical lines for $x = 1.0$ and 0.75 indicate the experimentally determined threshold thicknesses t_c, which for $x = 0.5$, is represented by a band for the more gradual transition. All values were obtained after ensuring that the samples had remained in dark conditions for a sufficiently long time to avoid any photoelectric contributions. The blue triangles are samples belonging to the first set, and red points denote samples from second set.*

5.6 Discussion

The striking result shown in figure 5.4 demonstrates that the critical thickness depends on x, increasing as the formal polarization decreases. The thresholds in conductivity obtained from the experimental data are only very marginally smaller than predicted by

theory, which can easily be attributed to the uncertainty in the dielectric constants of the solid solutions. The overall agreement, however, with the predictions of the intrinsic polar-catastrophe model described by equation 5.2.1 is remarkable. In contrast, it is difficult, or, at least, it demands a significantly more complex model, to explain the observed dependence of the threshold thickness with x in terms of the extrinsic phenomena of interfacial intermixing or oxygen vacancies. It would require that the "correct" composition to provide conductivity is only achieved at the interface, regardless of the film composition, and that this stoichiometry is obtained only after depositing a film thickness that does depend on x. We can envisage no such scenario explained by intermixing or oxygen vacancies. Using the principle of Occam's razor, we therefore consider both extrinsic mechanisms to be far less plausible candidates.

5.7 Conclusion

In conclusion, we have shown that, in heterostructures of ultrathin films of the solid solution $(LaAlO_3)_x/(SrTiO_3)_{1-x}$ grown on (001) $SrTiO_3$, the critical thickness, at which conductivity is observed, scales with the strength of the built-in electric field of the polar material. These results test the fundamental predictions of the polar-catastrophe scenario and provide compelling evidence in favour of the intrinsic origin of the doping at the LAO/STO interface.

Chapter 6

Spontaneous 2-Dimensional Carrier Confinement at the n-Type $SrTiO_3/LaAlO_3$ Interface

In this chapter we describe the confinement of the two-dimensional electron gas at the n-type $SrTiO_3/LaAlO_3$ interface, as a function of the sheet carrier density n_s via advanced first-principles calculations. Electrons localize spontaneously in Ti $3d_{xy}$ levels within a thin ($\lesssim$ 2 nm) interface-adjacent $SrTiO_3$ region for n_s lower than a threshold value $n_c = 10^{14}$ cm^{-2}. For $n_s > n_c$ a portion of charge flows into Ti $3d_{xz} - d_{yz}$ levels extending farther from the interface. This intrinsic confinement can be attributed to the interface-induced symmetry breaking and localized nature of Ti $3d$ t_{2g} states. The sheet carrier density directly controls the binding energy and the spatial extension of the conductive region. A direct, quantitative relation of these quantities with n_s is provided. These results were published in reference [94]. The pSIC calculations have been realized by the coauthors of this work.

6.1 Introduction

The previous chapters were dedicated to a general description of the $LaAlO_3$-$SrTiO_3$ system (chapter 3) and the possible mechanisms at the origin of the 2DEG at the n-type interface (chapter 4 and 5). The last part of this work is devoted to the properties of the 2DEG. For instance the two-dimensional nature of the gas was only proved in 2010 thanks to Shubnikov-de Haas experiments [154] and this gas is different to what is found

at conventional semiconductor interfaces [46, 157]: extremely small thickness ($\sim$ nm rather than $\sim \mu$m), large binding energies (tenths of eV rather than meV), and correlated nature of the carriers (as opposed to nearly free carriers), better described through the concept of two-dimensional electron liquid (2DEL). The $LaAlO_3$-$SrTiO_3$ heterostructure presents some new and rich physics as expected by tuning the degrees of freedom in oxides materials. In addition the high correlation of the Ti $3d$ electrons tend to make this system even more exciting with properties that are far from the usual "free electrons" behavior at the semiconductor interfaces. For that reason it is mandatory to investigate these new properties and to describe and explain the new possibilities of such systems that are an opportunity for electronics [5].

While previous theoretical works were based on conventional LDA/GGA [53, 54, 141, 144, 158–160] or parameter-dependent LDA+U [52, 143, 161–163], here we apply two advanced density functional theory-based methods which provide an improved description of strongly correlated materials: the pseudo self-interaction corrected local-density functional (pSIC) [164], and the hybrid Fock-exchange plus Wu-Cohen GGA functional (B1-WC) [114] as already used in the previous chapters. Their performance for correlated oxides is demonstrated by many previous applications [114, 164, 165] and the correct description of bulk STO and LAO electronic structures.

In this chapter we demonstrate, based on advanced first-principles calculations appropriate for correlated systems, that the formation of the 2DEL can be explained by purely intrinsic mechanisms activated by the localized nature of Ti $3d$ t_{2g} carriers. In addition we will show the impact of this orbital occupancy on the geometrical structure, through buckling and rumpling, an effect that was experimentally observed by Pauli *et al.* [61].

6.1.1 Orbitals splitting: a general case

The free Ti atom is formed of 22 electrons with the 4 latest that start to fill the five $3d$ orbitals. The $3d$ states are energetically degenerated in the free or spherical environment, see figure 6.1a. In $Sr^{2+}Ti^{4+}O_3^{2-}$, the Ti can be considered at the center of the cubic structure, and forming bondings with the O at the face center. Even if the three spatial directions are identical, the five $3d$ orbitals have different orientations and the Coulomb repulsions depend on the direction which is considered. Indeed, the electrons in O^{2-} are not at the same distances to all the $3d$ orbitals of Ti due to the octahedral symmetry.

◦ 3 orbitals are pointing between 2 oxygen atoms: d_{xy}, d_{xz} and d_{yz}. An electron in one

of these orbitals would experience a smaller electrostatic repulsion from the O^{2-} due to a larger distance. These 3 equivalent orbitals are collectively referred to as t_{2g} and are stabilized.

$\rightsquigarrow$ 2 orbitals are pointing toward oxygen atoms: d_{z^2} and $d_{x^2-y^2}$. An electron in one of these orbitals would experience a larger electrostatic repulsion from the O^{2-} due to a smaller distance. These 2 equivalent orbitals are collectively referred to as e_g and are destabilized.

The resulting picture is represented in figure 6.1b where 1 set of 5 degenerated orbitals changes to 2 sets of 3 and 2 degenerated orbitals. This description corresponds to an ideal and infinite system in all 3 directions, as in the bulk. In a real substrate, however, the previous description is only a valid approximation thanks to the size of the sample. Indeed the surface represents only a very small fraction of the system and is usually neglected[1]. For example in a 1 mm thick substrate there is only few layers close to the surface while $\sim 4 \times 10^6$ layers composes the sample.

In $Sr^{2+}Ti^{4+}O^{2-}$ the $3d$ orbitals are empty and if the system is doped, according to crystal field effect, the electrons rely in the t_{2g} orbitals. However, the Ti $3d$ orbitals do not have the same resulting properties and for instance can differ by their mobilities or their effective masses. Know in which t_{2g} orbitals the electrons rely is thus important when considering electronic properties. Nevertheless, in $LaAlO_3$-$SrTiO_3$ heterostructures additional symmetries are broken and a new splitting of orbitals can emerges compare to the octahedral symmetry represented in figure 6.1b.

6.1.2 Orbitals splitting: the LAO-STO case

The $LaAlO_3$-$SrTiO_3$ system is much more different due to the thin $LaAlO_3$ film on top of the substrate, meaning that surface and interfacial effects cannot be neglected in LAO. In addition, for $SrTiO_3$ the layers close to the interface experience a totally new environment due to the $LaAlO_3$ film, far from being bulk-like. More generally, all the directions are no longer equivalent. Parallel to the interface, i.e. in x and y directions, the system consist of repeating units in a large range, so surface effects can be neglected[2]. On the

[1] In fact the orbitals of the surfacial atoms can be modified and are forming surface bands. Such bands actually appear in our systems and will be discussed in a later section.

[2] In fact, due to the boundary condition, there is no surface at all in the calculations in these 2 directions.

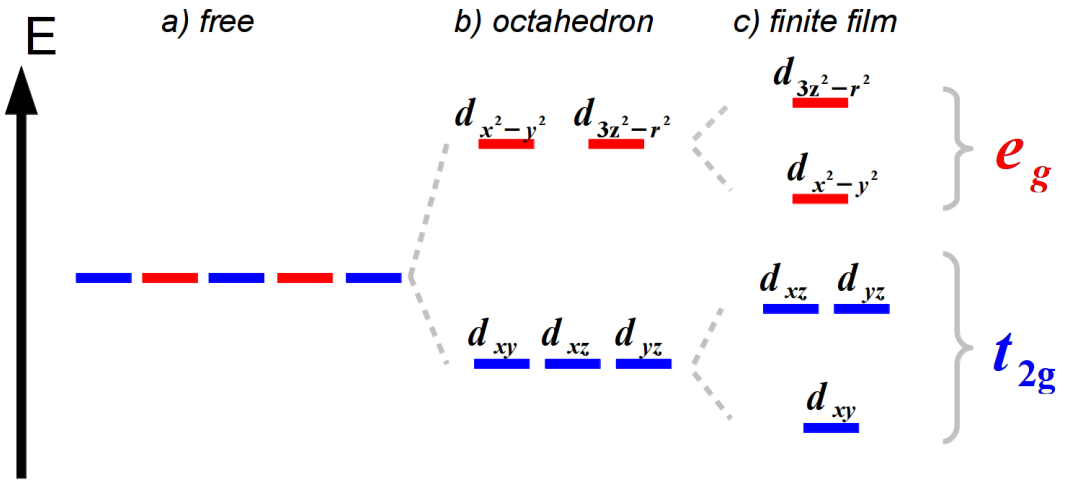

Figure 6.1: *a) The 5 Ti 3d degenerated states in the free environment. b) t_{2g} and e_g states of the octahedron symmetry. c) Additional splitting in the finite thin film.*

other hand, perpendicular to the interface, z direction, the environment suddenly changes when the interface ($SrTiO_3 \rightarrow LaAlO_3$) or the surface ($LaAlO_3 \rightarrow$ vacuum) is crossed. The z direction is no more equivalent to the two others, x and y. As consequence, in $LaAlO_3$-$SrTiO_3$ the t_{2g} orbitals in $SrTiO_3$ are split in a singlet d_{xy} and a doublet d_{yz} and d_{xz} as represented in figure 6.1c. However the orbital ordering in t_{2g} or e_g is not trivial to predict.

The band structures using B1-WC calculation of a vacuum/$(SrTiO_3)_4$/$(LaAlO_3)_2$/vacuum stack and on $SrTiO_3$ bulk are represented in figure 6.2b and 6.2a respectively. For the latter, the t_{2g} orbitals are degenerated at Γ point and the e_g orbitals are higher in energy as expected by the crystal field theory. The band structure of the slab is more complicated. First, the crystal field splits the $3d$ states. Secondly, symmetry breaking due to the interface splits the t_{2g} states in a lower d_{xy} singlet and an upper d_{xz}, d_{yz} doublet, inducing the preferential filling of the former, in agreement with measurements by x-ray spectroscopy [47]. In addition, the Ti atoms of different layers experience not equal electrostatic field due to various distances to the interface. For that reason, Ti in different layers are not equivalent anymore and several bands, corresponding to the number of TiO_2 layers in the system, are formed for each orbitals. For thicknesses smaller than t_c, the system is insulating and all the Ti $3d$ orbitals are above the Fermi level. When $SrTiO_3$ is doped, electrons start to fill these orbitals that are shifted below the Fermi level. Two questions are coming to mind here. First is, how the orbital occupancies and the properties of these bands evolves with the charge densities? Second is, how the shift of the bands evolves with the $LaAlO_3$ thicknesses or the carrier density (rigidly or not)

and what are the consequences? These two questions are at the center of the present chapter (or [94]) and the work in reference [166] (not presented in this thesis).

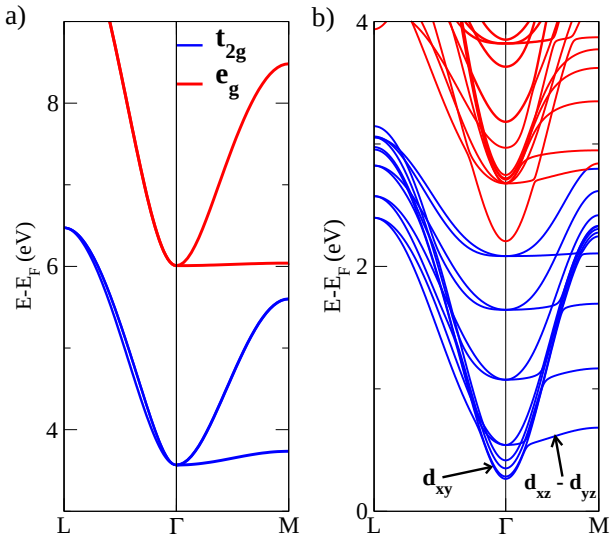

Figure 6.2: *a) The Ti 3d bands for STO in bulk. In Γ the t_{2g} orbitals are degenerated and lower in energy compare to e_g orbitals. b) The Ti 3d bands for STO in a two-dimensional slab. At Γ point the t_{2g} and e_g orbitals are split due to surfacial (or interfacial) effects. Each band is multiplied by the number of Ti atom in the system and are not at identical energy anymore. However generally a band does not correspond to a specific Ti.*

6.2 Orbital occupancy

6.2.1 Electron confinement

To describe the orbital occupancy in the $LaAlO_3$-$SrTiO_3$ system, we model the ideal and fully compensated (doped by 0.5 e^-/S) STO/LAO interface by a symmetric superlattice with two identical TiO_2/LaO interfaces (see section 2.4.2). The half-electron redistribution near the interface is illustrated in figure 6.3a, which reports the pSIC calculated layer and orbital projected Ti t_{2g} density of states in a small energy window near the STO conduction band bottom (the B1-WC results for the DOS, not displayed here, are quite similar[3]). The corresponding band energies and Fermi surfaces, discussed later on, are reported in figures 6.4a and 6.4c, respectively. As described in the introduction, the interface crystal field splits the t_{2g} states in a lower d_{xy} singlet, and an upper d_{xz}, d_{yz}

[3]We present here the results as they were in the original paper.

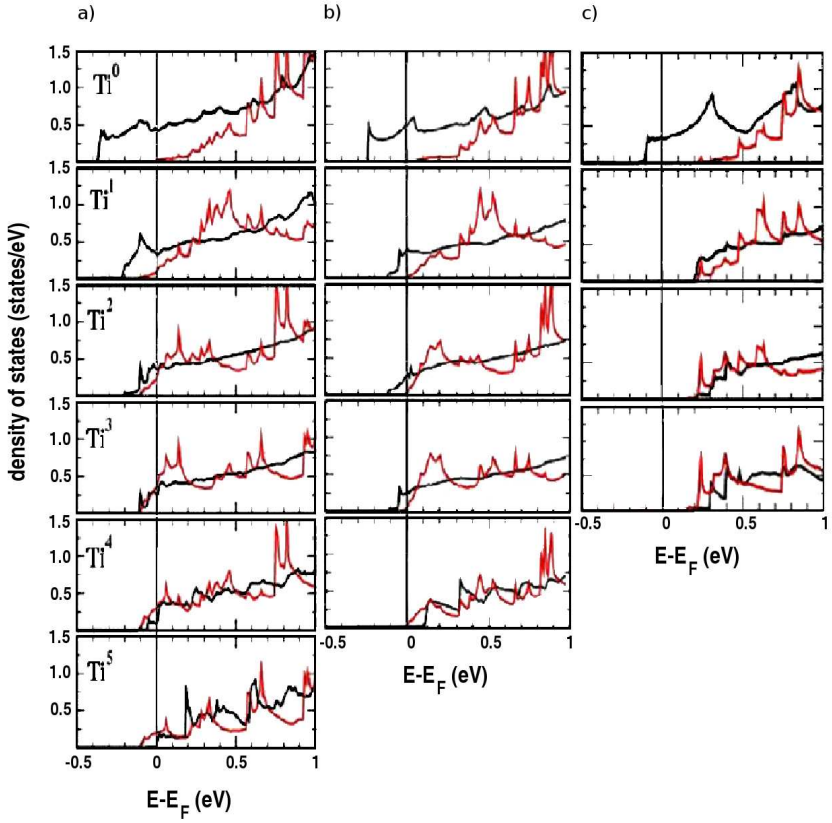

Figure 6.3: *Layer-projected and orbital-resolved density of states of the Ti 3d t_{2g} orbitals in the symmetric STO/LAO supercell calculated by pSIC. Black lines: d_{xy} singlet; red lines: (d_{xz}, d_{yz}) doublet; panels (a), (b), and (c) refer, respectively, to $n_s = 0.5$ e^-/S (i.e., 3.3 × 10^{14} cm^{-2}), 0.15 e^-/S (10^{14} cm^{-2}), and 0.03 e^-/S (0.2 × 10^{14} cm^{-2}). Ti^0 is the Ti atom at the interface, Ti^i the Ti atom of the ith layer below it. The e_g submanifold is empty and well above this energy range.*

doublet inducing the preferential filling of the former, in agreement with measurements by x-ray spectroscopy [47] (see the corresponding band splitting in figure 6.4a). Table 6.1 reports the (very consistent) B1-WC and pSIC values of singlet and doublet occupations in each STO layer: a large charge fraction (0.15 e^-/S) sits in the d_{xy} state right at the interface (Ti^0); a much smaller and steadily decreasing portion also exists in the Ti^i d_{xy} states up to layer $i = 4$, until on Ti^5 no more d_{xy} charge is found. On the other hand, starting from Ti^1 a minor portion of charge is carried by interface orthogonal d_{xz} and d_{yz} orbitals. This contribution, spread over a thicker STO region, survives beyond the sixth Ti layer below the interface. Concurrently, the singlet-doublet splitting decreases from ~ 0.37 eV for Ti^0 (0.4 eV according to B1-WC) to 0 at Ti^3, and then changes sign at Ti^4 as the singlet shifts above the doublet.

Calculated orbital occupancy						
	d_{xy}		$d_{xz}+d_{yz}$		t_{2g}	
Ti0	0.15	(0.15)	0	(0)	0.15	(0.15)
Ti1	0.09	(0.09)	0.01	(0.01)	0.10	(0.10)
Ti2	0.06	(0.05)	0.03	(0.02)	0.09	(0.07)
Ti3	0.04	(0.04)	0.05	(0.04)	0.09	(0.08)
Ti4	0	(0.01)	0.04	(0.05)	0.04	(0.06)
Ti5	0	(0)	0.02	(0.02)	0.02	(0.02)
total	0.34	(0.34)	0.15	(0.14)	0.49	(0.48)

Table 6.1: *Orbital decomposition of the 0.5 electron charge on the STO side of the fully compensated n-type TiO_2/LaO interface calculated by pSIC and B1-WC (in parentheses). The TiO_2 layer labeled "Ti^5" is the farthest from the interface.*

The 0.5 e^-/S (i.e., 3.3×10^{14} cm^{-2}) limit fixed by the polar catastrophe model is actually never reached in Hall measurements, which typically report n_s between 10^{13} cm^{-2} and 10^{14} cm^{-2}, depending on sample condition and preparation. This motivated us to investigate the 2DEL properties at lower charge carrier concentration. Thus, using the same structure, we fix n_s at two typical values: 10^{14} cm^{-2} (0.15 e^-/S) [46], and 0.2×10^{14} cm^{-2} (0.03 e^-/S) [40]. At $n_s = 10^{14}$ cm^{-2} [see the corresponding DOS and band energies in figure 6.3b and figure 6.4b, respectively] E_F crosses four d_{xy} bands of the first four Ti atoms from interface, running just below the bottom of the doublet band manifold, which remains unoccupied. Thus, the charge is entirely localized within the first 1.5-2 nm from the interface and is exclusively of d_{xy} orbital character. Clearly, even a tiny increase of E_F would produce a charge spillout into the doublet states. The binding energy (i.e., the difference between the conduction band bottom at the interface and in the inner side of the slab) is 0.25 eV, thus quite smaller than the 0.37 eV for $n_s = 0.5$ e^-/S, and consistent with the experimental value of 0.25 ± 0.07 eV [43]. In the very low-concentration case (see the DOS in figure 6.3c) all the charge is entirely localized on the Ti^0 d_{xy} orbital, and the binding energy is about 0.2 eV. Our analysis reveals a moderately correlated nature of the confined charge: the energy splitting at the interface between d_{xy} and d_{xz}, d_{yz} directly controls the confinement extension. Standard LDA/GGA underestimates the splitting due to the poor treatment of the on-site Coulomb repulsion, while B1-WC and PSIC, appropriate for correlated electrons, restore the correct behavior[4]. We have

[4]LDA predicts an interface singlet-doublet splitting significantly (∼ 50%) smaller, and a localization

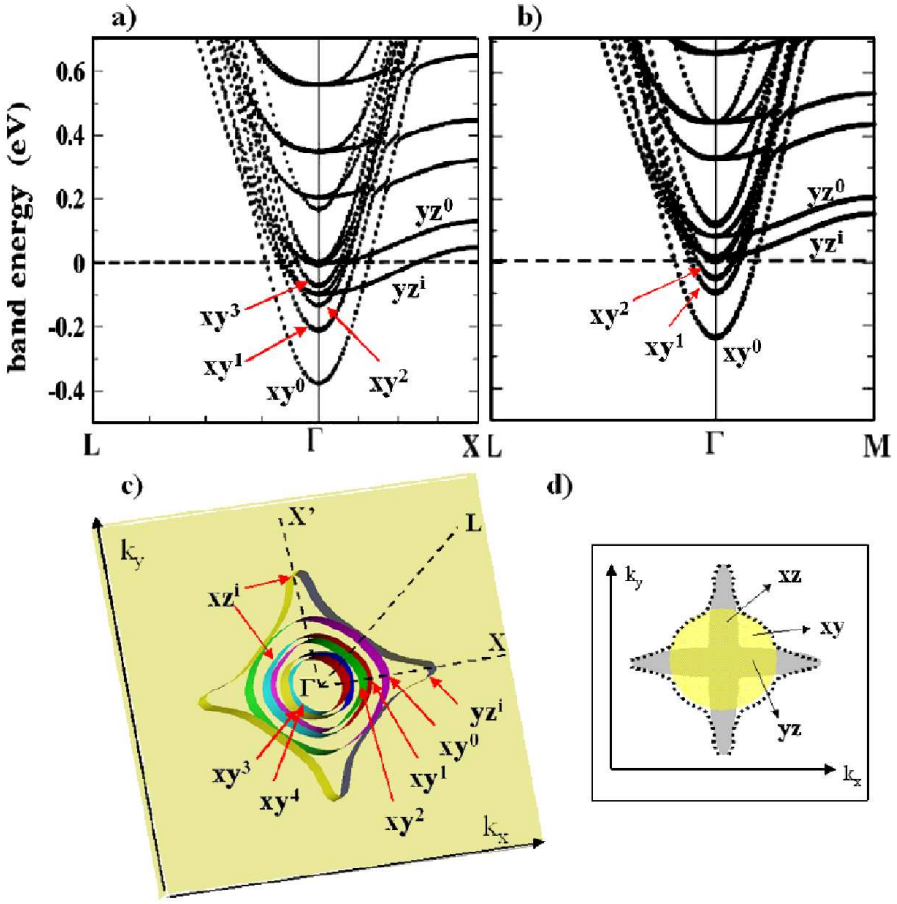

Figure 6.4: *Top: pSIC-calculated band energies for (a) $n_s = 0.5$ e^-/S (3.3×10^{14} cm^{-2}), and (b) $n_s = 0.15$ e^-/S (10^{14} cm^{-2}). Bottom: Panel (c) calculated Fermi surfaces for $n_s = 0.5$ e^-/S in the 1×1 Brillouin zone of edge $2\pi/a_{STO}$; labels identify the dominant t_{2g} orbital character and the TiO_2 layer they belong to (same notations as in figure 6.3); notice that xz^i, yz^i, with $i \leq 1$ label the (nearly degenerate) occupied doublet orbitals located on Ti^1, Ti^2, etc. Panel (d) sketch of the calculated extremal Fermi surfaces (dotted black line) divided up into three contributions, the circular xy^0 and two cigar-shaped xz^i and yz^i bands.*

estimated the contribution to the singlet-doublet splitting due to the on-site Coulomb repulsion to be ~ 0.2 eV at the interface layer for the $n_s = 0.5$ e$^-$/S case. This confining mechanism is fully consistent with that envisioned in reference [5, 157], and it holds in general for both LAO films grown on STO or STO/LAO multilayers, irrespective of the presence or absence of built-in electric field in LAO (as confirmed by B1-WC calculations on isolated STO/LAO/vacuum stacks of various LAO thicknesses presented in chapter 3). Figure 6.5 summarizes the interface band lineup, charge profile, and binding energies

length slightly longer than in our approach. See, e.g., W.-j. Son *et al.* [51]

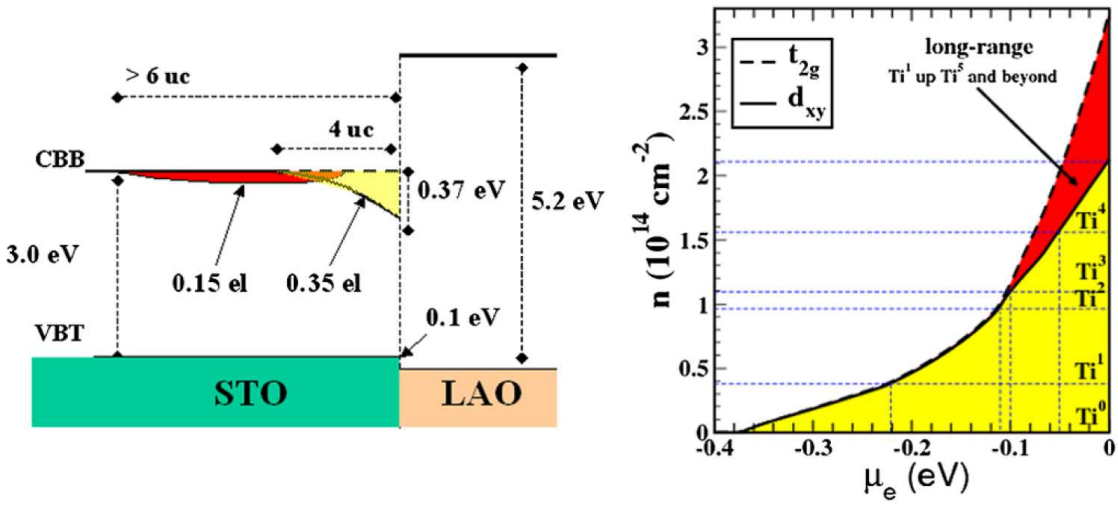

Figure 6.5: *Left: sketch of the band alignment at the LAO-STO interface as calculated in pSIC; yellow (light gray) and red (dark gray) areas indicate d_{xy} and $d_{xz} + d_{yz}$ contributions, respectively. Right: total t_{2g} (dashed) and d_{xy} (solid) charge densities per unit area as a function of chemical potential, calculated from the interface with 0.5 e^-/S assuming a rigid-band behavior ($E_F = 0$ corresponds to occupancy 0.5 e^-/S or 3.3 $\times$ 10^{14} cm^{-2}). Yellow (light gray) and red (dark gray) areas are contributions of planar d_{xy} and orthogonal (d_{xz}, d_{yz}) orbitals, respectively. On the right y axis, Ti^i indicates up to which Ti layer the d_{xy} charge (indicated by the dashed horizontal line) spreads.*

obtained in our calculation. The confining potential for the d_{xy} charge (left, in yellow) is just the interpolated profile of the conduction band bottom for the occupied d_{xy} states. A general relation between n_s and thickness of the metallic region is given in figure 6.5, right. Here $n_s(E_F)$ is calculated as the integral from band bottom to E_F of the DOS shown in figure 6.3a, distinguishing total t_{2g} and d_{xy} contributions. The d_{xy} charge is extremely short range, peaking at Ti^0 and extending only up to five STO units; the (d_{xz}, d_{yz}) charge extends beyond the sixth STO layer below the interface. Despite the implicit rigid-band approximation, the plot interpolates well the charge redistribution for n_s calculated directly in figure 6.5b and figure 6.5c: for n_s up to 0.4×10^{14} cm^{-2} the charge is entirely hosted by Ti^0 d_{xy}; above this value the Ti^1 $_{dxy}$ state begins to fill as well. At $n_c \simeq 10^{14}$ cm^{-2} (0.15 e^-/S) even Ti^2 and Ti^3 d_{xy} states host some charge, while immediately above this level the charge spills onto d_{xz}, d_{yz} states, progressively acquiring a delocalized character. Hence, n_c represents the maximum concentration which can be accommodated exclusively by d_{xy} states, and is highly confined in a $\sim$ 1.5-2 nm range from the interface.

6.2.2 Comparison to experimental data

We can use the model to analyze experimentally reported carrier densities. Several experiments (XAS [47], atomic force microscopy [28], hard x-ray photoemission [39, 64]) report confinement regions of few nm, in line with our results. Huijben *et al.* [40] found for the STO/LAO superlattice a small $n_s \sim 0.2 \times 10^{14}$ cm^{-2} at $T = 0$ K, which according to our results should imply charge entirely localized within 1 nm from the interface. A similar value was reported by Thiel *et al.* [32] for the freestanding LAO film. Dubroka *et al.* [46] recently found $n_s = 0.9 \times 10^{14}$ cm^{-2}, that is near our critical n_c, and should imply a confinement length of 2 nm or so. In fact, the n_s profile measured by ellipsometry does decay sharply at about 2 nm, quite consistently with our calculated d_{xy} density profile. An additional tail, vanishing at 11 nm, with a fourfold reduced carrier density, could be reasonably associated with the extended d_{yz}, d_{xz} doublet charge (see populations in Table 6.1).

6.2.3 Additional properties

We now come back to figure 6.4c to discuss the Fermi surface. We can distinguish five roughly circular Fermi sheets corresponding to the five Ti^i d_{xy} states ($i = 0, 4$) partially occupied at $n_s = 0.5$ e$^-$/S [figure 6.3a]. They are markedly parabolic in the (k_x, k_y) plane, and resemble closely their bulk counterparts. Contrariwise, d_{xz} and d_{yz} bands are quite anisotropic. The sketch in figure 6.4d illustrates how the largest Fermi surface for $n_s = 0.5$ e$^-$/S is in fact the intersection of d_{xz} and d_{yz} high-eccentricity ellipses with the circular d_{xy} section due to Ti^0. At lower $n_s = 0.15$ e$^-$/S (panel b), on the other hand, only circular d_{xy} sheets are occupied. The doublet bands, though, linger just above E_F, and small charge fluctuation may cause sloshing out of the 2 nm wide confinement region. The difference between singlet and doublet is also reflected in the calculated effective band mass m^*. For the d_{xy} bands, $m^*_x = m^*_y = 0.7$ (in units of m_e); for d_{xz} bands $m^*_x = 0.7$ and $m^*_y = 8.8$ (for d_{yz}, $m^*_x = 8.8$, $m^*_y = 0.7$ by symmetry). Thus, we are left with light electrons with $m^*_L = 0.7$ hosted by d_{xy} states, and heavy electrons with $m^*_H = 2(m^*_x m^*_y)/(m^*_x + m^*_y) = 1.3$ traveling within d_{xz} and d_{yz} states. They will contribute differently to mobility and transport. The ratio of conductivity due to d_{xy} carriers at Ti^0 to that of d_{xz}, d_{yz} electrons in their most populated layer (Ti^3) is $\sigma_0/\sigma_3 = n_0 m^*_H / n_3 m^*_L \sim 5.6$, where n_0 and n_3 are the calculated sheet densities for Ti^0 and Ti^3, respectively. Averaging over light and heavy carriers we obtain $m^* = n(m^*_L m^*_H)/(n_L m^*_H + n_H m^*_y) = 0.81$, with $n = (n_L + n_H) = 1/2$,

and n_L and n_H the total charge of singlet and doublet states, respectively, (last row of Table 6.1). Accounting for electron-phonon renormalization using a coupling constant $\lambda \sim 3$ typical for n-type STO [167], our estimate becomes $m_r^* = (1+\lambda)m^* \simeq 3.2$, in agreement with that inferred from ellipsometry and transport [46], $m^* = 3.2 \pm 0.4$. Our interface band mass is only 25% larger than the corresponding STO bulk value: this is in line with recent observations [168] which found no thermopower enhancement in STO/LAO structures compared to STO bulk. Remarkably, the band shapes remain substantially unchanged with n_s; hence, planar mobility should not depend on carrier concentration in the intrinsic limit.

6.3 Rumpling and buckling

Previously we described how the built-in electric field implies structural distortions in LAO through electrostrictive effects. The rumpling was already defined in chapter 3 as the distance between the cation and the anion of a layer divided by 2. However, in $SrTiO_3$ the origin of the structural distortions is the conductive charges that spread in the Ti $3d$ orbitals. The intensity does not depend directly on the charges but on the difference of charges, $\Delta\sigma$, in each layers[5]. The charge difference $\Delta\sigma$ is at the origin of a microscopic electric field which leads to local forces on anions and cations.

In the pristine $LaAlO_3$ thin film on (001) $SrTiO_3$ substrate, the charge density after the breakdown increase with the LAO film thickness. The structural distortions, here the rumpling in STO, should also increase with the film thickness. For $n = 4$, see figure 6.6, the system is still insulating and, in STO, no effect on atomic position is seen except the small one due to the interface. For $n = 5$, the system becomes metallic and some charges are transferred into the Ti $3d$ orbitals. Due to the orbital ordering the electrons preferentially fill the d_{xy} orbitals first, which are highly confined at the interface. The structural distortions reflect this behavior with a large rumpling close to the interface even if the rumpling is not strictly zero in the rest of STO[6]. For $n = 6$ the carrier density increased and become greater than σ_c leading to the filling of the Ti d_{yz} and d_{xz} orbitals, more spread in STO. This corresponds to a large increase of the rumpling in STO,

[5] Ti $3d$ orbitals are well localized in space.

[6] By fixing the thickness to $n = 5$ the carrier density is also fixed and it appears that the value is already close to σ_c and d_{xz}-d_{yz} are just below the Fermi level in this case. This is not always the case and in some systems these bands are really empty and above the Fermi level as predicted by the model.

excepted at the interface (still a factor of 2) where d_{xy} orbitals are now more slowly filled. In these thin film systems, the rumpling at the interface depends on the LAO thickness (i.e. the charge density) and is always smaller than the value found in superlattice, which corresponds to the maximum of charge transferred. As we approach the interface in STO, the lattice parameter gradually increases as observed in reference [60] where they attributed this effect to the distribution of Ti^{3+} atoms as shown in reference [94].

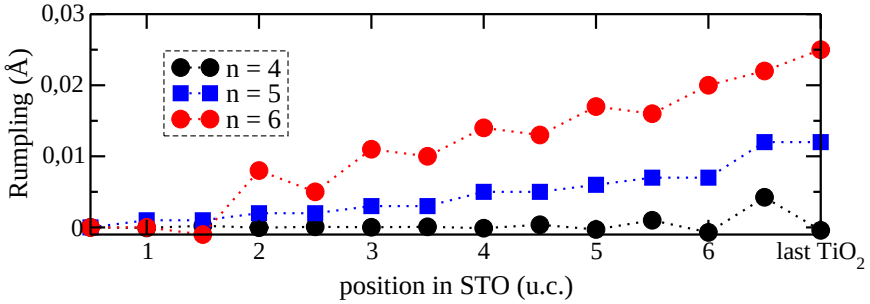

Figure 6.6: *The rumpling in SrO and TiO_2 layers for 3 different thicknesses. For $n = 4$: $\sigma_S = 0$, for $n = 5$: $\sigma_S < \sigma_c$ and for $n = 6$: $\sigma_S > \sigma_c$. The rumpling spreads into the STO when the critical carrier density σ_c is reached for thicknesses bigger than 6.*

6.4 Conclusion

Using advanced first-principles methods, we provided an accurate description of the 2DEL at the intrinsic TiO_2/LaO interface of STO/LAO heterostructures. We find the 2D charge confinement as due to interface-induced Ti $3d$ state splitting and to the localized nature of the Ti $3d_{xy}$ states, thus supporting the experimental attribution [46, 47, 157] of 2DEL formation to a primarily electronic origin[7]. Our results establish a relationship between sheet carrier density and spatial extension of the 2DEL, setting an intrinsic threshold ($n_c \sim 10^{14}$ cm^{-2} or 0.15 e$^-$/S) to the sheet carrier concentration of d_{xy} character that may be strictly localized near the interface; above this value, carriers start spilling over into the STO substrate. A connection between carrier density, binding energy, and thickness of the 2DEL is provided, which will be of practical guidance for future experiments and calculations.

[7] possibly reinforced by interface localized atomic displacements and, e.g., the analysis of nonlinear dielectric response at the interface presented in reference [44].

Chapter 7

Conclusions and outlook

This work has been devoted to the study of the polar $LaAlO_3$ thin film on a non-polar $SrTiO_3$ (001) substrate, for which we have given a complete study with an advanced functional: the hybrid B1-WC. The main achievement of this work is that we have provided arguments, based on first-principles calculations on pristine LAO/STO interface and in collaboration with experimentalists, supporting the polar-catastrophe scenario through i) the presence of an electric field probed through electrostriction and ii) a tunable metal/insulator threshold. Doing that, we have shown the importance of the polar discontinuity in these kind of systems.

In this way, we made our own contribution to the LAO-STO interface, which is a large and constantly evolving field. In addition, we have shown that *ab initio* calculations can be predictive in this complex system, in particular thanks to a collaboration with experimentalists. Moreover, some of our scientific results would not have been possible without this approach, that strongly couples theoretical simulations and experiments. For the future, it would be interesting to continue such a collaboration that proved its effectiveness, possibly on other polar/non-polar interfaces.

We have shown the prominent role of the polar discontinuity and the intrinsic nature in the $LaAlO_3$-$SrTiO_3$ interfaces. In a pristine (or almost pristine) interface, the electronic reconstruction is totally practicable. However, in a non-pristine interface, some defects can be activated, leading to other reconstruction mechanisms. For this reason, our work has left open which mechanism is really at the origin of the 2DEG. Indeed, the studies presented in chapter 4 and 5 could both give rise to a Zener breakdown or activation redox reactions. Likely both can contribute, and the one dominating could depend on growing conditions. The question of which mechanism occurs first is then less important

since, anyway, both of them predict a metal/insulator transition around 4 unit cells.

In chapter 6, we have studied the electronic confinement showing a critical carrier density at which the charges start spilling over into the STO substrate, an effect due to the localized nature of the Ti states. One of the biggest remaining issues is, however, the sheet carrier density obtained by Hall transport measurements, one order of magnitude lower than predicted. As an attempt to answer this problem, we considered the Fermi surface and the energy-band occupancy for various charge-carrier densities. However, the rigid band approximation (used for calculations in chapter 6) was no longer used. We have shown that experimental data of Fermi surface correspond to energy-band occupancies of low charge-carrier densities, suggesting that part of the electrons are trapped somewhere else. These results were recently published in reference [166].

This manuscript has presented our results related to the $LaAlO_3$-$SrTiO_3$ interface. However, it is only a part of the studies performed during this thesis. Indeed, the skills we have acquired during this work have been used to tackle other systems.
Thanks to our knowledge of the simulation package CRYSTAL and of the functional B1-WC, we have studied other oxide systems, such as half-doped titanates. In this system, we have highlighted the appearance of robust ferromagnetic and insulator states through the combination of two different types of Jahn-Teller motions, leading to an unusual charge and orbital ordering of the Ti d electrons. In addition, thanks to a ferroelectric state, with a spontaneous polarization approaching that of $BaTiO_3$, half-doped layered titanates could give a general concept to ferromagnetic ferroelectric multiferroics. These results are already in the publication process and are presented in appendix A.
In addition, we have dedicated a study to the $SrTiO_3$ under epitaxial constraints with a Landau-Ginzburg-Devonshire approach. This method, already used in biaxial strained STO, has been extended to uniaxial and isotropic constraints, showing the appearance of a ferroelectric state at room temperature. This study, supported by first-principles calculations, will soon be submitted to publication process. The latest version is presented in appendix B.
Finally, we have studied an organic ferroelectric compound: the polyvinylidene fluoride (CH_2-CF_2). In addition to a characterization through first-principles calculations, we studied the reversal polarization mechanism which can be easier thanks to a volume expansion. This work will be in the redaction process soon.

List of the scientific contributions

Publications in international journals

1. ML Reinle-Schmitt, C Cancellieri, Danfeng Li, **Denis Fontaine**, M Medarde, E Pomjakushina, CW Schneider, Stefano Gariglio, Ph Ghosez, J-M Triscone and PR Willmott.
   Tunable conductivity threshold at polar oxide interfaces.
   Nature communications, **3**, 932 (2012).
   doi:10.1038/ncomms1936.

2. Claudia Cancellieri, **Denis Fontaine**, Stefano Gariglio, Nicolas Reyren, AD Caviglia, Alexandre Fête, SJ Leake, SA Pauli, PR Willmott, M Stengel, Ph Ghosez and J-M Triscone.
   Electrostriction at the $LaAlO_3/SrTiO_3$ interface.
   Physical Review Letters, **107**, 056102 (2011).
   doi:10.1103/PhysRevLett.107.056102.

3. C. Cancellieri, M. L. Reinle-Schmitt, M. Kobayashi, V. N. Strocov, P. R. Willmott, **D. Fontaine**, Ph. Ghosez, A. Filippetti, P. Delugas, and V. Fiorentini.
   Doping-dependent band structure of $LaAlO_3/SrTiO_3$ interfaces by soft x-ray polarization-controlled resonant angle-resolved photoemission.
   Physical Review B, 89, 121412(R) (2014).
   doi:10.1103/PhysRevB.89.121412.

4. Pietro Delugas, Alessio Filippetti, Vincenzo Fiorentini, Daniel I Bilc, **Denis Fontaine** and Philippe Ghosez,
   Spontaneous 2-Dimensional Carrier Confinement at the n-Type $SrTiO_3/LaAlO_3$ Interface.
   Physical Review Letters, **106**, 166807 (2011).
   doi:10.1103/PhysRevLett.106.166807.

5. N.C. Bristowe, D. Fontaine, J. Varignon, E. Bousquet and Ph. Ghosez,
   Ferromagnetism induced by entangled charge and orbital orderings in ferroelectric titanate perovskites.
   in submission process.

6. Henu Sharma, Denis Fontaine, Jens Kreisel and Philippe Ghosez,
   First-principles and Landau theory studies of $SrTiO_3$.
   in preparation.

Conferences and seminars

1. **D. Fontaine**, *First-principles modelling of the $SrTiO_3/LaAlO_3$ interface with the B1-WC functional..*
   Oral presentation at the Triscone's group Scientific workshop, Stresa, Italy June 2-4, 2010.

2. **D. Fontaine**, *Theory and modelling of functional materials: Running activities at ULg.*
   Oral presentation at the Bushmills Workshop, Bushmills IRELAND, June 6-8, 2010.

3. **D. Fontaine**, *First principles study of PVDF.*
   Oral presentation at the Fundamental Physics of Ferroelectrics and Related Materials. National Institute of Standards and Technology (NIST), Gaithersburg, MD USA, January 2011.

4. **D. Fontaine**, *Ab-initio study of the electrostrictive effect on the $LaAlO_3/SrTiO_3$ structure.*
   Oral presentation at the Third international oxides workshop: engineering exotic phenomena at oxide interfaces, Olbia (Italy), 24-28 May 2011.

5. **D. Fontaine**, *First-principles study of $LaAlO_3/SrTiO_3$ interface: a summary.*
   Oral presentation at the Second international oxides workshop: engineering exotic phenomena at oxide interfaces, Santander (Spain), - 201.

Posters

1. **D. Fontaine**, *Ab initio study of 2DEG at $LaAlO_3/SrTiO_3$ interface.*
   Poster at the Fundamental Physics of Ferroelectrics and Related Materials. National Institute of Standards and Technology (NIST), Gaithersburg, MD USA, 2011.

2. **D. Fontaine**, *Ab initio study of the $SrTiO_3/LaAlO_3$ interface.*
   Poster at the Nature conference, Frontiers in electronic materials, Aachen Germany , 17-20 June 2012.

3. **D. Fontaine**, *Ab initio study of 2DEG at $SrTiO_3/LaAlO_3$ interface.*
   Poster at the Interuniversity attraction poles (AIP), quantum effect in clusters and nanowires , Hasselt (Belgium) , 26 November 2010.

4. **D. Fontaine**, *Designing enhanced polarization and ferromagnetism in hybrid-improper ferroelectric oxide superlattices from first principles.*
   Poster at the Fundamental Physics of Ferroelectrics and Related Materials. National Institute of Standards and Technology (NIST), Gaithersburg, MD USA, 2014.

Appendix A

Ferromagnetism induced by entangled charge and orbital orderings in ferroelectric titanate perovskites

N.C. Bristowe,[1] D. Fontaine,[1] J. Varignon,[1] E. Bousquet,[1] and Ph. Ghosez[1]

[1] *Theoretical Materials Physics, University of Liège, B-4000 Sart-Tilman, Belgium*

(Dated: July 8, 2014)

In magnetic materials, the Pauli exclusion principle typically drives anti-alignment between electron spins on neighbouring species resulting in antiferromagnetic behaviour. Ferromagnets exhibiting spontaneous spin alignment is a fairly rare behaviour, but once materialized is often associated with itinerant electrons in metals. Here we predict and rationalise robust ferromagnetism in an insulating oxide perovskite structure based on the popular titanate series. In half-doped layered titanates, the combination of two different types of Jahn-Teller motions opens a band gap and creates an unusual charge and orbital ordering of the Ti *d* electrons. It is argued that this intriguingly intricate electronic network favours the elusive *inter-site* ferromagnetic ordering, on the basis of *intra-site* Hund's rules. Finally we find that the layered oxides are also ferroelectric with a spontaneous polarization approaching that of $BaTiO_3$. The concepts are general and design principles of the technologically desirable ferromagnetic ferroelectric multiferroics are presented.

Perovskite oxides exhibit a fascinating range of physical properties, including ferroelectricity, (anti)ferromagnetism (AFM), superconductivity and magnetoresistance. This diverse behaviour is appealing for both fundamental and applied investigations, and has resulted in an intense global research effort over the past few decades. Many of these functional properties manifest due to the complex and subtle interplay between spin, charge, orbital and lattice degrees of freedom in perovskites [1–4]. Of the perovskites, the doped manganites have become a prototypical playground for the study of this interplay. Just considering the case of half-doping, i.e. $A_{0.5}R_{0.5}MnO_3$ where A is a divalent alkaline earth metal ion and R is a trivalent rare earth ion, manganites exhibit a rich variety of electronic phases. For example half-doped manganites can display ferromagnetic (FM) or A-type AFM metallic behaviour [5–7] or more commonly a CE-type AFM Mott insulating phase [8, 9] associated with two different charge orderings (Rocksalt [10] and Columnar [11]), and two different orbital orderings ("ferro" and "antiferro" Mn d e_g orderings [12]). The preferred electronic phase appears to be strongly dependent on the A and R cation sizes and whether they appear disordered (such as with Ca and La/Pr) or layered (such as for Ba and La/Tb/Y [5, 10, 12]) in the crystal.

In this regard, it is interesting to compare the physics of the half-doped manganites, with that of the half-doped titanates. At the bulk level the A and R cations are found to naturally disorder [13, 14] in the titanates, and typically no charge and orbital ordered Mott insulating phase is observed at half-doping [15]. An exception has been recently discovered for the case of very small A-cations, such as $Ca_{0.5}Lu_{0.5}TiO_3$, where a rocksalt charge-ordered and d_{xy} t_{2g} orbital-ordered Mott insulating phase was recently proposed [16]. On the other hand, in layered superlattices consisting of a repeating unit of k layers of $ATiO_3$ with l layers of $RTiO_3$, exotic behaviour such as an interface two-dimensional electron gas [17], which can be ferromagnetic (FM) [18] and superconducting [19] has been reported.

Here we consider half-doped titanates in short-period [001] superlattice form (k=l=1) (see figure 1), which can be artificially grown using modern layer-by-layer growth techniques. This case resembles a bulk-like double perovskite where every Ti ion shares the same mixed environment at odds with thicker superlattices. A careful first principles investigation (see Methods) including all possible degrees of freedom reveals an unexpected ferromagnetic and ferroelectric insulating ground state. The electronic structure exhibits an intricate orbital and charge ordering which is argued to be at the heart of the observed ferromagnetism. A symmetry lowering structural distortion enabling this particular orbital ordering

TABLE I: Key quantities for a selection of $ATiO_3$-$RTiO_3$ superlattices including amplitude Q (Å) of lattice distortions (in-phase Φ_z^+ and anti-phase Φ_{xy}^- AFD motions, polar mode P_{xy}, Jahn-Teller mode appearing at the M-point of the cubic Brillouin zone M_{JT}, breathing Jahn-Teller B_{JT}), polarization, P ($\mu C/cm^2$), band gap, Δ (eV), and gain of energy for FM vs AFM solution (see Methods) per 20-atom formula unit, ΔE (meV).

R, A	Q					P	Δ	ΔE
	Φ_z^+	Φ_{xy}^-	P_{xy}	B_{JT}	M_{JT}			
Sm, Sr	0.96	1.19	0.56	0.10	0.04	14.9	0.46	20.1
Y, Sr	1.10	1.30	0.66	0.11	0.04	16.7	0.57	18.0
Tm, Sr	1.18	1.36	0.72	0.11	0.03	18.2	0.63	16.4
Sm, Ba	0.75	0.96	0.48	0.13	0.07	18.6	0.50	18.5
Y, Ba	0.95	1.08	0.59	0.14	0.07	21.2	0.60	13.9
Tm, Ba	1.05	1.16	0.65	0.16	0.07	23.4	0.66	10.5

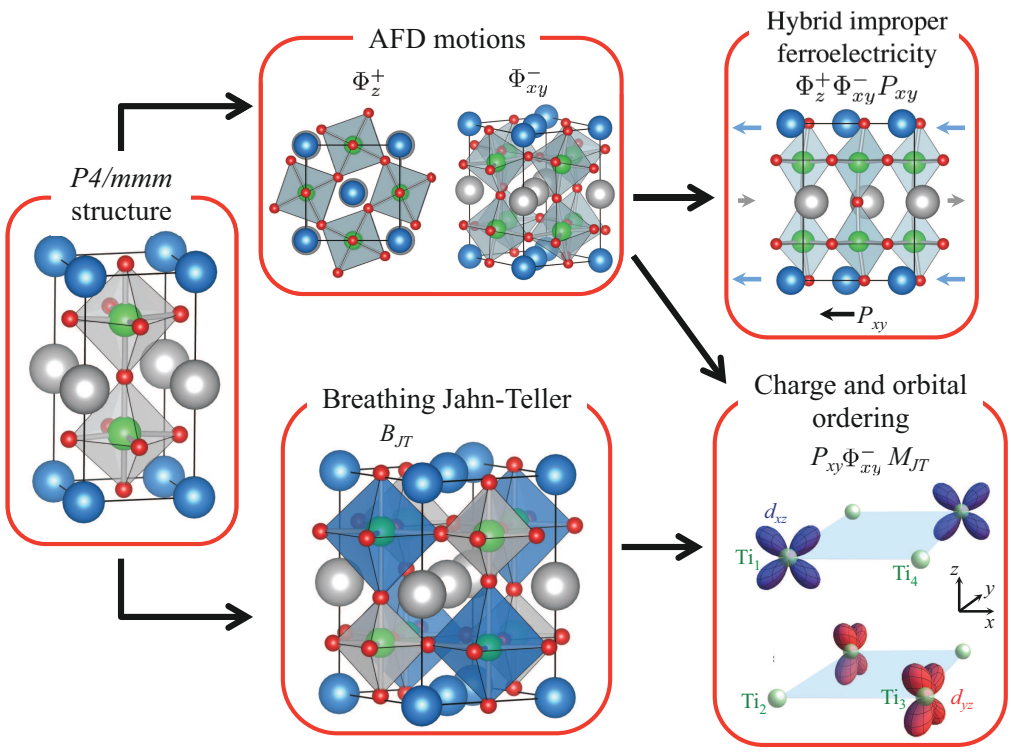

FIG. 1: (Color online) Superlattice geometry, major structural distortions, and resulting ferroelectric, charge and orbital ordering. The $ATiO_3$-$RTiO_3$ digital superlattice 10-atom high symmetry tetragonal $P4/mmm$ reference structure undergoes two major structural distortions; AFD motions and a breathing Jahn-Teller distortion. The rocksalt arrangement of large (blue) and small (grey) octahedral cages of the breathing Jahn-Teller are shown in the 20-atom cell. The AFD motions induce ferroelectricity through a unique anharmonic coupling to an in-plane polar mode. The combination of the AFD motions and breathing Jahn-Teller allows for an unusual charge and orbital ordering. Blue, grey, red and green spheres represent R, A, O and Ti respectively. Distortion are exaggerated for illustrative purposes.

is also found to drive the ferroelectricity. The results are found to be general across the whole $ATiO_3$-$RTiO_3$ (k=l=1) series, allowing for universal physical principles to be rationalized and new multiferroic design guidelines to be proposed. The subtle interplay between electronic and structural degrees of freedom are compared with the manganites and novel features are highlighted.

In order to unravel the unexpected ferroelectric and ferromagnetic behaviour, we begin by focussing on the atomic structure of the superlattice (see figure 1). In all cases we find a $P2_1$ symmetry ground state that consists of a complex combination of several lattice distortions (see table I) of the high-symmetry ($P4/mmm$) cube-on-cube double perovskite. Out of all the distortions, the largest in amplitude are oxygen octahedral rotations, both in-phase around the out-of-plane (z) axis, Φ_z^+, and anti-phase around the in-plane (x and y) axes, Φ_{xy}^- ($\Phi_x^- + \Phi_y^-$). These so-called antiferrodistortive (AFD) motions are ubiquitous in perovskites, appearing through steric effects described by the Goldschmidt tolerance factor [20]. The particular AFD pattern found here, $a^-a^-c^+$ in Glazer's notations [21], is the most common pattern shown by perovskites [22], certainly with tolerance factors between 0.8-1.0, the case studied here. This particular AFD pattern is stabilised over others in simple bulk perovskites through unique anharmonic couplings allowing the subsequent appearance of anti-polar A-cation motions [23–25], located at the zone-boundary of the cubic ABO_3 Brillouin zone. In the $ATiO_3$-$RTiO_3$ digital superlattices, this A and R-cation motion transforms to the zone-center, becoming polar in nature. The precise form of the anharmonic coupling is trilinear, $\Phi_z^+\Phi_{xy}^-P_{xy}$, which is the signature of the so-called rotationally driven hybrid improper ferroelectricity [26–28]. Indeed we calculate all superlattices to exhibit spontaneous polarizations in the range of 7-23 (μC/cm^2) (see for example Table I), approaching that of $BaTiO_3$ which is among the highest reported in hybrid improper ferroelectrics. Since the P_{xy}

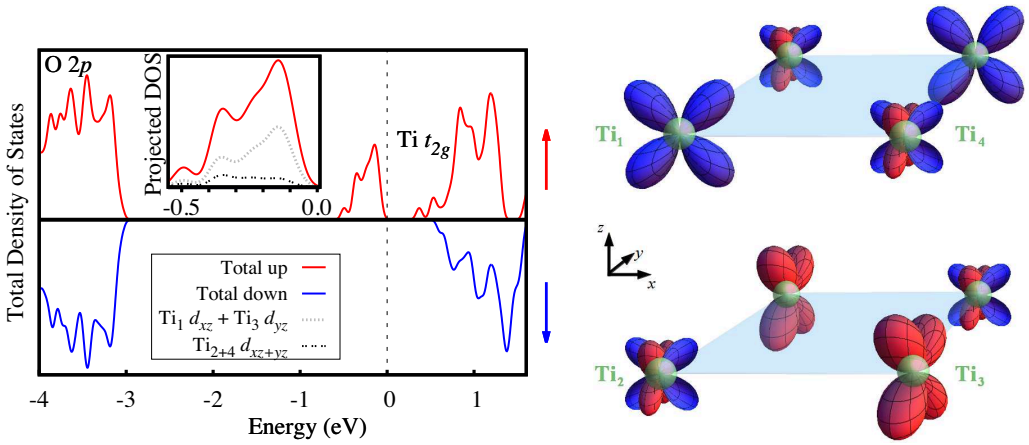

FIG. 2: (Color online) Left: Total and Projected spin-polarized Density of States (DOS). The upper panel (red), and lower panel (blue) correspond to up and down spins respectively. The vertical dashed line represents the Fermi level. The Projected DOS in the inset compares the Ti_1 d_{xz} + Ti_3 d_{yz} (grey fine dashed lines) with the Ti_{2+4} d_{xz+yz} (black dashed lines) DOS of the spin-split off state. Right: Sketch of the resulting orbital ordering. Green spheres represent Ti sites.

mode has a "ferri"-like character of the A and R cation motion (see figure 1), the large polarization is achieved by maximising the mode polarity through choosing A and R cations not only with asymmetric cation sizes [29] but also here thanks to significantly distinct Born effective charges (or valences in the simplest picture).

A necessary requirement of ferroelectricity is to be electronically insulating, which is not *a priori* obvious in these half-doped titanates. To achieve this a breathing Jahn-Teller motion, which expands or contracts the oxygen octahedra in nearest neighbour unit cells (see figure 1), appears in the ground state (Table I). This breathing distortion does not lift the degeneracy of the t_{2g} levels of the Ti atoms at the centre of each octahedra, but does lift the degeneracy between Ti sites. This motion is hence an electronic Jahn-Teller instability, driven to enable a d^1-d^0 charge ordering [47] , which helps to render the superlattices insulating. The charge ordering mimics the rocksalt pattern, and hence appears at the R-point (M-point) of the cubic (tetragonal) Brillouin zone, maximising the distance between the more highly charged d^0 Ti^{4+} ions.

This charge ordered insulating state is indeed found, as indicated through the spin-resolved density of states as presented for the FM solution in figure 2. The states near the Fermi level exhibit Ti d character, while the O $2p$ states appear deeper into the valence. A band gap separates an occupied spin-polarized "split-off" band from the remaining unoccupied Ti d conduction band. This "split-off" valence is found to consist of two bands with the majority of weight located at two different Ti sites, out of the four possible Ti sites in total in the 20-atom unit cell (see figure 1). These two sites are surrounded by the expanded oxygen octahedra, which we label the Ti d^1 sites, as opposed to the two other Ti d^0 sites surrounded by a contracted oxygen octahedra. Interestingly the orbital occupation of the two d^1 sites are different with one showing d_{xz} and the other d_{yz} character. The resulting orbital ordering corresponds to the same pattern, albeit with half the sites empty, as that achieved through a Jahn-Teller distortion appearing at the M-point of the cubic Brillouin zone (M_{JT}). This lattice distortion is indeed observed in the ground state (see table I). In fact it is found that the AFD motion themselves can achieve this orbital ordering, in absence of the M_{JT}, by lowering the symmetry of the bulk (superlattice) cubic (tetragonal) reference phase to orthorhombic (monoclinic). Indeed, similarly to the improper appearance of the polar A-cation motions, the AFD motions also drive the appearance of the M_{JT} distortion through another trilinear coupling, $P_{xy}\Phi^{-}_{xy}M_{JT}$ [30]. The fact that the AFD motions produce the same orbital ordering as the M_{JT} distortion is simply a consequence of this symmetry relation.

Interestingly, we find that the charge ordering is not exactly the ideal case of d^1-d^0. Defining m as the magnitude of the local magnetic moment, we find a $d^{(1-m)}$-d^m ordering, with a significant weight on the nominally d^0 sites ($0.11< m <0.18$ depending on the A and R species), displaying a mixed d_{xz}-d_{yz} character. The system remains insulating despite this delocalised state, through a strong hybridisation of the two occupied Ti d bands. The resulting intricate and entangled charge and orbital ordering is sketched in figure 2.

Having discussed the lattice, charge and orbital degrees of freedom, and their coupling, we move to the final de-

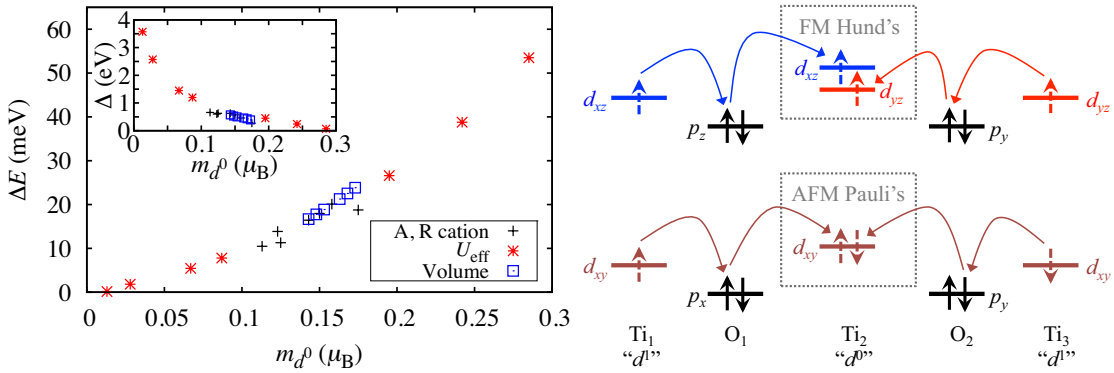

FIG. 3: (Color online) Left: Energy gain of FM compared to AFM state (see Methods) per 20-atom formula unit, ΔE, as a function of the moment on the d^0 sites, m_{d^0}. Inset: band gap Δ vs m_{d^0}. The different points correspond to various perturbations of the superlattice, including varying the A and R cation species, the on-site Coulomb repulsion U, and the volume of the cell. Right: Simplified spin exchange diagram between nearest neighbour d_1 sites (Ti_1 and Ti_3), via a d_0 site (Ti_2). The curved arrows represent inter-site spin hopping through oxygen ions, and the dashed box represents intra-site spin-exchange via Hund's rules, in the case of d_{xz}-d_{yz} orbital ordering due to AFD motions, or Pauli's exclusion principle, in the case of d_{xy} orbital ordering in the absence of AFD motions.

gree of freedom; spin. Various magnetic orderings (see methods) were studied, and in all cases and chemistries the ferromagnetic state was unexpectedly found to be the lowest in energy. In an attempt to understand the origin of this rare insulating FM ground state, we observe a universal trend across $ATiO_3$-$RTiO_3$ superlattices with all A and R species and various applied perturbations. This trend is shown in figure 3, where it is seen that the energy difference between AFM and FM states, or more simply the strength of the FM exchange, is clearly strongly dependent on the spin density of d electrons on the nominally d^0 sites. Indeed, as the system tends to the ideal charge ordering d^1-d^0, the FM and AFM energies tend to equilibrate. Therefore, in this regime, the spins on the two d^1 sites are completely decoupled. However, as the d^0-site electrons become populated, the FM exchange strengthens. This key observation indicates that the FM exchange mechanism relies on a real intra-site spin exchange on the nominally d^0 sites, rather than a virtual direct exchange between d^1 sites. We propose the intra-site FM spin exchange as Hund's rule (see figure 3).

To illustrate, we first note that by construction the spin of the d_{xz} (d_{yz}) orbital on the nominally d^0 site equals the spin of the d_{xz} (d_{yz}) orbital on the nearest neighbour d^1_{xz} (d^1_{yz}) site. This rule can be rationalised either within the hybridised band picture (figure 2 and supplementary material), or within a localized orbital spin hopping picture (figure 3). Since the spins on the d^0 orbitals dictate those on the d^1, and a density of spins on the d^0 site lowers the energy of the FM solution, the d^0_{xz}-d^0_{yz} intra-site spin exchange is at the heart of the observed FM. In the same spirit as Hund's rule of maximum multiplicity, which maximises the spin of an electron configuration of an atom, a FM solution of the d^0_{xz}-d^0_{yz} spins becomes the ground state. This rule minimises the intra-site Coulombic energy. The FM solution relies on both kinetic and Coulomb contributions, to delocalise the spin polarized d^1 electrons partially on the d^0 sites, and to align the d^0 intra-site spins, respectively. In this regard, it resembles a double (kinetic+Coulomb) exchange, even if in an insulator. This FM mechanism in d^0-d^1 charge ordered systems, which has been previously overlooked, extends the list of d^i-d^j charge orderings considered within the Goodenough-Kanamori rules [8, 31, 32].

Intriguingly, when AFD motions are artificially neglected the tetragonal symmetry can lead to an insulating charge ordered state but now with d_{xy} orbital ordering, once an unrealistically large on-site Coulomb repulsion U ($>$ 7eV) is enforced [33]. We have reproduced this computer experiment and find that the AFM solution now becomes slightly favoured. This can again be understood through the intra-site spin exchange on the nominally d^0 sites (see figure 3). An anti-alignment of spins on the intra-site d^0_{xy}-d^0_{xy} orbitals (and hence on the inter-site d^1_{xy}-d^1_{xy} orbitals) is favoured from Pauli's exclusion principles - now that the same orbital (spacial coordinate) is occupied, opposite electron spins are favoured. Therefore the combination of charge ordering at the R-point, via breathing Jahn-Teller motions, and orbital ordering at the M-point, via AFD and M_{JT} motions, of the cubic Brillouin zone is key to realise the FM ground state.

We note the FM mechanism here is distinct from the FM behaviour found in some $RTiO_3$ bulk compounds (for R from Gd to Yb). To illustrate, for example, we note

the FM coupling becomes stronger as the A size decreases and band gap [34] increases in bulk $RTiO_3$ compounds. This is seen through a transition from AFM to FM and then a rise in FM T_C with decreasing A size [35]. The reverse trend is observed here, where the FM coupling strengthens with increasing A cation size, and decreasing band gap.

It is interesting finally to compare the FM solution of the half-doped titanates, to the (A-type or E-type) AFM solution of the half-doped manganites. The magnetic ordering is likely different due to the superexchange interaction in the manganites between the fully occupied core t_{2g} electrons on every Mn site. This superexchange path is clearly cut-off by the rocksalt arrangement of d^0 sites in the titanates studied here. A FM insulating phase of the manganites does exists for the specific case of $Pr_{1-x}Ca_xMnO3$ with doping $x \approx 0.2$ [36–38], where a FM exchange wins due to a particular e_g orbital polaron ordering [39], not completely dissimilar to the t_{2g} case here, using the Goodenough-Kanamori rules [8, 31, 32].

Having rationalized the key concepts underlying the ferromagnetic and ferroelectric behaviour, we can propose some basic design rules and suggest alternative materials to achieve a similar multiferroic state. To ensure an insulating ground state, the smaller the A and R cations the larger the band gap, consistent with the recent observation of insulating $Ca_{0.5}Lu_{0.5}TiO_3$ [16]. Maximising the ferroelectric polarisation can be achieved by choosing the greatest asymmetry in both the born charge and size of the A and R cations. Regarding ferromagnetism, the exchange coupling constant J, and hence the FM T_C, increases the greater the delocalisation of charges onto the nominally d_0 sites which can be altered with strain and A-site chemistry as shown in figure 3. It could be interesting to test the same concepts on other B-cations such as the $4d$ and $5d$ transition metals, d^9-d^{10} systems such as the cuprates which can be viewed as a d^1-d^0 hole charge ordering, or d^6-d^7 systems with ordering of the single e_g electron instead of the t_{2g} in the titanates. Here might expect a similar type of entangled charge and orbital orderings leading to unexpected ferromagnetism, and hope that this study might encourage the search for related novel electronic phases within these systems.

METHODS

Unless stated otherwise in the main text results are presented for the case of $SmTiO_3$-$SrTiO_3$. Here we describe a three-step first principles strategy for the titanate calculations. i) Initially hybrid functional calculations, using the B1WC functional [40] within the Crystal code [41], were performed on bulk titanates ($YTiO_3$, $LaTiO_3$, $SrTiO_3$, $BaTiO_3$) and compared with experiment (see supp material). ii) Once verified on the bulk, hybrid functional calculations were performed on several representative $RTiO_3$-$ATiO_3$ superlattices. Ground states were determined through condensing various lattice instabilities and recalculating phonon frequencies. Band gaps and FM and AFM energies were computed on the ground states. iii) To make the calculations computationally tractable, and allow simulation of many more chemistries, GGA+U calculations [42], using the PBEsol functional [43] within the VASP code [44], were performed on the relaxed hybrid superlattice ground state structures. The on-site Coulomb repulsion U was fitted to simultaneously reproduce the band gap and spin flip energy of the hybrid functionals, and minimise atomic forces (see supp material), with a value of $U = 3.0$ eV found to be appropriate. This allowed for full structural relaxation using GGA+U on a wide-range of $RTiO_3$-$ATiO_3$ structures (R: La, Pr, Sm, Y, Tm, Lu. A: Sr, Ba, Ca). All lattice vectors were fully relaxed. Small to moderate in-plane strains resembling thin film epitaxy were not found to alter the qualitative findings presented (see supp material). Note we do not consider R f-electrons explicitly to simplify calculations and avoid a spurious mixing with the Ti d orbitals, which is a reasonable approximation since in practice the f-states should lie at much higher energies [45]. For longer range AFM orderings $2\times2\times1$, and $2\sqrt{2}\times\sqrt{2}\times1$ 40-atom supercells were relaxed with all possible spin orderings considered, including the CE-type. Unless stated otherwise the AFM ordering presented in the main text is the simplest allowed within the $\sqrt{2}\times\sqrt{2}\times1$ 20-atom cell.

Acknowledgments

Authors acknowledge stimulating discussions with N. Spaldin and C. Ederer, and support from the ARC project TheMoTherm. Ph. Ghosez acknowledges Research Professorship from the Francqui foundation. Calculations have been performed within the PRACE projects TheoMoMuLaM and TheDeNoMo and the NIC3 and NIC4 clusters at ULg.

[1] P. Zubko, S. Gariglio, M. Gabay, P. Ghosez, and J.-M. Triscone, Annu. Rev. Condens. Matter Phys. **2**, 141 (2011).
[2] H. Hwang, Y. Iwasa, M. Kawasaki, B. Keimer, N. Nagaosa, and Y. Tokura, Nat. Mater. **11**, 103 (2012).
[3] Y. Tokura and N. Nagaosa, Science **288**, 462 (2000).
[4] E. Dagotto, Science **309**, 257 (2005).
[5] F. Millange, V. Caignaert, B. Domenges, B. Raveau, and E. Suard, Chem. Mater. **10**, 1974 (1998).
[6] F. Millange, E. Suard, V. Caignaert, and B. Raveau, Mater. Res. Bull. **34**, 1 (1999).
[7] T. Nakajima, H. Kageyama, and Y. Ueda, J. Phys. Chem. Solids **63**, 913 (2002).
[8] J. B. Goodenough, Phys. Rev. **100**, 564 (1955).

[9] E. Wollan and W. Koehler, Phys. Rev. **100**, 545 (1955).
[10] A. J. Williams and J. P. Attfield, Phys. Rev. B **66**, 220405 (2002).
[11] P. Radaelli, D. Cox, M. Marezio, and S. Cheong, Phys. Rev. B **55**, 3015 (1997).
[12] A. J. Williams and J. P. Attfield, Phys. Rev. B **72**, 024436 (2005).
[13] H. Ju, C. Eylem, J. Peng, B. Eichhorn, and R. Greene, Phys. Rev. B **49**, 13335 (1994).
[14] C. Eylem, G. Saghi-Szabo, B. H. Chen, B. Eichhorn, J. L. Peng, R. Greene, L. Salamanca-Riba, and S. Nahm, Chem. Mater. **4**, 1038 (1992).
[15] Y. Tokura, Y. Taguchi, Y. Okada, Y. Fujishima, T. Arima, K. Kumagai, and Y. Iye, Phys. Rev. Lett. **70**, 2126 (1993).
[16] A. Komarek, M. Reuther, T. Lorenz, A. Cousson, P. Link, W. Morgenroth, D. Trots, C. Baehtz, and M. Braden, arXiv preprint arXiv:1109.0234 (2011).
[17] A. Ohtomo, D. Muller, J. Grazul, and H. Y. Hwang, Nature **419**, 378 (2002).
[18] S. Okamoto and A. J. Millis, Nature **428**, 630 (2004).
[19] J. Biscaras, N. Bergeal, A. Kushwaha, T. Wolf, A. Rastogi, R. C. Budhani, and J. Lesueur, Nature communications **1**, 89 (2010).
[20] V. M. Goldschmidt, Naturwissenschaften **14**, 477 (1926).
[21] A. Glazer, Acta Crystallogr. B **28**, 3384 (1972).
[22] M. W. Lufaso and P. M. Woodward, Acta Crystallogr. B **57**, 725 (2001).
[23] N. Miao, N. C. Bristowe, B. Xu, M. J. Verstraete, and P. Ghosez, J. Phys.: Condens. Matter **26**, 035401 (2014).
[24] N. W. Thomas, Acta Crystallogr. B **52**, 16 (1996).
[25] P. M. Woodward, Acta Crystallogr. B **53**, 44 (1997).
[26] E. Bousquet, M. Dawber, N. Stucki, C. Lichtensteiger, P. Hermet, S. Gariglio, J.-M. Triscone, and P. Ghosez, Nature **452**, 732 (2008).
[27] N. A. Benedek and C. J. Fennie, Phys. Rev. Lett. **106**, 107204 (2011).
[28] T. Fukushima, A. Stroppa, S. Picozzi, and J. M. Perez-Mato, Phys. Chem. Chem. Phys. **13**, 12186 (2011).
[29] A. T. Mulder, N. A. Benedek, J. M. Rondinelli, and C. J. Fennie, Adv. Funct. Mater. **23**, 4810 (2013).
[30] J. Varignon, N. Bristowe, E. Bousquet, and P. Ghosez, To be published (2014).
[31] J. B. Goodenough, J. Phys. Chem. Solids **6**, 287 (1958).
[32] J. Kanamori, J. Phys. Chem. Solids **10**, 87 (1959).
[33] R. Pentcheva and W. E. Pickett, Phys. Rev. Lett. **99**, 016802 (2007).
[34] Y. Okimoto, T. Katsufuji, Y. Okada, T. Arima, and Y. Tokura, Phys. Rev. B **51**, 9581 (1995).
[35] A. Komarek, H. Roth, M. Cwik, W.-D. Stein, J. Baier, M. Kriener, F. Bourée, T. Lorenz, and M. Braden, Phys. Rev. B **75**, 224402 (2007).
[36] Z. Jirak, S. Krupička, Z. Šimša, M. Dlouha, and S. Vratislav, J. Magn. Magn. Mater. **53**, 153 (1985).
[37] Y. Tomioka, A. Asamitsu, Y. Moritomo, H. Kuwahara, and Y. Tokura, Phys. Rev. Lett. **74**, 5108 (1995).
[38] H. Yoshizawa, H. Kawano, Y. Tomioka, and Y. Tokura, Phys. Rev. B **52**, R13145 (1995).
[39] T. Mizokawa, D. Khomskii, and G. Sawatzky, Phys. Rev. B **63**, 024403 (2000).
[40] D. Bilc, R. Orlando, R. Shaltaf, G.-M. Rignanese, J. Íñiguez, and P. Ghosez, Phys. Rev. B **77**, 165107 (2008).
[41] R. Dovesi, R. Orlando, B. Civalleri, C. Roetti, V. R. Saunders, and C. M. Zicovich-Wilson, Zeitschrift Fur Kristallographie **220**, 571 (2005).
[42] A. Liechtenstein, V. Anisimov, and J. Zaanen, Phys. Rev. B **52**, 5467 (1995).
[43] J. P. Perdew, A. Ruzsinszky, G. I. Csonka, O. A. Vydrov, G. E. Scuseria, L. A. Constantin, X. Zhou, and K. Burke, Phys. Rev. Lett. **100**, 136406 (2008).
[44] G. Kresse and J. Furthmüller, Phys. Rev. B **54**, 11169 (1996).
[45] M. Czyżyk and G. Sawatzky, Phys. Rev. B **49**, 14211 (1994).
[46] Y. Quan, V. Pardo, and W. E. Pickett, Phys. Rev. Lett. **109**, 216401 (2012).
[47] The term "charge ordering" throughout this article is used in the traditional sense as applied to, for example, the manganites, nickelates, ferrites and vanadates where a metallic to insulating transition is observed accompanied by the appearance of two unique transition metal sites, commonly thought to show two distinct valence states. The actual degree of charge ordering is ill-defined, depending on the non-unique method of partitioning charge amongst species, but various estimates typically suggest minimal charge disproportionation actually occurs in these materials (see for example the discussion within reference [46]). Similarly we calculate using Mulliken populations or LDA+U occupations the difference of charge to be only approximately 0.1 electrons between the two Ti sites. In this regard, it might be more accurate to replace "charge ordering" by "spin-density ordering" within this article. The inequivalence between the two Ti sites here is not only seen through the magnetic moment and orbital occupations, but also the Born effective charges which are reported in the supplementary material.

Appendix B

Theoretical study of $SrTiO_3$ under uniaxial, biaxial and isotropic mechanical strains

Henu Sharma[1,2,3], Denis Fontaine[1], Jens Kreisel[3,4], and Philippe Ghosez[1]
[1] *Physique Théorique des Matériaux, Université de Liège, B-4000 Sart Tilman, Belgium*
[2] *Lab. Matériaux et Génie Physique, Grenoble INP-CNRS, Grenoble, France*
[3] *Science and Analysis of Materials, Gabriel Lippmann Public Research Center, 41 Rue du Brill, L-4422 Belvaux, Luxembourg and*
[4] *Physics and Materials Science Research Unit, University of Luxembourg, 41 Rue du Brill, L-4422 Belvaux, Luxembourg*

The behavior of $SrTiO_3$ under uniaxial strains is investigated combining first-principles calculations within density functional theory and Landau-Ginzburg-Devonshire phenomenological theory. At the bulk level, we observe that uniaxial strain has a much larger effect on the ferroelectric instability than on the antiferrodistortive oxygen motions, suggesting a progressive evolution from an antiferrodistorted to a ferroelectric ground-state under increasing strains. The phase diagram of $SrTiO_3$ in terms of uniaxial strain and temperature has been obtained and compared to the case of biaxial and isotropic strains. We predict that $SrTiO_3$ can be made ferroelectric at room temperature under moderate uniaxial tensile strains.

I. INTRODUCTION

The understanding of ABO_3 perovskite-type oxides is a very active research area, of great relevance to both fundamental and application-related issues. Perovskite oxides form a particularly interesting class of materials because drastic changes of their physical properties can appear under even slight modifications of their crystal structure, as produced for instance through chemical substitution or external conditions, such as temperature or pressure[1,2]. Amongst ABO_3 compounds, $SrTiO_3$ is likely one of those that have attracted much attention, being simultaneously a prototypical quantum paraelectric[3] and a superconductor under doping at low temperature[4]. At a more applied level, $SrTiO_3$ is a component of $Ba_xSr_{1-x}TiO_3$ solid solutions widely used for tunable dielectric applications[5] and a promising n-type thermoelectric oxide compound[6]. Nowadays, it is also the most common substrate for epitaxial growth of various type of oxide nanostructures[8–11] and a key ingredient of the famous $LaAlO_3/SrTiO_3$ interface[12] developing a 2-dimensional electron gas, the properties of which are intimately linked to those of $SrTiO_3$.

Stable at high temperature in the ideal $Pm\bar{3}m$ cubic perovskite structure (see Fig. 1), $SrTiO_3$ combines ferroelectric (FE) and antiferrodistortive (AFD) structural instabilities. Under cooling, mechanically free bulk $SrTiO_3$ undergoes a unique cubic-to-tetragonal AFD phase transition at 105 K[13,14] to a non-polar phase of $I4/mcm$ symmetry. This appears as a typical displacive phase transition resulting from the softening of a phonon mode at the R-point of the cubic Brillouin zone (BZ), associated to the rotation of the oxygen octahedra[15]. At the same time, $SrTiO_3$ exhibits a progressive softening of a zone-center polar phonon mode, yielding a progressive divergence of its dielectric properties when temperature is lowered and that should produce a ferroelectric phase transition at very low-temperature. The latter is nevertheless suppressed by quantum fluctuations[16], making of $SrTiO_3$ a prototypical "quantum paraelectric"[3].

Previous studies already provided insight into the evolution of the structural properties of epitaxial $SrTiO_3$ thin films with temperature and epitaxial strain amplitude. It was so demonstrated experimentally that $SrTiO_3$ can be made ferroelectric at room temperature under appropriate biaxial strain[2,17], in agreement with Landau-Ginzburg-Devonshire theory[2] and first-principles calculations[20–22] restricted to the consideration of FE degrees of freedom. The tunability of the dielectric constant under epitaxial strain was also studied theoretically[24]. Using a more complete LGD model including explicitly AFD motions, Pertsev et al.,[23] then predicted a rich temperature–biaxial strain phase diagram, highlighting phases combining FE and AFD distortions, a result further confirmed at the first-principles level[18]. The behavior of $SrTiO_3$ under hydrostatic pressure has also been explored, highlighting a linear increase of the cubic to tetragonal AFD phase transition temperature up to room temperature or even above at high pressure[1]. Pressure dependence of the elastic constants of $SrTiO_3$ under hydrostatic pressure was also explored in the past[19].

Although, there have been various investigations of the behavior of $SrTiO_3$ under biaxial and isotropic strains, we are not aware of previous studies regarding the ef-

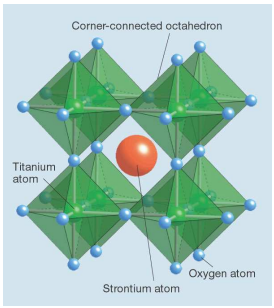

FIG. 1. The crystal structure of $SrTiO_3$[7]. Each titanium atom is bonded to six oxygen atoms, forming an octahedral structure.

fect of uniaxial mechanical constraints. In this work, we have extended our previous investigations on $PbTiO_3$ by exploring theoretically the effect of uniaxial strains on the properties of perovskite $SrTiO_3$, by combining first-principles calculations and phenomenological Landau-Ginzburg-Devonshire (LGD) model. For comparison, we also report results concerning the role of isotropic and biaxial strains. At first, we study the cubic phase of $SrTiO_3$, identify the most relavant phonon instabilities and discuss their evolution with strain using first-principles DFT calculations. Then, we determine the phase diagram of $SrTiO_3$ in terms of temperature and strain using LGD theory and discuss how these results compare with first-principles calculations.

II. TECHNICAL DETAILS

Our first-principles calculations have been performed in the framework of density functional theory (DFT) as implemented in the ABINIT package[25–27]. We did calculations using both (i) the local density approximation (LDA)[28] and extended norm-conserving Teter pseudopotentials[29] and (ii) the generalized gradient approximation with the functional proposed by Wu and Cohen (GGA-WC)[30] and optimized RRK pseudopotentials[31] generated with OPIUM code[32]. In both cases, semi-core states were treated as valence electrons, considering explicitly the following levels in the calculation: $4s$, $4p$ and $5s$ for the Sr atom, $3s$, $3p$, $3d$ and $4s$ for the Ti atom and $2s$ and $2p$ for the O atom. The wavefunction was expanded on a plane-wave basis set. Convergency was reached using a plane-wave energy cutoff of 45 hartrees.

In the 5 atoms perovskite ABO_3 unit cell, a Monkorsh-Pack mesh of 6×6×6 k points was used to sample the Brillouin zone. When condensing the AFD instabilities, we considered either a 20-atom supercell corresponding to $\sqrt{2}a_0$= a=b, and c= $2a_0$, and a sampling of 6×6×4 k points or, for the *Cmcm* phase, a 40-atom supercell corresponding to $2a_0$, $2a_0$, and $2a_0$ and a sampling of 4×4×4 k points. We explicitly checked that the relative energy of the different phases is well converged and independent of the choice of the supercell. Structural relaxations were performed until the forces were smaller than 10^{-7} hartrees/bohr and stresses are smaller than 10^{-8} hartrees/bohr^3. The vibrational properties, Born effective charges and dielectric tensors were calculated using the density functional perturbation theory (DFPT)[33]. The polarization has been computed using the modern theory of the polarization and the Berry phase formalism[34].

The Landau-Ginzburg-Devonshire (LGD) calculations have been performed following the scheme and using parameters provided in Ref.[23].

In what follows, we consider that the x, y and z cartesian axis are aligned respectively with the cell vectors a, b and c of the reference cubic structure. Then, the uniaxial constraint is always applied along the z-direction. To label the ferroelectric and antiferrodistortive motions compatible with a given space group, we use "generalized" Glazer's notations in which the superscripts refer as usual to the rotation pattern and a subscript P is added to identify the direction(s) along which a polarization can develop.

III. BULK STRUCTURE

First, we reinvestigate the highly-symmetric cubic perovskite structure of $SrTiO_3$. In this cubic phase, the atomic positions are fixed by symmetry and the only structural parameter to be relaxed is the lattice constant a_0. Our relaxed lattice constants a_0^{LDA} = 3.846 Å and a_0^{GGA} = 3.906 Å are comparable to previous calculations (a_0^{LDA} = 3.84 Å[35]) and in satisfactory agreement with experimental data (a_0^{EXP} = 3.905 Å[36]). As expected, the LDA tends to underestimate the experimental lattice constant that is nearly exactly reproduced at the GGA-WC level.

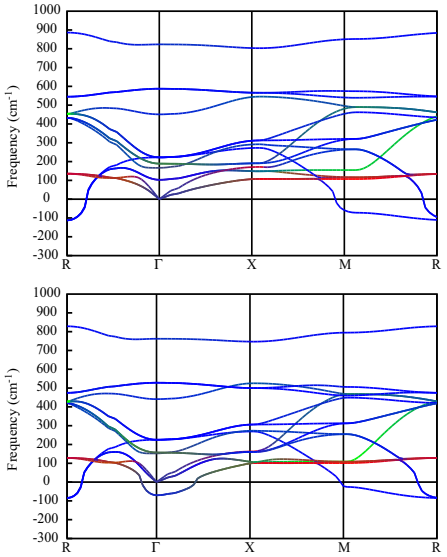

FIG. 2. Calculated phonon dispersion curves of cubic $SrTiO_3$, at the LDA volume (panel a) and at the GGA-WC volume (panel b) along the path R–Γ–X–M–R of the Brillouin zone.

The phonon dispersion curves of cubic $SrTiO_3$ calculated within the LDA and GGA-WC (at the optimized volume corresponding to each functional) are shown in Fig. 2. They significantly differ from each other, although agreeing each with the previous literature[35]. At the LDA level, we observe a single unstable phonon branch dominated by a R^{4+} instability at a frequency of 125i cm^{-1}. This mode corresponds to antiferrodistortive (AFD) motions associated to rotations of the oxygen oc-

tahedra, with consecutive octahedra along the rotation axis moving anti-phase (a^- in Glazer's notations). This instability then propagates all the way from R to M, connecting to an unstable M^{3+} mode at a frequency of 71i cm^{-1} which is associate to rotation of the oxygen octahedra with consecutive octahedra moving in-phase (a^+ in Glazer's notations). At the GGA-WC level, we still observe a similar branch of AFD unstable modes, although with a reduced amplitude of the instabilities, (R^{4+} mode at 84i cm^{-1} and M^{3+} mode at 25i cm^{-1}). Additionally, we now observe the appearance of a ferroelectric (FE) instability associated to a Γ^{4-} (F_{1u}) mode at a frequency of 70i cm^{-1} (stable at 102 cm^{-1} in LDA) and corresponding to a polar displacement of cations against the oxygen. This instability remains confined in a small volume of the Brillouin zone around the Γ point.

The difference between LDA and GGA-WC results can be assigned to their distinct relaxed volumes : contrary to the GGA-WC, the LDA underestimates the experimental lattice constant. This volume contraction, as usual in perovskites, suppresses the FE instability and amplifies the AFD instability. Our GGA-WC results closely resemble those obtained in the early calculation of LaSota *et al.*[37] within the LDA but at the experimental volume and highlight the incipient character of ferroelectricity in $SrTiO_3$.

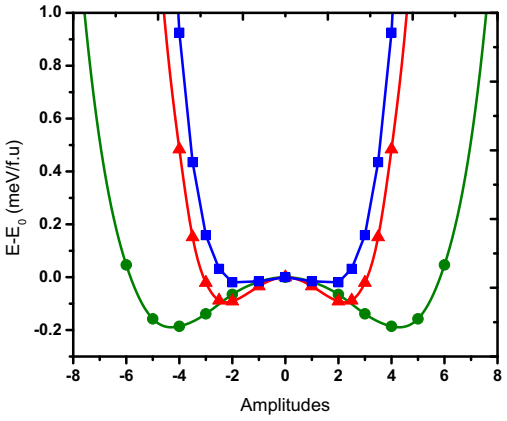

FIG. 3. (Color Online) Double-wells of (I4 /*mcm*) phase of $SrTiO_3$ at GGA volume. The green solid circles indicates *Ima*2 phase, red solid triangles indicates *Fmm*2 phase and blue solid squares indicates *I*4*cm* phase.

Since they predict distinct structural instabilities at the cubic level, we now investigate to which extent LDA and GGA-WC functionals both reproduce the correct ground state. In Table I, we report the energy and structural parameters of different metastable phases resulting from the condensation of (i) different combinations of AFD modes at R and M points and, at the GGA-WC level, (ii) the additional FE instability at the Γ point. Within the LDA, the largest gain of energy is obtained for the *I*4/*mcm* symmetry compatible with the ($a^0a^0c^-$) oxygen tilt pattern, consistently with the experimental ground state. We observe that the a^+ rotation pattern always produces a much lower gain of energy. In line with this, we notice that atomic relaxations in the *Cmcm* ($a^0b^+c^-$) and *Pbnm* ($a^-a^-c^+$) symmetries relax back to the *I*4/*mcm* and *Imma* phases respectively, attesting that the appearance of the a^- rotation suppresses the instability associated to a^+ motions. Within the GGA-WC we observe the same trend as for the LDA, although with typically lower gains of energy. In this case, the FE distortion is unstable but, in comparison to the AFD motions, it produces significantly lower energy gains. This ferroelectric instability is nevertheless not suppressed by the AFD motions and the *I*4/*mcm* phase presents phonon zone-center instabilities associated to FE distortions polarized along x, y and z at frequencies of 70i cm^{-1}, 70i cm^{-1} 66i cm^{-1}. Condensing into the *I*4/*mcm* phase the unstable FE motion polarized along x, xy and z lowers the symmetry of the system to *Fmm*2, *Ima*2 and *I*4*cm* respectively and yield the dou-

Phase	Unit cell a (Å)	b (Å)	c (Å)	Energy ΔE (meV/f.u.)	Distortion(s) Angle or P_s (° or $\mu C/cm^2$)
$a^0a^0a^0$	3.846	3.846	3.846	0	–
*Pm*3*m*	(3.906)	(3.906)	(3.906)	(0)	–
Exp.[36]	3.905	3.905	3.905	–	–
$a^0a^0c^0_P$	–	–	–	–	–
*P*4*mm*	(3.903)	(3.903)	(3.917)	(-0.57)	(P_s = 17.46)
$a^0_Pa^0_Pc^0$	–	–	–	–	–
*Amm*2	(3.911)	(3.911)	(3.902)	(-0.59)	(P_s = 19.55)
$a^0_Pa^0_Pa^0_P$	–	–	–	–	–
*R*3*m*	(3.908)	(3.908)	(3.908)	(-0.55)	(P_s = 20.08)
$a^0a^0c^+$	5.423	5.423	7.719	-4.48	c^+ = 4.91
*P*4/*mbm*	(5.522)	(5.522)	(7.812)	(0.18)	(c^+ = 1.08)
$a^0a^0c^-$	5.409	5.409	7.739	-23.02	c^- = 7.17
I4 /*mcm*	(5.507)	(5.507)	(7.840)	(-8.13)	(c^- = 5.65)
Exp.[39]	5.507	5.507	7.796	–	(c^- = 2.01)
$a^-a^-c^0$	5.426	5.455	7.657	-21.15	a^- = 4.81
Imma	(5.516)	(5.533)	(7.790)	(-7.41)	(a^- = 3.78)
*R*3*c*	7.681	7.681	7.681	-20.32	a^- =3.82
($a^-a^-a^-$)	(7.806)	(7.806)	(7.806)	(-7.18)	(a^- =3.01)
$a^0_Pa^0_Pc^-$	–	–	–	–	–
*Ima*2	(5.511)	(5.515)	(7.833)	(-8.48)	(P_s = 17) (c^- = 5.49)
$a^-_Pa^-_Pc^-$	–	–	–	–	–
Cc	(5.510)	(5.513)	(7.839)	(-8.51)	(P_s = 16) (a^- = 0.65) (c^- = 4.77)

TABLE I. Cell parameters, internal energies and distortion amplitudes of different meta-stable phases of $SrTiO_3$ fully relaxed within the LDA and the GGA-WC (values in brackets). For each phase, we specify the space group and, in brackets, the compatible FE and AFD structural distortion using generalized Glazer's notations (see method Section). The amplitude of the spontaneous polarization (P_s) and of the oxygen octahedra rotation angle (ϕ) are reported when appropriate.

ble wells shown in Fig. 3. The largest gain of energy is associated to a polar distortion along the xy direction. Fully relaxing the associated $Ima2$ phase ($a^0_P a^0_P c^-$), the gain of energy is of -8.48 meV/f.u, with a polarization $P_s = -0.17$ C/m^2. Recomputing the phonons in this $Ima2$ phase, we found again one unstable mode at a frequency of 29i cm^{-1}, including a complex interplay between oxygen motions and polar motions of Ti along z and anti-polar motions of Sr along xy. Condensing this mode, the symmetry is lowered to Cc. Fully relaxing within the Cc space group, the final gain of energy is of -8.51 meV/f.u. Within this relaxed Cc phase, we did not identified any phonon instability. At the GGA-WC level, the ground state is therefore no more the $I4/mcm$ phase but an unexpected Cc phase. The difference of energy between the $I4/mcm$ and Cc phases is however very tiny and beyond the expected accuracy of our calculations. This result highlights the incipient ferroelectric character of $SrTiO_3$ and is compatible with its quantum paraelectric character.

In order to anticipate how the ground state of $SrTiO_3$ can be affected by mechanical constraints, we now analyze how the amplitude of the most relevant FE instabilities at Γ and AFD instabilities at R of the reference paraelectric structure are evolving under uniaxial strains. For comparison, we did the same investigation for biaxial and isotropic strains.

Under isotropic strain, the paraelectric reference remains cubic and we can directly follow the strain evolution of the Γ^{4-} and R^{4+} modes. Applying a uniaxial strain along the z axis or a biaxial strain along the x and y axis, the $Pm\bar{3}m$ structure becomes tetragonal ($P4/mmm$ symmetry). This splits the triply degenerated Γ^{4-} (F_{1u}) FE mode into a single Γ^{3-} (A_1) mode and a doubly degenerated Γ^{5-} (E) mode, polarized respectively along c-axis and perpendicularly to it. Similarly the triply degenerated R^{4+} AFD mode is split into a single A_z mode and a doubly degenerated A mode, corresponding respectively to oxygen rotations about the z-axis or about the x or y axis for the uniaxial strain and the vice-versa for the biaxial strain. The evolution of the frequencies of these modes with isotropic, biaxial and uniaxial strains are reported in Fig. 4 at both LDA and GGA volume.

Although the AFD instability dominate at the bulk level, the situation can strongly evolve with strain. As general rules, (i) FE and AFD instabilities are oppositely affected by strain and (ii) the FE instability is more affected than the AFD one. For the isotropic case, the FE mode (triply degenerate) is strongly destabilized under tensile strains and AFD mode (triply degenerate) under compression. Under biaxial strain, the Γ^{5-} (resp. Γ^{3-}) mode is strongly destabilized under tension (resp. compression), becoming the dominant instability at large strains. Under uniaxial strain, the situation is very similar except that Γ^{5-} (resp. Γ^{3-}) mode is now destabilized under compression (resp. tension). LDA and GGA-WC reproduce globally the same trends. These results highlight that, similarly to what has been made under biaxial strain, uniaxial strain can switch the hierarchy between AFD and FE instabilities and likely make $SrTiO_3$ ferroelectric.

IV. UNIAXIAL STRAIN

A. LGD theory

In order to access the phase diagrams of $SrTiO_3$ in terms of different types of strain and temperature, we switch now to a phenomenological description within LGD theory. In view of the previous discussion, we adopted a model including explicitly FE (polarization amplitudes P_i), AFD (a^- rotation amplitudes q_i) and strain (S_i) degrees of freedom, as previously proposed by Pertsev et al.,[23]. In this framework, the Helmholtz free energy density F in terms of P_i, q_i and S_i is written as :

$$
\begin{aligned}
F = & \alpha_1 \left(P_1^2 + P_2^2 + P_3^2\right) + \alpha_{11} \left(P_1^4 + P_2^4 + P_3^4\right) \\
& + \alpha_{12} \left(P_1^2 P_2^2 + P_2^2 P_3^2 + P_1^2 P_3^2\right) \\
& + \beta_1 \left(q_1^2 + q_2^2 + q_3^2\right) + \beta_{11} \left(q_1^4 + q_2^4 + q_3^4\right) \\
& + \beta_{12} \left(q_1^2 q_2^2 + q_2^2 q_3^2 + q_1^2 q_3^2\right) \\
& + \frac{1}{2} c_{11} \left(S_1^2 + S_2^2 + S_3^2\right) + c_{12} \left(S_1 S_2 + S_2 S_3 + S_1 S_3\right) \\
& + \frac{1}{2} c_{44} \left(S_4^2 + S_5^2 + S_6^2\right) \\
& - g_{11} \left(S_1 P_1^2 + S_2 P_2^2 + S_3 P_3^2\right) \\
& - g_{12} \left(S_1 \left(P_2^2 + P_3^2\right) + S_2 \left(P_1^2 + P_3^2\right) + S_3 \left(P_1^2 + P_2^2\right)\right) \\
& - g_{44} \left(S_4 P_2 P_3 + S_5 P_1 P_3 + S_6 P_1 P_2\right) \\
& - \lambda_{11} \left(S_1 q_1^2 + S_2 q_2^2 + S_3 q_3^2\right) \\
& - \lambda_{12} \left(S_1 \left(q_2^2 + q_3^2\right) + S_2 \left(q_1^2 + q_3^2\right) + S_3 \left(q_1^2 + q_2^2\right)\right) \\
& - \lambda_{44} \left(S_4 q_2 q_3 + S_5 q_1 q_3 + S_6 q_1 q_2\right) \\
& - t_{11} \left(P_1 q_1^2 + P_2 q_2^2 + P_3 q_3^2\right) \\
& - t_{12} \left(P_1 \left(q_2^2 + q_3^2\right) + P_2 \left(q_1^2 + q_3^2\right) + P_3 \left(q_1^2 + q_2^2\right)\right) \\
& - t_{44} \left(P_1 P_2 q_1 q_2 + P_2 P_3 q_2 q_3 + P_1 P_3 q_1 q_3\right),
\end{aligned}
$$

where α_i and β_i are the coefficients of the FE and AFD energy wells, c_{nl} are the elastic stiffnesses, g_{nl} are the electrostrictive constants, λ_{nl} describe the coupling between the strain and AFD oxygen motions, and t_{nl} define the interaction between the polarization and AFD oxygen motions. As usual in such phenomenological approach, all these parameters are considered as constant except for α_1 and β_1 given by :

$$
\begin{aligned}
\alpha_1 &= 4.5 \left[\coth(54/T) - \coth(54/30)\right] 10^{-3} \\
\beta_1 &= 1.32 \left[\coth(145/T) - \coth(145/105)\right] 10^{26}
\end{aligned}
$$

The phase diagrams are then built by identifying the configuration of parameters that minimizes F at each temperature under some fixed mechanical constraints.

In case of fixed *isotropic* strains, we assume that $S_1 = S_2 = S_3$. Then shear strains were also fixed to zero,

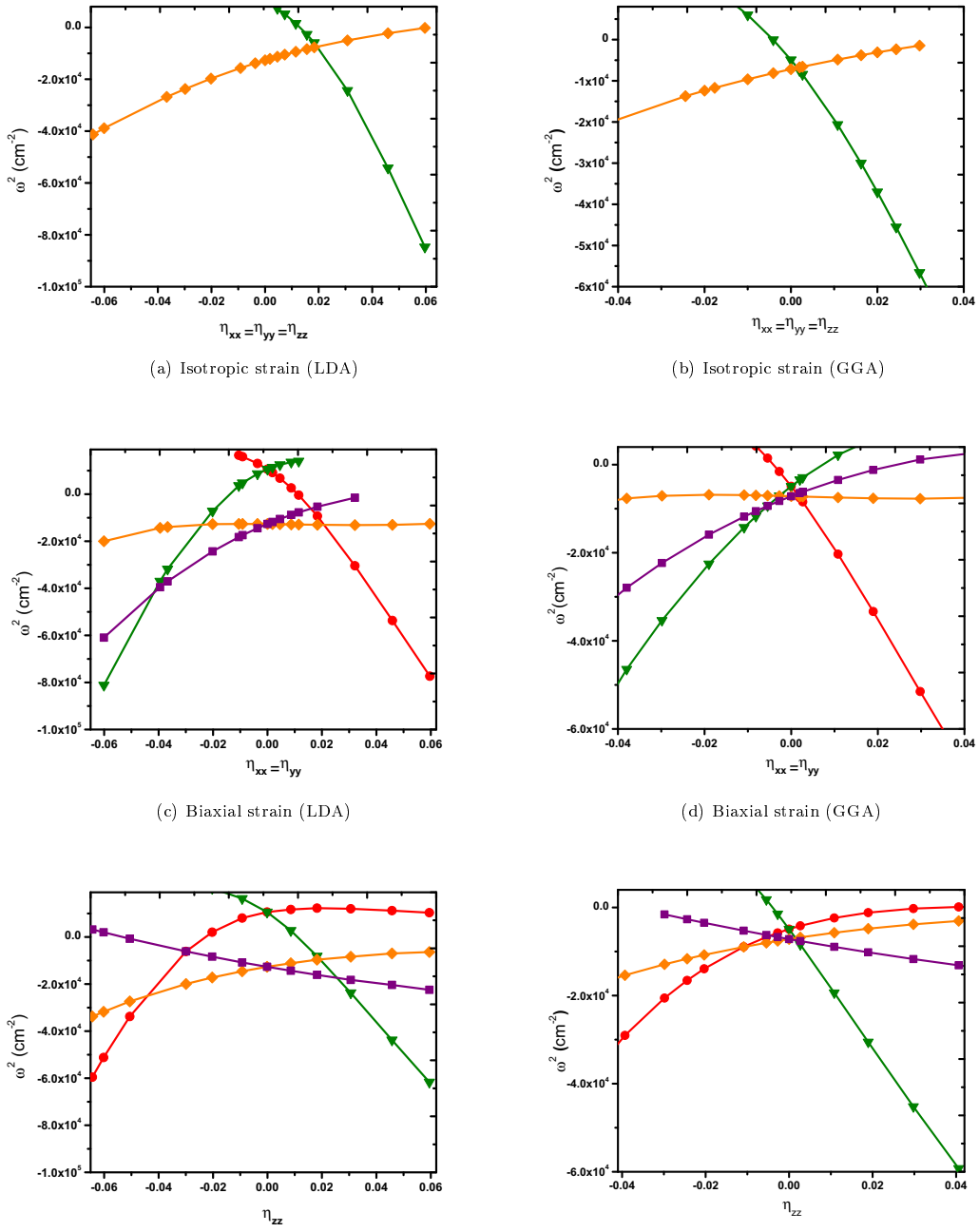

(a) Isotropic strain (LDA)

(b) Isotropic strain (GGA)

(c) Biaxial strain (LDA)

(d) Biaxial strain (GGA)

(e) Uniaxial strain (LDA)

(f) Uniaxial strain (GGA)

FIG. 4. (Color Online) Evolution of the square of the frequency of the FE and AFD modes under isotropic, biaxial and uniaxial strains in the paraelectric $P4/mmm$ phase of $SrTiO_3$, as obtained within the LDA and GGA-WC volume. Here, Γ^{3-} (green triangles) and Γ^{5-} (red circles) and of the AFD modes A_3^+ (purple squares) and A_5^+ (orange diamonds) for (panel c, d, e and f). For triply degenerate FE modes, Γ^{5-} or Γ^{3-} is indicated in (green triangles) and triply degenerate AFD modes A_3^+ or A_5^+, in (orange diamonds) (panel a and b).

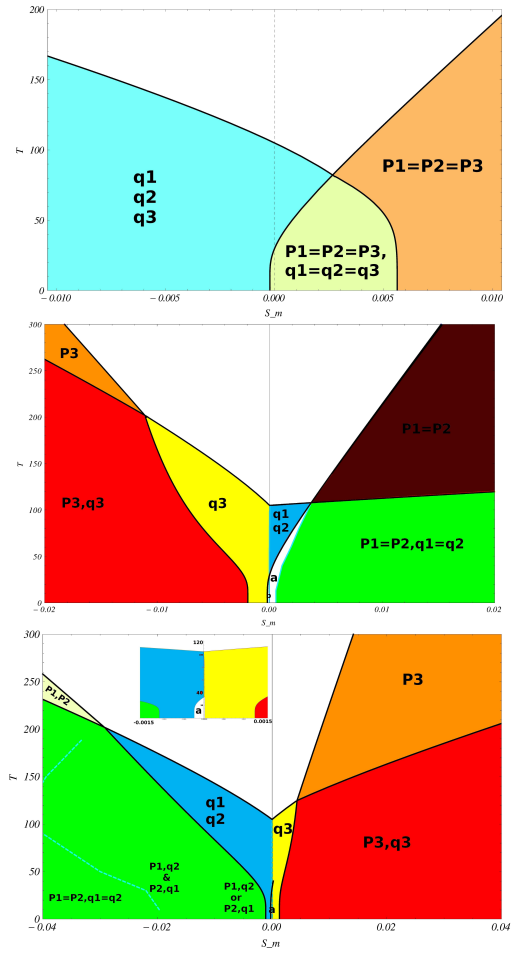

FIG. 5. Phase diagram of $SrTiO_3$ under isotropic (panel a), biaxial (panel b) and uniaxial strains (panel c) using LGD theory.

although we explicitly checked that relaxing them is not playing any significant role. This corresponds to

$$S_1 = S_2 = S_3 = S_m = \frac{a^* - a_0}{a_0}$$
$$S_4 = S_5 = S_6 = 0$$

The phase diagram is reported and in Fig. 5(a). It is consistent with the evolution of the phonon frequencies previously discussed, highlighting a purely FE ground state under tension and a purely AFD ground state under compression.

In the case of fixed *biaxial* strains imposed in the x and y directions, mimicking the epitaxial strain imposed to thin films by a cubic substrate (fixing S_1, S_2 and S_6), we have mixed mechanical boundary conditions corresponding to :

$$S_1 = S_2 = S_m = \frac{a^* - a_0}{a_0}, S_6 = 0$$
$$\frac{\delta F}{\delta S_3} = \frac{\delta F}{\delta S_4} = \frac{\delta F}{\delta S_5} = 0$$

In our calculations, we neglect the possible appearance of a depolarizing field along z, which corresponds to the case a a relatively thick film between metallic electrodes in short-circuit. The phase diagram reported in Fig. 5(b) corresponds to that previously reported by Pertsev et al.[23]. At small strains, different AFD tilt patterns can be observed while FE distortion appears at increasing strains. It confirms that $SrTiO_3$ can be made FE at room temperature under both moderate tensile and compressive epitaxial strains. This is again consistent with the fact that FE phonon instabilities become dominant as strain increases. As highlighted in the previous Section, large biaxial strains do however not suppress all AFD instabilities so that phases combining FE and AFD distortions are observed at lower temperature.

In case of fixed *uniaxial* strain applied along the z axis, only S_3 is fixed while all other strain components are free to relax :

$$S_1 = S_m = \frac{a^* - a_0}{a_0}$$
$$\frac{\delta F}{\delta S_2} = \frac{\delta F}{\delta S_3} = \frac{\delta F}{\delta S_4} = \frac{\delta F}{\delta S_5} = \frac{\delta F}{\delta S_6} = 0$$

The phase diagram obtained under uniaxial strain is reported in Fig. 5(c). It present close similarities with that observed under biaxial strains, the phases stabilized under compression being now observed under tension and *vice versa*. We observe that a very moderate tensile uniaxial strain can make $SrTiO_3$ ferroelectric at room temperature, while doing so under compression would require a much larger strain. At low temperatures, the system is expected to go through a sequence of many different phase transitions when the strain evolves from +4 to -4 %, as also summarized in Fig.6. Under tension, $SrTiO_3$ combines FE and AFD motions along z axis. When the strain is reduced, the FE distortion first disappears. Then under compression, the AFD motion switches from rotations around the z to the x (or y) axis and, later, a polarization additionally appears along x. Progressively when compressive strains continue to increase, FE and AFD motions rotates from x to xy direction. Some of these phases are stable in a very narrow range of strains.

First-principles calculations

LGD theory predicts a rich and complex phase diagram for $SrTiO_3$ under uniaxial strain. It is interesting to check how the sequence of phase transition expected at low temperature is validated by first-principles calculations at the LDA and GGA-WC levels. To that end, we have compared the energetics of various different phases at

selected strains. The results are summarized in Fig.6. For each strain, we report the ground state identified with each functional. In cases where different phases are very close in energy (difference of energy of the order of 1 meV or lower), all of them are mentioned.

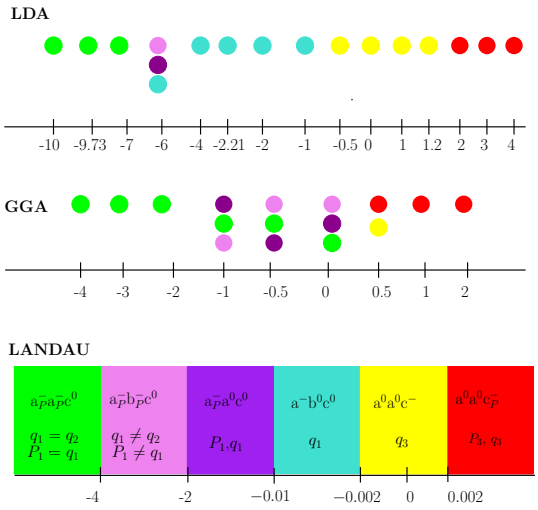

FIG. 6. Phase diagram of $SrTiO_3$ under uniaxial strain with LDA (panel a), GGA (panel b) and LGD theory (panel c).

The LDA reproduces qualitatively the phase predicted at the Landau level. However it significantly broadens the range of stability of the $a^-b^0c^0$ and $a^0a^0c^-$ phases. Still, the $a^-_P a^-_P c^0$ and $a^0a^0c^-_P$ phases appears under compression and tension respectively but at much larger strains than predicted from Landau theory. This is a direct consequence of the lower volume obtained in LDA that, as previously discussed, tends to suppress the ferroelectric instability.

At the opposite, the GGA-WC calculations tends to broaden the range of stability of the $a^-_P a^-_P c^0$ and $a^0a^0c^-_P$ phases. Between the range of stability of these two phases, there is a narrow region in which many phases are in close competition. The difference of energy between those phases is however so small (lower than 1 meV) that it is not possible to unambiguously determine the sequence of phase transition and limits between the different phases. As illustrated in Fig. 7, in the strain range of about -1%, a phase with different amplitude of oxygen AFD rotations around the x and y axis can be stabilized, confirming what is predicted at the LGD level. The same is obtained at the LDA level but at much larger strains. Overall, the GGA-WC calculation is therefore in close agreement with the LGD calculations and confirms the main features of the phase diagram obtained at that phenomenological level.

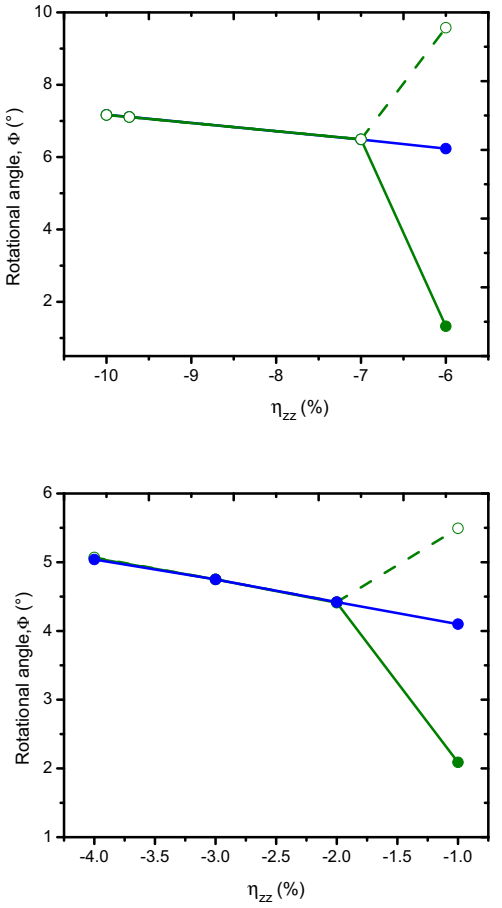

FIG. 7. (Color Online) Evolution of rotational angles of $Ima2$ and Cm phase of $SrTiO_3$ with LDA (panel a) and GGA (panel b) under compressive strains. Green solid circles and open circles indicates a^- and b^- rotational angles of Cm phase and blue solid circles indiates a^- angles of $Ima2$ phase.

V. CONCLUSIONS

In this work, we have investigated the role of uniaxial strain on the FE and AFD instabilities of $SrTiO_3$, making explicit comparison with the cases of isotropic and biaxial strains. The phase diagram in terms of uniaxial strain amplitude and temperature has been obtained in the context of LGD phenomenological theory, and confirmed from first-principles calculations. We predict a rich phase diagram, including phases combining FE and

AFD motions and presenting some close similarities with that obtained under biaxial strains. In particular, we predict that $SrTiO_3$ could easily be made ferroelectric under moderate uniaxial tensile strains, a feature that, we hope, can be further confirmed experimentally.

ACKNOWLEDGMENTS

This work was supported by Grenoble INP funded by IDS-FunMat, an International Doctoral Programme in Functional Materials. Additional financial support has been provided by the Gabriel Lippmann Public Research Center (Luxembourg), through the National Research Fund, Luxembourg (FNR/P12/4853155/Kreisel) and the University of Liège (Belgium) through the ARC project TheMoTherm. Ph.G. acknowledges a Research Professorship from the Francqui Foundation.

ANNEX

This annex reports the values of different phases of $SrTiO_3$ under tensile and compressive strains. Table. II and Table. III are the input for the uniaxial compressive strains and tensile strains of $SrTiO_3$ in GGA volume. Table. IV and Table. V are the input for the uniaxial compressive strains and tensile strains of $SrTiO_3$ in LDA volume.

[1] M. Guennou, P. Bouvier, and J. Kreisel, Phys. Rev. B. **81**, 054115 (2010).
[2] J. H. Haeni, P. Irvin, W. Chang, R. Uecker, P. Reiche, Y. L. Li, S. Choudhury, W. Tian, M. E. Hawley, B. Craigo, A. K. Tagantsev, X. Q. Pan, S. K. Streiffer, L. Q. Chen, S. W. Kirchoefer, J. Levy and D. G. Schlom, Nature **430**, 758-761 (12 August 2004).
[3] Müller, K.A., Burkard, H.: Phys. Rev. B **19**, 3593 (1979).
[4] J. F. Schooley, W. R. Hosler, and M. L. Cohen, Phys. Rev. Letters **12**, 474 (1964).
[5] Cole, M. W., Joshi, P. C., Ervin, M. H., Wood, M. C. and Pfeffer, R. L. The influence of Mg doping on the materials properties of $Ba_xSr_{1-x}TiO_3$ thin films for tunable device applications. Thin Solid Films 374, 34-41 (2000).
[6] H. Ohta. Mat. Today. 10 44-49 (2007).
[7] Michael O'Keeffe, Nature **419**, 28-29 (2002).
[8] Julia Slutsker, Igor Levin, Jianhua Li, Andrei Artemev and Alexander L. Roytburd, Phys. Rev. B **73**, 184127 (2006).
[9] Eric Bousquet, Matthew Dawber, Nicolas Stucki, Cèline Lichtensteiger, Patrick Hermet, Stefano Gariglio, Jean-Marc Triscone and Philippe Ghosez, Nature Vol **452**, (2008).
[10] M. Dawber, C. Lichtensteiger, M. Cantoni, M. Veithen, P. Ghosez, K. Johnston, K. M. Rabe, and J.-M. Triscone, PRL **95**, 177601 (2005).
[11] Agham-Bayan Posadas, Mill Lippmaa, Fred J. Walker, Matthew Dawber, Charles H. Ahn and Jean-Marc Triscone, Topics Appl. Physics **105**, 291-304 (2007).
[12] A. Ohtomo and H. Y. Hwang, Nature (London) 427, 423 (2004).
[13] G. Shirane and Y. Yamada, Phys. Rev. **177**, 858 (1969).
[14] H. Thomas and K. A. Müller, Phys. Rev. Lett. **21**, 1256 (1968).
[15] P. A. Fleury, J. F. Scott, and J. M. Worlock, Phys. Rev. Lett. **21**, 16 (1968).
[16] W. Zhong and D. Vanderbilt, Phys. Rev. B **53**, (1996).
[17] M. P. Warusawithana, C. Cen, Ch. R. Sleasman, J. C. Woicik, Y. Li, L. F. Kourkoutis, J. A. Klug, H. Li, Ph. Ryan, L.-P. Wang, M. Bedzyk, D. A. Muller, L.-Q. Chen, J. Levy, and D. G. Schlom, Science **17** 367 (2009).
[18] Lin, C.-H., Huang, C.-M. and Guo, G. Y, J. Appl. Phys. **100**, 084104 (2006).

Strain	Space groupNo.	Glazer's notation	*Delta*E (meV/f.u.)	R_x	R_y	R_z
0%	*Ima*2	$a^-_+a^-_+c^0$	-8.26	3.77	3.77	0
	Fmmm	$a^-a^0c^0$	-8.10	5.57	0	0
	Cm	$a^-_+b^-_+c^0$	**-8.44**	2.25	4.77	0
	*Fmm*2	$a^-_+a^0c^0$	-8.26	5.51	0	0
	I4/*mcm*	$a^0a^0c^-$	-5.77	0	0	5.10
-0.5%	*Ima*2	$a^-_+a^-_+c^0$	-7.25	3.95	3.95	0
	Fmmm	$a^-a^0c^0$	-6.72	5.90	0	0
	Cm	$a^-_+b^-_+c^0$	**-7.41**	2.07	5.21	0
	*Fmm*2	$a^-_+a^0c^0$	-7.13	5.83	0	0
	I4/*mcm*	$a^0a^0c^-$	-0.79	0	0	4.69
-1%	*Ima*2	$a^-_+a^-_+c^0$	-4.06	4.10	4.10	0
	Fmmm	$a^-a^0c^0$	-2.96	6.18	0	0
	Cm	$a^-_+b^-_+c^0$	-3.69	2.09	5.5	0
	*Fmm*2	$a^-_+a^0c^0$	**-4.18**	6.11	0	0
-2%	*Ima*2	$a^-_+a^-_+c^0$	10.15	4.42	4.42	0
	Fmmm	$a^-a^0c^0$	13.78	6.70	0	0
	Cm	$a^-_+b^-_+c^0$	**10.07**	4.41	4.42	0
	*Fmm*2	$a^-_+a^0c^0$	11.77	6.33	0	0
-3%	*Ima*2	$a^-_+a^-_+c^0$	34.20	4.75	4.75	0
	Fmmm	$a^-a^0c^0$	43.09	7.32	0	0
	Cm	$a^-_+b^-_+c^0$	**34.17**	4.75	4.75	0
	*Fmm*2	$a^-_+a^0c^0$	38.63	7.15	0	0
-4%	Ima2	$a^-_+a^-_+c^0$	**65.18**	5.05	5.05	0
	Fmmm	$a^-a^0c^0$	82.42	8	0	0
	Cm	$a^-_+b^-_+c^0$	65.23	5.06	5.07	0
	Fmm2	$a^-_+a^0c^0$	74.22	7.67	0	0

TABLE II. Uniaxial compressive strain, Space group No, gain in energy (meV/f.u) and rotational angles (°) for the phases of $SrTiO_3$ at GGA level.

[19] A. G. Beattie and G. A. Samara, Journal of applied physics, Volume **42**, Number 6, May (1971).

Strain	Space groupNo.	Glazer's notation	*Delta*E (meV/f.u.)	R_x	R_y	R_z
+0.5%	*Cmcm*	$a^0b^+c^-$	-6.88	0	5.25	0
	*I*4*cm*	$a^0a^0c^-_+$	**-7.96**	0	0	5.50
	I4/*mcm*	$a^0a^0c^-$	-7.96	0	0	5.50
+1%	*Cmcm*	$a^0b^+c^-$	-3.23	0	4.91	0
	*I*4*cm*	$a^0a^0c^-_+$	**-8.14**	0	0	5.62
	I4/*mcm*	$a^0a^0c^-$	-7.64	0	0	5.82
+2%	*Cmcm*	$a^0b^+c^-$	11.01	0	4.48	0
	*I*4*cm*	$a^0a^0c^-_+$	**-4.26**	0	0	5.93
	I4/*mcm*	$a^0a^0c^-$	0.26	0	0	6.30

TABLE III. Uniaxial tensile strain, Space group No, gain in energy (meV/f.u) and rotational angles (°) for the phases of $SrTiO_3$ at GGA level.

[20] O. Diéguez, K. M. Rabe, and D. Vanderbilt, Phys. Rev. B **72**, 144101 (2005).
[21] O. Diéguez and D. Vanderbilt, Cond-mat.mtrl-sci (2008).
[22] T. Hashimoto, T. Nishimatsu, H. Mizuseki, Y. Kawazoe, A. Sasaki, and Y. Ikeda, Jpn. J. Appl. Phys., Part 1 **44**, 7134 (2005).
[23] N. A. Pertsev, A. K. Tagantsev, and N. Setter, Phys. Rev. B **61**, R825 (2000); N. A. Pertsev, A. K. Tagantsev, and N. Setter, Phys. Rev. B **65**, 219901 (E) (2002).
[24] A. Antons, J. B. Neaton, K. M. Rabe, and D. Vanderbilt, Phys. Rev. B **71**, 024102 (2005).
[25] X. Gonze, J.-M. Beuken, R. Caracas, F. Detraux, M. Fuchs, G.-M. Rignanese, L. Sindic, M. Verstraete, G. Zerah, F. Jollet, M. Torrent, A. Roy, M. Mikami, Ph. Ghosez, J.-Y. Raty, and D. C. Allan, Comput. Mater. Sci. **25**, 478 (2002).
[26] X. Gonze, G.-M. Rignanese, M. Verstraete, J.-M. Beuken, Y. Pouillon, R. Caracas, F. Jollet, M. Torrent, G. Zerah, M. Mikami, Ph. Ghosez, M. Veithen, V. Olevano, L. Reining, R. Godby, G. Onida, D. Hamann, and D. C. Allan, Z. Kristallogr. **220**, 558 (2005).
[27] X. Gonze, B. Amadon, P.-M. Anglade, J.-M. Beuken, F. Bottin, P. Boulanger, F. Bruneval, D. Caliste, R. Caracas, M. Cote, T. Deutsch, L. Genovese, Ph. Ghosez, M. Giantomassi, S. Goedecker, D. R. Hamann, P. Hermet, F. Jollet, G. Jomard, S. Leroux, M. Mancini, S. Mazevet, M. J. T. Oliveira, G. Onida, Y. Pouillon, T. Rangel, G.-M. Rignanese, D. Sangalli, R. Shaltaf, M. Torrent, M. J. Verstraete, G. Zerah, and J. W. Zwanziger, Comput. Phys. Commun. **180**, 2582 (2009).
[28] S. Goedecker, M. Teter, J. Huetter, Phys. Rev. B **54**, 1703 (1996)
[29] M. Teter, Phys. Rev. B **48**, 5031 (1993).
[30] Z. Wu and R. E. Cohen, Phys. Rev. B **73**, 235116 (2006).
[31] A. M. Rappe, K. M. Rabe, E. Kaxiras, and J. D. Joannopoulos, Phys. Rev. B 41, 1227 (1990).
[32] see OPIUM website at http://opium.sourceforge.net/.
[33] X. Gonze and C. Lee, Phys. Rev. B **55**, 10355 (1997).
[34] D. King-Smith and D. Vanderbilt, Phys. Rev. B **47**, 1651(R) (1993).
[35] E. Bousquet, Ph.D. thesis, Universitè de Liège, 2008.
[36] Farrel W.Lytle, Journal of applied physics, Volume **35**, Number **7**, (July 1964).

Strain	Space groupNo.	Glazer's notation	*Delta*E (meV/f.u.)	R_x	R_y	R_z
-0.5%	I4/*mcm*	$a^0a^0c^-$	**-21.96** (GS)	0	0	6.89
-1%	*Ima*2	$a^-_+a^-_+c^0$	-21.15	4.80	4.80	0
	Fmmm	$a^-a^0c^0$	**-23.04**	7.08	0	0
	I4/*mcm*	$a^0a^0c^-$	-17.22	0	0	6.50
-2%	*Ima*2	$a^-_+a^-_+c^0$	-15.76	5.1	5.1	0
	Fmmm	$a^-a^0c^0$	**-18.91**	7.6	0	0
	I4/*mcm*	$a^0a^0c^-$	0.89	0	0	5.80
-2.21%	*Ima*2	$a^-_+a^-_+c^0$	-13.05	5.17	5.17	0
	Fmmm	$a^-a^0c^0$	**-16.75**	7.71	0	0
	I4/*mcm*	$a^0a^0c^-$	6.42	0	0	5.65
-4%	Ima2	$a^-_+a^-_+c^0$	33.50	5.73	5.73	0
	Fmmm	$a^-a^0c^0$	**26.64**	8.75	0	0
	I4/*mcm*	$a^0a^0c^-$	79.55	0	0	4.05
-6%	Ima2	$a^-_+a^-_+c^0$	127.81	6.23	6.23	0
	Fmmm	$a^-a^0c^0$	126.66	9.98	0	0
	Cm	$a^-_+b^-_+c^0$	126.03	0.44	9.80	0
	Fmm2	$a^-_+a^0c^0$	126.20	9.91	0	0
	I4/*mcm*	$a^0a^0c^-$	224.48	0	0	0
-7%	Ima2	$a^-_+a^-_+c^0$	191.05	6.49	6.49	0
	Fmmm	$a^-a^0c^0$	201.53	10.67	0	0
	Cm	$a^-_+b^-_+c^0$	190.95	6.50	6.50	0
	Fmm2	$a^-_+a^0c^0$	198.41	10.43	0	0
	I4/*mcm*	$a^0a^0c^-$	331.62	0	0	0
-9.73%	Ima2	$a^-_+a^-_+c^0$	**402.64**	7.11	7.11	0
	Fmmm	$a^-a^0c^0$	484.31	12.50	0	0
	Cm	$a^-_+b^-_+c^0$	**402.44**	7.10	7.10	0
	Fmm2	$a^-_+a^0c^0$	455.17	11.41	0	0
	I4/*mcm*	$a^0a^0c^-$	754.03	0	0	0
-10%	Ima2	$a^-_+a^-_+c^0$	**426.37**	7.17	7.17	0
	Fmmm	$a^-a^0c^0$	518.53	12.68	0	0
	Cm	$a^-_+b^-_+c^0$	**426.17**	7.17	7.17	0
	Fmm2	$a^-_+a^0c^0$	493.48	0.000019	0	0
	I4/*mcm*	$a^0a^0c^-$	807.35	0	0	0

TABLE IV. Uniaxial compressive strain, Space group No, gain in energy (meV/f.u) and rotational angles (°) for the phases of $SrTiO_3$ at LDA level.

[37] Chris LaSota, Cheng-Zhang Wang, Rici Yu, and Henry Krakauer, Ferroelectrics **194**, 109 (1997).
[38] Ying Xie, Hong-gang Fu, Hai-tao Yu, Guo-xu Zhang and Jia-zhong Sun, J. Phys.: Condens. Matter **19** (2007) 506213 (9pp).
[39] W. Jauch and A. Palmer, Phys. Rev. B **60**, 2961 (1999).

10

Strain	Space groupNo.	Glazer's notation	*Delta*E (meV/f.u.)	R_x	R_y	R_z
0%	I4/*mcm*	$a^0a^0c^-$	**-23.02**	0	0	7.17
+1%	I4/*mcm*	$a^0a^0c^-$	**-16.83**	0	0	7.77
+1.20%	I4/*mcm*	$a^0a^0c^-$	**-15.17**	0	0	7.85
+2%	I4/*mcm*	$a^0a^0c^-$	-1.91	0	0	8.28
	*I*4*cm*	$a^0a^0c^-_+$	**-2.03**	0	0	8.22
+3%	I4/*mcm*	$a^0a^0c^-$	24.38	0	0	8.80
	*I*4*cm*	$a^0a^0c^-_+$	**20.99**	0	0	8.55
+4%	I4/*mcm*	$a^0a^0c^-$	53.72	0	0	9.21
	*I*4*cm*	$a^0a^0c^-_+$	**44.05**	0	0	8.80

TABLE V. Uniaxial tensile strain, Space group No, gain in energy (meV/f.u) and rotational angles (°) for the phases of $SrTiO_3$ at LDA level.

References

[1] Ohtomo, A and Hwang, H Y, "A high-mobility electron gas at the $LaAlO_3/SrTiO_3$ heterointerface.," *Nature*, vol. 427, pp. 423–6, 2004.

[2] H. Y. Hwang, "Tuning interface states.," *Science*, vol. 313, no. 5795, pp. 1895–18966, 2006.

[3] S. A. Pauli and P. R. Willmott, "Conducting interfaces between polar and non-polar insulating perovskites," *Journal of Physics: Condensed Matter*, vol. 20, no. 26, p. 264012, 2008.

[4] M. Huijben, A. Brinkman, G. Koster, G. Rijnders, H. Hilgenkamp, and D. H. A. Blank, "Structure-property relation of $SrTiO_3/LaAlO_3$ interfaces," *Advanced Materials*, vol. 21, no. 17, pp. 1665–1677, 2009.

[5] J. Mannhart and D. G. Schlom, "Oxide interfaces–an opportunity for electronics.," *Science*, vol. 327, no. 5973, pp. 1607–11, 2010.

[6] H. Chen, A. M. Kolpak, and S. Ismail-Beigi, "Electronic and magnetic properties of $SrTiO_3/LaAlO_3$ interfaces from first principles," *Advanced Materials*, vol. 22, no. 26-27, pp. 2881–2899, 2010.

[7] D. G. Schlom and J. Mannhart, "Oxide electronics: Interface takes charge over Si," *Nat Mater*, vol. 10, no. 3, pp. 168–169, 2011.

[8] R. Pentcheva and W. E. Pickett, "Electronic phenomena at complex oxide interfaces: insights from first principles.," *J Phys Condens Matter*, vol. 22, no. 4, p. 043001, 2010.

[9] R. Pentcheva, R. Arras, K. Otte, V. G. Ruiz, and W. E. Pickett, "Termination control of electronic phases in oxide thin films and interfaces: $LaAlO_3/SrTiO_3(001)$," vol. 370, no. 1977, pp. 4904–4926, 2012.

[10] S. Chambers, M. Engelhard, V. Shutthanandan, Z. Zhu, T. Droubay, L. Qiao, P. Sushko, T. Feng, H. Lee, T. Gustafsson, E. Garfunkel, A. Shah, J.-M. Zuo, and Q. Ramasse, "Instability, intermixing and electronic structure at the epitaxial heterojunction," *Surface Science Reports*, vol. 65, no. 10-12, pp. 317 – 352, 2010.

[11] M. Gabay, S. Gariglio, J.-M. Triscone, and A. Santander-Syro, "2-dimensional oxide electronic gases: Interfaces and surfaces," *The European Physical Journal Special Topics*, vol. 222, no. 5, pp. 1177–1183, 2013.

[12] N. C. Bristowe, P. Ghosez, P. B. Littlewood, and E. Artacho, "The origin of two-dimensional electron gases at oxide interfaces: insights from theory," *Journal of Physics: Condensed Matter*, vol. 26, no. 14, p. 143201, 2014.

[13] N. Miao, N. C. Bristowe, B. Xu, M. J. Verstraete, and P. Ghosez, "First-principles study of the lattice dynamical properties of strontium ruthenate," *Journal of Physics: Condensed Matter*, vol. 26, no. 3, p. 035401, 2014.

[14] W. Zhong and D. Vanderbilt, "Effect of quantum fluctuations on structural phase transitions in $SrTiO_3$ and $BaTiO_3$," *Phys. Rev. B*, vol. 53, pp. 5047–5050, Mar 1996.

[15] N. A. Hill, "Why are there so few magnetic ferroelectrics?," *The Journal of Physical Chemistry B*, vol. 104, no. 29, pp. 6694–6709, 2000.

[16] H. Uwe and T. Sakudo, "Stress-induced ferroelectricity and soft phonon modes in $SrTiO_3$," *Phys. Rev. B*, vol. 13, pp. 271–286, Jan 1976.

[17] P. Zubko, S. Gariglio, M. Gabay, P. Ghosez, and J.-M. Triscone, "Interface physics in complex oxide heterostructures," *Annual Review of Condensed Matter Physics*, vol. 2, no. 1, pp. 141–165, 2011.

[18] P. Yu, Y.-H. Chu, and R. Ramesh, "Oxide interfaces: pathways to novel phenomena," *Materials Today*, vol. 15, no. 7âĂŞ8, pp. 320 – 327, 2012.

[19] E. Dagotto, "When oxides meet face to face," *Science*, vol. 318, no. 5853, pp. 1076–1077, 2007.

[20] M. Kawasaki, K. Takahashi, T. Maeda, R. Tsuchiya, M. Shinohara, O. Ishiyama, T. Yonezawa, M. Yoshimoto, and H. Koinuma, "Atomic control of the $SrTiO_3$ crystal surface," *Science*, vol. 266, pp. 1540–1542, 1994.

[21] G. Koster, B. L. Kropman, G. J. H. M. Rijnders, D. H. A. Blank, and H. Rogalla, "Quasi-ideal strontium titanate crystal surfaces through formation of strontium hydroxide," *Applied Physics Letters*, vol. 73, no. 20, pp. 2920–2922, 1998.

[22] T. Ohnishi, K. Shibuya, M. Lippmaa, D. Kobayashi, H. Kumigashira, M. Oshima, and H. Koinuma, "Preparation of thermally stable TiO_2-terminated $SrTiO_3$(100) substrate surfaces," *Applied Physics Letters*, vol. 85, no. 2, pp. 272–274, 2004.

[23] P. W. Tasker, "The stability of ionic crystal surfaces," *Journal of Physics C: Solid State Physics*, vol. 12, no. 22, p. 4977, 1979.

[24] N. C. Bristowe, P. B. Littlewood, and E. Artacho, "The net charge at interfaces between insulators.," *J Phys Condens Matter*, vol. 23, no. 8, p. 081001, 2011.

[25] M. Stengel and D. Vanderbilt, "Berry-phase theory of polar discontinuities at oxide-oxide interfaces," *Phys. Rev. B*, vol. 80, p. 241103, Dec 2009.

[26] D. Vanderbilt and R. D. King-Smith, "Electric polarization as a bulk quantity and its relation to surface charge," *Phys. Rev. B*, vol. 48, pp. 4442–4455, Aug 1993.

[27] G. A. Baraff, J. A. Appelbaum, and D. R. Hamann, "Self-consistent calculation of the electronic structure at an abrupt GaAs-Ge interface," *Phys. Rev. Lett.*, vol. 38, pp. 237–240, Jan 1977.

[28] M. Basletic, J.-L. Maurice, C. Carretero, G. Herranz, O. Copie, M. Bibes, E. Jacquet, K. Bouzehouane, S. Fusil, and A. Barthelemy, "Mapping the spatial distribution of charge carriers in $LaAlO_3/SrTiO_3$ heterostructures," *Nat. Mater.*, vol. 7, no. 8, pp. 621–625, 2008.

[29] N. Reyren, S. Thiel, A. D. Caviglia, L. F. Kourkoutis, G. Hammerl, C. Richter, C. W. Schneider, T. Kopp, A.-S. Rüetschi, D. Jaccard, M. Gabay, D. A. Muller, J.-M. Triscone, and J. Mannhart, "Superconducting interfaces between insulating oxides.," *Science*, vol. 317, no. 5842, pp. 1196–9, 2007.

[30] A. Brinkman, M. Huijben, M. van Zalk, J. Huijben, U. Zeitler, J. C. Maan, W. G. van der Wiel, G. Rijnders, D. H. A. Blank, and H. Hilgenkamp, "Magnetic effects at the interface between non-magnetic oxides," *Nat. Mater.*, vol. 6, pp. 493–496, 2007.

[31] A. D. Caviglia, S. Gariglio, N. Reyren, D. Jaccard, T. Schneider, M. Gabay, S. Thiel, G. Hammerl, J. Mannhart, and J.-M. Triscone, "Electric field control of the $LaAlO_3/SrTiO_3$ interface ground state.," *Nature*, vol. 456, no. 7222, pp. 624–7, 2008.

[32] S. Thiel, G. Hammerl, A. Schmehl, C. W. Schneider, and J. Mannhart, "Tunable quasi-two-dimensional electron gases in oxide heterostructures.," *Science*, vol. 313, no. 5795, pp. 1942–5, 2006.

[33] C. W. Schneider, S. Thiel, G. Hammerl, C. Richter, and J. Mannhart, "Microlithography of electron gases formed at interfaces in oxide heterostructures," *Applied Physics Letters*, vol. 89, no. 12, pp. –, 2006.

[34] N. Nakagawa, H. Y. Hwang, and D. A. Muller, "Why some interfaces cannot be sharp," *Nat Mater*, vol. 5, pp. 204–209, 2006.

[35] O. N. Tufte and P. W. Chapman, "Electron mobility in semiconducting strontium titanate," *Phys. Rev.*, vol. 155, pp. 796–802, Mar 1967.

[36] G. Herranz, M. Basletić, M. Bibes, C. Carrétéro, E. Tafra, E. Jacquet, K. Bouzehouane, C. Deranlot, A. Hamzić, J.-M. Broto, A. Barthélémy, and A. Fert, "High mobility in $LaAlO_3/SrTiO_3$ heterostructures: Origin, dimensionality, and perspectives," *Phys. Rev. Lett.*, vol. 98, p. 216803, May 2007.

[37] A. Kalabukhov, R. Gunnarsson, J. Börjesson, E. Olsson, T. Claeson, and D. Winkler, "Effect of oxygen vacancies in the $SrTiO_3$ substrate on the electrical properties of the $LaAlO_3/SrTiO_3$ interface," *Phys. Rev. B*, vol. 75, p. 121404, Mar 2007.

[38] W. Siemons, G. Koster, H. Yamamoto, W. A. Harrison, G. Lucovsky, T. H. Geballe, D. H. A. Blank, and M. R. Beasley, "Origin of charge density at $LaAlO_3$ on $SrTiO_3$ heterointerfaces: Possibility of intrinsic doping," *Phys. Rev. Lett.*, vol. 98, p. 196802, May 2007.

[39] M. Sing, G. Berner, K. Goß, A. Müller, A. Ruff, A. Wetscherek, S. Thiel, J. Mannhart, S. A. Pauli, C. W. Schneider, P. R. Willmott, M. Gorgoi, F. Schäfers, and R. Claessen, "Profiling the interface electron gas of $LaAlO_3/SrTiO_3$ heterostructures with hard x-ray photoelectron spectroscopy," *Phys. Rev. Lett.*, vol. 102, p. 176805, Apr 2009.

[40] M. Huijben, "Electronically coupled complementary interfaces between perovskite band insulators," *Nature Materials*, vol. 5, no. 7, pp. 556–560, 2006.

[41] R. Pentcheva, M. Huijben, K. Otte, W. E. Pickett, J. E. Kleibeuker, J. Huijben, H. Boschker, D. Kockmann, W. Siemons, G. Koster, H. J. W. Zandvliet, G. Rijnders, D. H. A. Blank, H. Hilgenkamp, and A. Brinkman, "Parallel electron-hole bilayer conductivity from electronic interface reconstruction," *Phys. Rev. Lett.*, vol. 104, p. 166804, Apr 2010.

[42] G. Berner, S. Glawion, J. Walde, F. Pfaff, H. Hollmark, L.-C. Duda, S. Paetel, C. Richter, J. Mannhart, M. Sing, and R. Claessen, "$LaAlO_3/SrTiO_3$ oxide heterostructures studied by resonant inelastic x-ray scattering," *Phys. Rev. B*, vol. 82, p. 241405, Dec 2010.

[43] K. Yoshimatsu, R. Yasuhara, H. Kumigashira, and M. Oshima, "Origin of metallic states at the heterointerface between the band insulators $LaAlO_3$ and $SrTiO_3$," *Phys. Rev. Lett.*, vol. 101, p. 026802, Jul 2008.

[44] O. Copie, V. Garcia, C. Bödefeld, C. Carrétéro, M. Bibes, G. Herranz, E. Jacquet, J.-L. Maurice, B. Vinter, S. Fusil, K. Bouzehouane, H. Jaffrès, and A. Barthélémy, "Towards two-dimensional metallic behavior at $LaAlO_3/SrTiO_3$ interfaces," *Phys. Rev. Lett.*, vol. 102, p. 216804, May 2009.

[45] T. Fix, F. Schoofs, J. L. MacManus-Driscoll, and M. G. Blamire, "Charge confinement and doping at $LaAlO_3/SrTiO_3$ interfaces," *Phys. Rev. Lett.*, vol. 103, p. 166802, Oct 2009.

[46] A. Dubroka, M. Rössle, K. W. Kim, V. K. Malik, L. Schultz, S. Thiel, C. W. Schneider, J. Mannhart, G. Herranz, O. Copie, M. Bibes, A. Barthélémy, and C. Bernhard, "Dynamical response and confinement of the electrons at the $LaAlO_3/SrTiO_3$ interface," *Phys. Rev. Lett.*, vol. 104, p. 156807, Apr 2010.

[47] M. Salluzzo, J. C. Cezar, N. B. Brookes, V. Bisogni, G. M. De Luca, C. Richter, S. Thiel, J. Mannhart, M. Huijben, A. Brinkman, G. Rijnders, and G. Ghiringhelli, "Orbital reconstruction and the two-dimensional electron gas at the $LaAlO_3/SrTiO_3$ interface," *Phys. Rev. Lett.*, vol. 102, p. 166804, Apr 2009.

[48] A. Savoia, D. Paparo, P. Perna, Z. Ristic, M. Salluzzo, F. Miletto Granozio, U. Scotti di Uccio, C. Richter, S. Thiel, J. Mannhart, and L. Marrucci, "Polar

catastrophe and electronic reconstructions at the $LaAlO_3/SrTiO_3$ interface: Evidence from optical second harmonic generation," *Phys. Rev. B*, vol. 80, p. 075110, Aug 2009.

[49] K.-J. Zhou, M. Radovic, J. Schlappa, V. Strocov, R. Frison, J. Mesot, L. Patthey, and T. Schmitt, "Localized and delocalized Ti 3d carriers in $LaAlO_3/SrTiO_3$ superlattices revealed by resonant inelastic x-ray scattering," *Phys. Rev. B*, vol. 83, p. 201402, May 2011.

[50] H. Chen, A. M. Kolpak, and S. Ismail-Beigi, "Fundamental asymmetry in interfacial electronic reconstruction between insulating oxides: An *ab initio* study," *Phys. Rev. B*, vol. 79, p. 161402, Apr 2009.

[51] W.-j. Son, E. Cho, B. Lee, J. Lee, and S. Han, "Density and spatial distribution of charge carriers in the intrinsic n-type $LaAlO_3$-$SrTiO_3$ interface," *Phys. Rev. B*, vol. 79, p. 245411, Jun 2009.

[52] R. Pentcheva and W. E. Pickett, "Charge localization or itineracy at $LaAlO_3/SrTiO_3$ interfaces: Hole polarons, oxygen vacancies, and mobile electrons," *Phys. Rev. B*, vol. 74, p. 035112, Jul 2006.

[53] Z. S. Popović, S. Satpathy, and R. M. Martin, "Origin of the two-dimensional electron gas carrier density at the $LaAlO_3$ on $SrTiO_3$ interface," *Phys. Rev. Lett.*, vol. 101, p. 256801, Dec 2008.

[54] K. Janicka, J. P. Velev, and E. Y. Tsymbal, "Quantum nature of two-dimensional electron gas confinement at $LaAlO_3/SrTiO_3$ interfaces," *Phys. Rev. Lett.*, vol. 102, p. 106803, Mar 2009.

[55] M. Stengel, "First-principles modeling of electrostatically doped perovskite systems," *Phys. Rev. Lett.*, vol. 106, p. 136803, Mar 2011.

[56] Ariando, X. Wang, G. Baskaran, Z. Q. Liu, J. Huijben, J. B. Yi, A. Annadi, A. R. Barman, A. Rusydi, S. Dhar, Y. P. Feng, J. Ding, H. Hilgenkamp, and T. Venkatesan, "Electronic phase separation at the $LaAlO_3/SrTiO_3$ interface," *Nat Commun*, vol. 2, p. 188, 2011.

[57] L. Li, C. Richter, J. Mannhart, and R. C. Ashoori, "Coexistence of magnetic order and two-dimensional superconductivity at $LaAlO_3/SrTiO_3$ interfaces," *Nat. Phys.*, vol. 7, pp. 762–766, 2011.

[58] J. A. Bert, B. Kalisky, C. Bell, M. Kim, Y. Hikita, H. Y. Hwang, and K. A. Moler, "Direct imaging of the coexistence of ferromagnetism and superconductivity at the $LaAlO_3/SrTiO_3$ interface," *Nat. Phys.*, vol. 7, pp. 767–771, 2011.

[59] J.-L. Maurice, C. Carrétéro, M.-J. Casanove, K. Bouzehouane, S. Guyard, Ã. Larquet, and J.-P. Contour, "Electronic conductivity and structural distortion at the interface between insulators $SrTiO_3$ and $LaAlO_3$," *physica status solidi (a)*, vol. 203, no. 9, pp. 2145–2145, 2006.

[60] P. R. Willmott, S. A. Pauli, R. Herger, C. M. Schlepütz, D. Martoccia, B. D. Patterson, B. Delley, R. Clarke, D. Kumah, C. Cionca, and Y. Yacoby, "Structural basis for the conducting interface between $LaAlO_3$ and $SrTiO_3$," *Phys. Rev. Lett.*, vol. 99, p. 155502, Oct 2007.

[61] S. A. Pauli, S. J. Leake, B. Delley, M. Björck, C. W. Schneider, C. M. Schlepütz, D. Martoccia, S. Paetel, J. Mannhart, and P. R. Willmott, "Evolution of the interfacial structure of $LaAlO_3$ on $SrTiO_3$," *Phys. Rev. Lett.*, vol. 106, p. 036101, Jan 2011.

[62] L. Qiao, T. C. Droubay, V. Shutthanandan, Z. Zhu, P. V. Sushko, and S. A. Chambers, "Thermodynamic instability at the stoichiometric $LaAlO_3/SrTiO_3$ (001) interface," *Journal of Physics: Condensed Matter*, vol. 22, no. 31, p. 312201, 2010.

[63] E. Breckenfeld, N. Bronn, J. Karthik, A. R. Damodaran, S. Lee, N. Mason, and L. W. Martin, "Effect of growth induced (non)stoichiometry on interfacial conductance in," *Phys. Rev. Lett.*, vol. 110, p. 196804, May 2013.

[64] C. Cen, S. Thiel, G. Hammerl, C. W. Schneider, K. E. Andersen, C. S. Hellberg, J. Mannhart, and J. Levy, "Nanoscale control of an interfacial metal-insulator transition at room temperature," *Nat Mater*, vol. 7, p. 298, 2008.

[65] F. Bi, D. F. Bogorin, C. Cen, C. W. Bark, J.-W. Park, C.-B. Eom, and J. Levy, "'water-cycle' mechanism for writing and erasing nanostructures at the $LaAlO_3/SrTiO_3$ interface," *Applied Physics Letters*, vol. 97, no. 17, 2010.

[66] B. Förg, C. Richter, and J. Mannhart, "Field-effect devices utilizing $LaAlO_3$-$SrTiO_3$ interfaces," *Applied Physics Letters*, vol. 100, no. 5, pp. –, 2012.

[67] C. Cen, S. Thiel, J. Mannhart, and J. Levy, "Oxide nanoelectronics on demand," *Science*, vol. 323, no. 5917, pp. 1026–1030, 2009.

[68] D. Stornaiuolo, S. Gariglio, N. J. G. Couto, A. Fête, A. D. Caviglia, G. Seyfarth, D. Jaccard, A. F. Morpurgo, and J.-M. Triscone, "In-plane electronic confinement in superconducting $LaAlO_3/SrTiO_3$ nanostructures," *Applied Physics Letters*, vol. 101, no. 22, 2012.

[69] L. Yu and A. Zunger, "A unifying mechanism for conductivity and magnetism at interfaces of insulating nonmagnetic oxides," *ArXiv (cond-mat.mtrl-sci)*, vol. 1402.0895, 2014.

[70] G. Herranz, F. Sánchez, N. Dix, M. Scigaj, and J. Fontcuberta, "High mobility conduction at (110) and (111) $LaAlO_3/SrTiO_3$ interfaces," *Sci. Rep.*, vol. 2, p. 758, 2012.

[71] Y. Chen, N. Pryds, J. E. Kleibeuker, G. Koster, J. Sun, E. Stamate, B. Shen, G. Rijnders, and S. Linderoth, "Metallic and insulating interfaces of amorphous $SrTiO_3$-based oxide heterostructures," *Nano Letters*, vol. 11, no. 9, pp. 3774–3778, 2011.

[72] S. W. Lee, Y. Liu, J. Heo, and R. G. Gordon, "Creation and control of two-dimensional electron gas using Al-based amorphous oxides/$SrTiO_3$ heterostructures grown by atomic layer deposition," *Nano Letters*, vol. 12, no. 9, pp. 4775–4783, 2012.

[73] D. V. Christensen, F. Trier, Y. Z. Chen, A. Smith, J. Nygård, and N. Pryds, "Controlling interfacial states in amorphous/crystalline $LaAlO_3/SrTiO_3$ heterostructures by electric fields," *Applied Physics Letters*, vol. 102, no. 2, 2013.

[74] Z. Q. Liu, C. J. Li, W. M. Lü, X. H. Huang, Z. Huang, S. W. Zeng, X. P. Qiu, L. S. Huang, A. Annadi, J. S. Chen, J. M. D. Coey, T. Venkatesan, and Ariando, "Origin of the two-dimensional electron gas at $LaAlO_3/SrTiO_3$ interfaces: The role of oxygen vacancies and electronic reconstruction," *Phys. Rev. X*, vol. 3, p. 021010, May 2013.

[75] Y. Segal, J. H. Ngai, J. W. Reiner, F. J. Walker, and C. H. Ahn, "X-ray photoemission studies of the metal-insulator transition in $LaAlO_3/SrTiO_3$ structures grown by molecular beam epitaxy," *Phys. Rev. B*, vol. 80, p. 241107, Dec 2009.

[76] G. Berner, A. Müller, F. Pfaff, J. Walde, C. Richter, J. Mannhart, S. Thiess, A. Gloskovskii, W. Drube, M. Sing, and R. Claessen, "Band alignment in

$LaAlO_3/SrTiO_3$ oxide heterostructures inferred from hard x-ray photoelectron spectroscopy," *Phys. Rev. B*, vol. 88, p. 115111, Sep 2013.

[77] G. Singh-Bhalla, C. Bell, J. Ravichandran, W. Siemons, Y. Hikita, S. Salahuddin, A. F. Hebard, H. Y. Hwang, and R. Ramesh, "Built-in and induced polarization across $LaAlO_3/SrTiO_3$ heterojunctions," *Nat Phys*, vol. 7, 2011.

[78] B.-C. Huang, Y.-P. Chiu, P.-C. Huang, W.-C. Wang, V. T. Tra, J.-C. Yang, Q. He, J.-Y. Lin, C.-S. Chang, and Y.-H. Chu, "Mapping band alignment across complex oxide heterointerfaces," *Phys. Rev. Lett.*, vol. 109, p. 246807, Dec 2012.

[79] E. Slooten, Z. Zhong, H. J. A. Molegraaf, P. D. Eerkes, S. de Jong, F. Massee, E. van Heumen, M. K. Kruize, S. Wenderich, J. E. Kleibeuker, M. Gorgoi, H. Hilgenkamp, A. Brinkman, M. Huijben, G. Rijnders, D. H. A. Blank, G. Koster, P. J. Kelly, and M. S. Golden, "Hard x-ray photoemission and density functional theory study of the internal electric field in $SrTiO_3/LaTiO_3$ oxide heterostructures," *Phys. Rev. B*, vol. 87, p. 085128, Feb 2013.

[80] C. Noguera, "Polar oxide surfaces," *Journal of Physics: Condensed Matter*, vol. 12, no. 31, p. R367, 2000.

[81] A. Ohtomo, D. A. Muller, J. L. Grazul, and H. Y. Hwang, "Artificial charge-modulationin atomic-scale perovskite titanate superlattices," *Nature*, vol. 419, pp. 378–380, 2002.

[82] P. Perna, D. Maccariello, M. Radovic, U. Scotti di Uccio, I. Pallecchi, M. Codda, D. Marré, C. Cantoni, J. Gazquez, M. Varela, S. J. Pennycook, and F. M. Granozio, "Conducting interfaces between band insulating oxides: The $LaGaO_3/SrTiO_3$ heterostructure," *Applied Physics Letters*, vol. 97, no. 15, 2010.

[83] Y. Hotta, T. Susaki, and H. Y. Hwang, "Polar discontinuity doping of the $LaVO_3/SrTiO_3$ interface," *Phys. Rev. Lett.*, vol. 99, p. 236805, Dec 2007.

[84] N. C. Bristowe, P. B. Littlewood, and E. Artacho, "Surface defects and conduction in polar oxide heterostructures," *Phys. Rev. B*, vol. 83, p. 205405, May 2011.

[85] Y. Li, S. N. Phattalung, S. Limpijumnong, J. Kim, and J. Yu, "Formation of oxygen vacancies and charge carriers induced in the n-type interface of a $LaAlO_3$ overlayer on $SrTiO_3(001)$," *Phys. Rev. B*, vol. 84, p. 245307, Dec 2011.

[86] G. Rijnders and D. H. A. Blank, "Perovskite oxides: An atomic force pencil and eraser," *Nat Mater*, vol. 7, no. 4, p. 270, 2014.

[87] Z. Zhong, P. X. Xu, and P. J. Kelly, "Polarity-induced oxygen vacancies at $LaAlO_3/SrTiO_3$ interfaces," *Phys. Rev. B*, vol. 82, p. 165127, Oct 2010.

[88] D. W. Reagor and V. Y. Butko, "Highly conductive nanolayers on strontium titanate produced by preferential ion-beam etching," *Nat Mater*, vol. 4, pp. 593–596, 2005.

[89] Z. Q. Liu, Z. Huang, W. M. Lü, K. Gopinadhan, X. Wang, A. Annadi, T. Venkatesan, and Ariando, "Atomically flat interface between a single-terminated $LaAlO_3$ substrate and $SrTiO_3$ thin film is insulating," *AIP Advances*, vol. 2, no. 1, 2012.

[90] C. Cancellieri, D. Fontaine, S. Gariglio, N. Reyren, A. D. Caviglia, A. Fête, S. J. Leake, S. A. Pauli, P. R. Willmott, M. Stengel, P. Ghosez, and J.-M. Triscone, "Electrostriction at the $LaAlO_3/SrTiO_3$ interface," *Phys. Rev. Lett.*, vol. 107, p. 056102, Jul 2011.

[91] M. Huijben, D. Kockmann, J. Huijben, J. E. Kleibeuker, A. van Houselt, G. Koster, D. H. A. Blank, H. Hilgenkamp, G. Rijnders, A. Brinkman, and H. J. W. Zandvliet, "Local probing of coupled interfaces between two-dimensional electron and hole gases in oxide heterostructures by variable-temperature scanning tunneling spectroscopy," *Phys. Rev. B*, vol. 86, p. 035140, Jul 2012.

[92] M. P. Warusawithana, C. Richter, J. A. Mundy, P. Roy, J. Ludwig, S. Paetel, T. Heeg, A. A. Pawlicki, L. F. Kourkoutis, M. Zheng, M. Lee, B. Mulcahy, W. Zander, Y. Zhu, J. Schubert, J. N. Eckstein, D. A. Muller, C. S. Hellberg, J. Mannhart, and D. G. Schlom, "$LaAlO_3$ stoichiometry is key to electron liquid formation at $LaAlO_3/SrTiO_3$ interfaces," *Nat Commun*, vol. 4, p. 2351, 2013.

[93] M. Reinle-Schmitt, C. Cancellieri, D. Li, D. Fontaine, M. Medarde, E. Pomjakushina, C. Schneider, S. Gariglio, P. Ghosez, J.-M. Triscone, and P. Willmott, "Tunable conductivity threshold at polar oxide interfaces," *Nat Commun*, vol. 3, no. 932, 2012.

[94] P. Delugas, A. Filippetti, V. Fiorentini, D. I. Bilc, D. Fontaine, and P. Ghosez, "Spontaneous 2-dimensional carrier confinement at the n-type $SrTiO_3/LaAlO_3$ interface," *Phys. Rev. Lett.*, vol. 106, p. 166807, Apr 2011.

[95] K. Capelle, "A bird's-eye view of density-functional theory," *ArXiv (cond-mat.mtrl-sci)*, vol. 0211443v5, 2006.

[96] R. Martin, "Electronic structure: basic theory and practical methods," *Cambridge Univ Pr*, 2004.

[97] P. Hohenberg and W. Kohn, "Inhomogeneous electron gas," *Phys. Rev.*, vol. 136, pp. B864–B871, Nov 1964.

[98] W. Kohn and L. J. Sham, "Self-consistent equations including exchange and correlation effects," *Phys. Rev.*, vol. 140, pp. A1133–A1138, Nov 1965.

[99] R. Dovesi, R. Orlando, B. Civalleri, C. Roetti, V. R. Saunders, and C. M. Zicovich-Wilson *Z. Kristallogr.*, vol. 220, p. 571, Aug.

[100] X. Gonze, B. Amadon, P.-M. Anglade, J.-M. Beuken, F. Bottin, P. Boulanger, F. Bruneval, D. Caliste, R. Caracas, M. Côté, T. Deutsch, L. Genovese, P. Ghosez, M. Giantomassi, S. Goedecker, D. Hamann, P. Hermet, F. Jollet, G. Jomard, S. Leroux, M. Mancini, S. Mazevet, M. Oliveira, G. Onida, Y. Pouillon, T. Rangel, G.-M. Rignanese, D. Sangalli, R. Shaltaf, M. Torrent, M. Verstraete, G. Zerah, and J. Zwanziger, "Abinit: First-principles approach to material and nanosystem properties," *Computer Physics Communications*, vol. 180, no. 12, pp. 2582 – 2615, 2009.

[101] D. M. Ceperley and B. J. Alder, "Ground state of the electron gas by a stochastic method," *Phys. Rev. Lett.*, vol. 45, pp. 566–569, Aug 1980.

[102] J. P. Perdew, K. Burke, and Y. Wang, "Generalized gradient approximation for the exchange-correlation hole of a many-electron system," *Phys. Rev. B*, vol. 54, pp. 16533–16539, Dec 1996.

[103] J. P. Perdew, K. Burke, and M. Ernzerhof, "Generalized gradient approximation made simple," *Phys. Rev. Lett.*, vol. 77, pp. 3865–3868, Oct 1996.

[104] J. P. Perdew, A. Ruzsinszky, G. I. Csonka, O. A. Vydrov, G. E. Scuseria, L. A. Constantin, X. Zhou, and K. Burke, "Restoring the density-gradient expansion for exchange in solids and surfaces," *Phys. Rev. Lett.*, vol. 100, p. 136406, Apr 2008.

[105] Z. Wu and R. E. Cohen, "More accurate generalized gradient approximation for solids," *Phys. Rev. B*, vol. 73, p. 235116, Jun 2006.

[106] J. Harris, "Adiabatic-connection approach to Kohn-Sham theory," *Phys. Rev. A*, vol. 29, pp. 1648–1659, Apr 1984.

[107] A. D. Becke, "Correlation energy of an inhomogeneous electron gas: A coordinate-space model," *The Journal of Chemical Physics*, vol. 88, no. 2, pp. 1053–1062, 1988.

[108] A. D. Becke, "A new mixing of hartree-fock and local density-functional theories," *The Journal of Chemical Physics*, vol. 98, no. 2, pp. 1372–1377, 1993.

[109] K. Kim and K. D. Jordan, "Comparison of density functional and MP2 calculations on the water monomer and dimer," *The Journal of Physical Chemistry*, vol. 98, no. 40, pp. 10089–10094, 1994.

[110] P. J. Stephens, F. J. Devlin, C. F. Chabalowski, and M. J. Frisch, "Ab initio calculation of vibrational absorption and circular dichroism spectra using density functional force fields," *The Journal of Physical Chemistry*, vol. 98, no. 45, pp. 11623–11627, 1994.

[111] J. Heyd, G. E. Scuseria, and M. Ernzerhof, "Hybrid functionals based on a screened coulomb potential," *The Journal of Chemical Physics*, vol. 118, no. 18, pp. 8207–8215, 2003.

[112] A. D. Becke, "Density-functional exchange-energy approximation with correct asymptotic behavior," *Phys. Rev. A*, vol. 38, pp. 3098–3100, Sep 1988.

[113] C. Lee, W. Yang, and R. G. Parr, "Development of the colle-salvetti correlation-energy formula into a functional of the electron density," *Phys. Rev. B*, vol. 37, pp. 785–789, Jan 1988.

[114] D. I. Bilc, R. Orlando, R. Shaltaf, G.-M. Rignanese, J. Íñiguez, and P. Ghosez, "Hybrid exchange-correlation functional for accurate prediction of the electronic and structural properties of ferroelectric oxides," *Phys. Rev. B*, vol. 77, p. 165107, Apr 2008.

[115] J. Varignon and P. Ghosez, "Improper ferroelectricity and multiferroism in 2H-$BaMnO_3$," *Phys. Rev. B*, vol. 87, p. 140403, Apr 2013.

[116] A. Prikockytė, D. Bilc, P. Hermet, C. Dubourdieu, and P. Ghosez, "First-principles calculations of the structural and dynamical properties of ferroelectric $YMnO_3$," *Phys. Rev. B*, vol. 84, p. 214301, Dec 2011.

[117] Z. Zanolli, J. C. Wojdeł, J. Íñiguez, and P. Ghosez, "Electric control of the magnetization in $BiFeO_3/LaFeO_3$ superlattices," *Phys. Rev. B*, vol. 88, p. 060102, Aug 2013.

[118] C. Franchini, "Hybrid functionals applied to perovskites," *Journal of Physics: Condensed Matter*, vol. 26, no. 25, p. 253202, 2014.

[119] J. M. Soler, E. Artacho, J. D. Gale, A. García, J. Junquera, P. Ordejón, and D. Sánchez-Portal, "The SIESTA method for *ab initio* order-N materials simulation," *Journal of Physics: Condensed Matter*, vol. 14, no. 11, p. 2745, 2002.

[120] D. R. Hamann, M. Schlüter, and C. Chiang, "Norm-conserving pseudopotentials," *Phys. Rev. Lett.*, vol. 43, pp. 1494–1497, Nov 1979.

[121] N. Troullier and J. L. Martins, "Efficient pseudopotentials for plane-wave calculations," *Phys. Rev. B*, vol. 43, pp. 1993–2006, Jan 1991.

[122] T. Bredow, P. Heitjans, and M. Wilkening, "Electric field gradient calculations for Li_x TiS_2 and comparison with ^{7}Li NMR results," *Phys. Rev. B*, vol. 70, p. 115111, Sep 2004.

[123] S. Piskunov, E. Heifets, R. Eglitis, and G. Borstel, "Bulk properties and electronic structure of $SrTiO_3$, $BaTiO_3$, $PbTiO_3$ perovskites: an *ab initio* HF/DFT study," *Computational Materials Science*, vol. 29, no. 2, pp. 165 – 178, 2004.

[124] "http://www.tcm.phy.cam.ac.uk/ mdt26/crystal.html,"

[125] X. Cao and M. Dolg, "Segmented contraction scheme for small core lanthanide pseudopotential basis sets," *J. Molec. Struct. (THEOCHEM)*, vol. 581, pp. 139 – 147, 2002.

[126] K. Nassau and A. Miller, "Strontium titanate: An index to the literature on properties and the growth of single crystals," *Journal of Crystal Growth*, vol. 91, no. 3, pp. 373 – 381, 1988.

[127] S. Geller and V. B. Bala, "Crystallographic studies of perovskite-like compounds. ii. rare earth alluminates," *Acta Crystallographica*, vol. 9, no. 12, pp. 1019–1025, 1956.

[128] P. Bouvier and J. Kreisel, "Pressure-induced phase transition in $LaAlO_3$," *Journal of Physics: Condensed Matter*, vol. 14, no. 15, p. 3981, 2002.

[129] Y. A. Abramov, V. G. Tsirelson, V. E. Zavodnik, S. A. Ivanov, and B. I. D., "The chemical bond and atomic displacements in $SrTiO_3$ from X-ray diffraction analysis," *Acta Crystallographica Section B*, vol. 51, pp. 942–951, Dec 1995.

[130] C. J. Howard, B. J. Kennedy, and B. C. Chakoumakos, "Neutron powder diffraction study of rhombohedral rare-earth aluminates and the rhombohedral to cubic phase transition," *Journal of Physics: Condensed Matter*, vol. 12, no. 4, p. 349, 2000.

[131] C. L. Jia, S. B. Mi, M. Faley, U. Poppe, J. Schubert, and K. Urban, "Oxygen octahedron reconstruction in the $SrTiO_3/LaAlO_3$ heterointerfaces investigated using aberration-corrected ultrahigh-resolution transmission electron microscopy," *Phys. Rev. B*, vol. 79, p. 081405, Feb 2009.

[132] A. J. Hatt and N. A. Spaldin, "Structural phases of strained $LaAlO_3$ driven by octahedral tilt instabilities," *Phys. Rev. B*, vol. 82, p. 195402, Nov 2010.

[133] T. T. Fister, H. Zhou, Z. Luo, S. S. A. Seo, S. O. Hruszkewycz, D. L. Proffit, J. A. Eastman, P. H. Fuoss, P. M. Baldo, H. N. Lee, and D. D. Fong, "Octahedral rotations in strained $LaAlO_3/SrTiO_3$ (001) heterostructures," *APL Materials*, vol. 2, no. 2, 2014.

[134] K. van Benthem, C. Elsässer, and R. H. French, "Bulk electronic structure of $SrTiO_3$: Experiment and theory," *Journal of Applied Physics*, vol. 90, no. 12, pp. 6156–6164, 2001.

[135] S.-G. Lim, S. Kriventsov, T. N. Jackson, J. H. Haeni, D. G. Schlom, A. M. Balbashov, R. Uecker, P. Reiche, J. L. Freeouf, and G. Lucovsky, "Dielectric functions and optical bandgaps of high-k dielectrics for metal-oxide-semiconductor field-effect transistors by far ultraviolet spectroscopic ellipsometry," *Journal of Applied Physics*, vol. 91, no. 7, pp. 4500–4505, 2002.

[136] B.-E. Park and H. Ishiwara, "Electrical properties of $LaAlO_3$/Si and $Sr_{0.8}Bi_{2.2}Ta_2O_9$/$LaAlO_3$/Si structures," *Applied Physics Letters*, vol. 79, no. 6, pp. 806–808, 2001.

[137] B. Choudhury, K. Rao, and R. Choudhury, "Dielectric properties of $SrTiO_3$ single crystals subjected to high electric fields and later irradiated with X-rays or γ-rays," *Journal of Materials Science*, vol. 24, no. 10, pp. 3469–3474, 1989.

[138] T. Konaka, M. Sato, H. Asano, and S. Kubo, "Relative permittivity and dielectric loss tangent of substrate materials for high-T_c superconducting film," *Journal of Superconductivity*, vol. 4, no. 4, pp. 283–288, 1991.

[139] M. Stengel, P. Aguado-Puente, N. A. Spaldin, and J. Junquera, "Band alignment at metal/ferroelectric interfaces: Insights and artifacts from first principles," *Phys. Rev. B*, vol. 83, p. 235112, Jun 2011.

[140] V. Heine, "Theory of surface states," *Phys. Rev.*, vol. 138, pp. A1689–A1696, Jun 1965.

[141] N. C. Bristowe, E. Artacho, and P. B. Littlewood, "Oxide superlattices with alternating p and n interfaces," *Phys. Rev. B*, vol. 80, p. 045425, Jul 2009.

[142] H. Chen, A. Kolpak, and S. Ismail-Beigi, "First-principles study of electronic reconstructions of $LaAlO_3$/$SrTiO_3$ heterointerfaces and their variants," *Phys. Rev. B*, vol. 82, p. 085430, Aug 2010.

[143] R. Pentcheva and W. E. Pickett, "Ionic relaxation contribution to the electronic reconstruction at the n-type $LaAlO_3$/$SrTiO_3$ interface," *Phys. Rev. B*, vol. 78, p. 205106, Nov 2008.

[144] J.-M. Albina, M. Mrovec, B. Meyer, and C. Elsässer, "Structure, stability, and electronic properties of $SrTiO_3$/$LaAlO_3$ and $SrTiO_3$/$SrRuO_3$ interfaces," *Phys. Rev. B*, vol. 76, p. 165103, Oct 2007.

[145] J. P. Perdew and M. Levy, "Physical content of the exact kohn-sham orbital energies: Band gaps and derivative discontinuities," *Phys. Rev. Lett.*, vol. 51, pp. 1884–1887, Nov 1983.

[146] L. J. Sham and M. Schlüter, "Density-functional theory of the energy gap," *Phys. Rev. Lett.*, vol. 51, pp. 1888–1891, Nov 1983.

[147] R. Arras, V. G. Ruiz, W. E. Pickett, and R. Pentcheva, "Tuning the two-dimensional electron gas at the $LaAlO_3/SrTiO_3(001)$ interface by metallic contacts," *Phys. Rev. B*, vol. 85, p. 125404, Mar 2012.

[148] C. Cancellieri, N. Reyren, S. Gariglio, A. D. Caviglia, A. Fête, and J.-M. Triscone, "Influence of the growth conditions on the $LaAlO_3/SrTiO_3$ interface electronic properties," *EPL (Europhysics Letters)*, vol. 91, no. 1, p. 17004, 2010.

[149] S. Gariglio, N. Reyren, A. D. Caviglia, and J.-M. Triscone, "Superconductivity at the $LaAlO_3/SrTiO_3$ interface," *Journal of Physics: Condensed Matter*, vol. 21, no. 16, p. 164213, 2009.

[150] S. Gariglio, N. Stucki, J.-M. Triscone, and G. Triscone, "Strain relaxation and critical temperature in epitaxial ferroelectric $Pb(Zr_{0.20}Ti_{0.80})O_3$ thin films," *Applied Physics Letters*, vol. 90, no. 20, pp. –, 2007.

[151] V. M. Kaganer, R. Köhler, M. Schmidbauer, R. Opitz, and B. Jenichen, "X-ray diffraction peaks due to misfit dislocations in heteroepitaxial structures," *Phys. Rev. B*, vol. 55, pp. 1793–1810, Jan 1997.

[152] M. Stengel and N. A. Spaldin, "*Ab initio* theory of metal-insulator interfaces in a finite electric field," *Phys. Rev. B*, vol. 75, p. 205121, May 2007.

[153] M. Stengel, N. A. Spaldin, and D. Vanderbilt, "Electric displacement as the fundamental variable in electronic-structure calculations," *Nat Phys*, vol. 5, p. 304, 2009.

[154] A. D. Caviglia, S. Gariglio, C. Cancellieri, B. Sacépé, A. Fête, N. Reyren, M. Gabay, A. F. Morpurgo, and J.-M. Triscone, "Two-dimensional quantum oscillations of the conductance at $LaAlO_3/SrTiO_3$ interfaces," *Phys. Rev. Lett.*, vol. 105, p. 236802, Dec 2010.

[155] M. Stengel and N. A. Spaldin, "Origin of the dielectric dead layer in nanoscale capacitors," *Nature*, vol. 443, pp. 679–682, 2006.

[156] P. hsuan Sun, T. Nakamura, Y. J. Shan, Y. Inaguma, M. Itoh, and T. Kitamura, "Dielectric behavior of (1-x)$LaAlO_3$-x$SrTiO_3$ solid solution system at microwave frequencies," *Japanese Journal of Applied Physics*, vol. 37, no. 10R, p. 5625, 1998.

[157] M. Breitschaft, V. Tinkl, N. Pavlenko, S. Paetel, C. Richter, J. R. Kirtley, Y. C. Liao, G. Hammerl, V. Eyert, T. Kopp, and J. Mannhart, "Two-dimensional electron liquid state at $LaAlO_3$-$SrTiO_3$ interfaces," *Phys. Rev. B*, vol. 81, p. 153414, Apr 2010.

[158] M. S. Park, S. H. Rhim, and A. J. Freeman, "Charge compensation and mixed valency in $LaAlO_3/SrTiO_3$ heterointerfaces studied by the FLAPW method," *Phys. Rev. B*, vol. 74, p. 205416, Nov 2006.

[159] J. Lee and A. A. Demkov, "Charge origin and localization at the n-type $SrTiO_3/LaAlO_3$ interface," *Phys. Rev. B*, vol. 78, p. 193104, Nov 2008.

[160] U. Schwingenschlögl and C. Schuster, "Surface effects on oxide heterostructures," *EPL (Europhysics Letters)*, vol. 81, no. 1, p. 17007, 2008.

[161] R. Pentcheva and W. E. Pickett, "Avoiding the polarization catastrophe in $LaAlO_3$ overlayers on $SrTiO_3$(001) through polar distortion," *Phys. Rev. Lett.*, vol. 102, p. 107602, Mar 2009.

[162] Z. Zhong and P. J. Kelly, "Electronic-structure-induced reconstruction and magnetic ordering at the $LaAlO_3/SrTiO_3$ interface," *EPL (Europhysics Letters)*, vol. 84, no. 2, p. 27001, 2008.

[163] S. S. A. Seo, M. J. Han, G. W. J. Hassink, W. S. Choi, S. J. Moon, J. S. Kim, T. Susaki, Y. S. Lee, J. Yu, C. Bernhard, H. Y. Hwang, G. Rijnders, D. H. A. Blank, B. Keimer, and T. W. Noh, "Two-dimensional confinement of $3d^1$ electrons in $LaTiO_3/LaAlO_3$ multilayers," *Phys. Rev. Lett.*, vol. 104, p. 036401, Jan 2010.

[164] A. Filippetti and N. A. Spaldin, "Self-interaction-corrected pseudopotential scheme for magnetic and strongly-correlated systems," *Phys. Rev. B*, vol. 67, p. 125109, Mar 2003.

[165] F. Alessio and V. Fiorentini, "A practical first-principles band-theory approach to the study of correlated materials," *Eur. Phys. J. B*, vol. 71, p. 139, 2009.

[166] C. Cancellieri, M. L. Reinle-Schmitt, M. Kobayashi, V. N. Strocov, P. R. Willmott, D. Fontaine, P. Ghosez, A. Filippetti, P. Delugas, and V. Fiorentini, "Doping-dependent band structure of $LaAlO_3/SrTiO_3$ interfaces by soft x-ray polarization-controlled resonant angle-resolved photoemission," *Phys. Rev. B*, vol. 89, p. 121412, Mar 2014.

[167] J. L. M. van Mechelen, D. van der Marel, C. Grimaldi, A. B. Kuzmenko, N. P. Armitage, N. Reyren, H. Hagemann, and I. I. Mazin, "Electron-phonon interaction and charge carrier mass enhancement in $SrTiO_3$," *Phys. Rev. Lett.*, vol. 100, p. 226403, Jun 2008.

[168] I. Pallecchi, M. Codda, E. Galleani d'Agliano, D. Marré, A. D. Caviglia, N. Reyren, S. Gariglio, and J.-M. Triscone, "Seebeck effect in the conducting $LaAlO_3/SrTiO_3$ interface," *Phys. Rev. B*, vol. 81, p. 085414, Feb 2010.